DISSERTATION

Femtosecond Coherent Vibrational Dynamics of Anabaena Sensory Rhodopsin

Partha Pratim Roy

Dissertation

Submitted to the
Combined Faculty for the Natural Sciences and for Mathematics
Heidelberg University, Germany
for the degree of
Doctor of Natural Sciences (Dr. rer. nat.)

Presented by
M.Sc. Partha Pratim Roy
Born in Kolkata (India)
Oral examination: 18th December, 2018

Femtosecond Coherent Vibrational Dynamics of Anabaena Sensory Rhodopsin

Referees: Prof. Dr. Hans-Robert Volpp

Prof. Dr. Andreas Dreuw

Abstract

The photo-induced isomerization of retinal protonated Schiff base (RPSB) inside the protein pocket is one of the fastest (<ps) and most stereo-selective photochemical reactions in nature. The ground state structure of the RPSB and its surrounding protein constructions are thought to be the two most crucial factors to drive this reaction. The investigation of each factor individually was the main goal of this thesis. Anabaena Sensory Rhodopsin (ASR), a recently discovered microbial retinal protein, serves as an ideal system for this study as it binds two structural isomers (all-*trans*: AT and 13-*cis*: 13C) of the RPSB within the same protein constructions in its photocycle. In the present work, the photo-induced dynamics of the RPSB in ASR has been explored with the help of time resolved coherent vibrational spectroscopic methods, which monitor the photo-induced sub-ps structural changes of the RPSB. These studies have helped to shed light on the intricate relationship between electronic and vibrational dynamics of the RPSB.

In the first half of this thesis, a comparative study showed both electronic and vibrational dynamics are widely distinct for the AT and 13C isomers of the RPSB in ASR. In particular, the 13C isomer exhibited more than five folds faster dynamics than the AT isomer. One possible molecular origin behind this dynamical difference was found by comparing the ground state Raman spectra of the two isomers. It depicted an increase in the amplitude of hydrogen-out-of-plane (HOOP) modes for the 13C isomer, which is usually considered to be an evidence of distortion in the ground state structure for the retinal system. The ground state pre-distortion has been reported as a potential element for the acceleration of the isomerization reaction for the 13C isomer, in analogy with the *cis* isomers of visual rhodopsin and bacteriorhodopsin.

The second half of this work explored the role of the part of protein helix inside the retinal pocket as well as that far away from the pocket. In particular, the replacement of the amino acid residues in vicinity of the RPSB by point mutation caused an acceleration of the reaction rate for the AT isomer, but it had only a minor effect for the 13C isomer of the RPSB. Furthermore, the truncation of the part of the protein, embedded into the cytoplasmic region, affected the formation of the primary photoproduct. All these experimental results lead to two major conclusions of this thesis: (i) the protein constructions govern the retinal isomerization dynamics and (ii) the same protein cage exerts differential interactions on two structural isomers of the RPSB.

Kurzzusammenfassung

Die photoinduzierte Isomerisierung von retinaler protonierter Schiff-Base (RPSB) in der Proteintasche ist eine der schnellsten (<ps) und stereoselektivsten photochemischen Reaktionen in der Natur. Die Grundzustandstruktur des RPSB und die umgebenden Proteinkonstruktionen gelten als die beiden wichtigsten Faktoren, die diese Reaktion antreiben. Die Untersuchung jedes einzelnen Faktors war das Hauptziel dieser Arbeit. Anabaena Sensory Rhodopsin (ASR), ein kürzlich entdecktes mikrobielles Retinalprotein, dient als ideales System für diese Studie, da es zwei Strukturisomere (all-trans: AT und 13-cis: 13C) des RPSB innerhalb derselben Proteinkonstruktionen in seinem Photozyklus bindet . In der vorliegenden Arbeit wurde die photoinduzierte Dynamik des RPSB in ASR mit Hilfe zeitaufgelöster kohärenter schwingungsspektroskopischer Methoden untersucht, die die photoinduzierten sub ps-Strukturänderungen des RPSB nachverfolgen. Diese Studien halfen, die komplizierte Beziehung zwischen elektronischer und Schwingungsdynamik des RPSB aufzuklären.

In der ersten Hälfte dieser Arbeit zeigte eine vergleichende Studie, dass sowohl die elektronische als auch die Schwingungsdynamik für die AT- und 13C-Isomere des RPSB in ASR sehr verschieden sind. Insbesondere das 13C-Isomer zeigte eine mehr als fünffach schnellere Dynamik als das AT-Isomer. Ein möglicher molekularer Ursprung dieses dynamischen Unterschieds wurde durch Vergleich der Ramanspektren beider Isomere im Grundzustand gefunden. Für das 13C-Isomer stellte dies eine Zunahme der Schwingungsamplitude von Wasserstoffatomen aus der Molekülebene heraus dar, was normalerweise als Hinweis auf eine Verdrillung der Grundzustandsstruktur des Retinalsystems gesehen wird. Die Vorverzerrung im Grundzustand wurde als potentielles Element für die Beschleunigung der Isomerisierungsreaktion für das 13C-Isomer beschrieben, analog zu den cis-Isomeren von Sehpigment Rhodopsin und Bakteriorhodopsin.

Die zweite Hälfte dieser Arbeit untersuchte die Rolle des Teils der Proteinhelix in der Retinaltasche sowie des weit vom RPSB entfernten Teils. Insbesondere der Austausch der Aminosäurereste nahe des RPSB durch Punktmutation führte zu einer Beschleunigung der Reaktionsgeschwindigkeit beim AT-Isomer, hatte jedoch nur einen geringen Einfluss auf das 13C-Isomer des RPSB. Darüber hinaus beeinflusst die Verkürzung des in die cytoplasmatische Region eingebetteten Teils des Proteins die Bildung des primären Photoprodukts. All diese experimentellen Befunde führen zu zwei wichtigen Schlussfolgerungen dieser Arbeit: (i) die

Proteinkonstruktionen bestimmen die Dynamik der retinalen Isomerisierung und (ii) derselbe Proteinkäfig übt auf zwei Strukturisomere des RPSB unterschiedliche Wechselwirkungen aus.

List of scientific contributions

Articles

"*Effect of point mutations on the ultrafast photo-isomerization of Anabaena Sensory Rhodopsin*", D. Agathangelou, Y. Orozco-Gonzalvez, M. C. Marín, **P. P. Roy**, J. Brazard, H. Kandori, K.-H. Jung, J. Léonard, T. Buckup, N. Ferré, M. Olivucci and S. Haacke, *Faraday Discuss.* **2018**, *207*, 55-75

"*Mapping the ultrafast vibrational dynamics of all-trans and 13-cis retinal isomerization in Anabaena Sensory Rhodopsin*", **P. P. Roy**, Y. Kato, R. Abe-Yoshizumi, E. Pieri, N. Ferré, H. Kandori and T. Buckup, submitted to *Phys. Chem. Chem. Phys.*, August 29, **2018**.

"*Pre-distortion of retinal chromophore due to point mutation of Anabaena Sensory Rhodopsin leads to shorter excited state lifetime*", **P. P. Roy**, R. Abe-Yoshizumi, H. Kandori and T. Buckup, *in preparation.*

"*Influence of cytoplasmic domain on the ultrafast photocycle of Anabaena Sensory Rhodopsin.*" **P. P. Roy**, Y. Kato, D. Agathangelou, H. Kandori, J. Léonard, S. Haacke and T. Buckup, *in preparation*.

"*Effect of mutation on the vibrational dynamics of Anabaena Sensory Rhodopsin.*", **P. P. Roy**, R. Abe-Yoshizumi, H. Kandori and T. Buckup, *in preparation*.

Conference proceedings

"*Mapping the ultrafast vibrational dynamics of all-trans and 13-cis retinal isomerization in Anabaena Sensory Rhodopsin*", **P. P. Roy**, Y. Kato, R. Abe-Yoshizumi, H. Kandori and T. Buckup, Ultrafast Phenomena XXI 2018, *in press*.

Contributions in Conference talks

"*Exploring vibrational dynamics of Anabaena Sensory Rhodopsin by pump impulsive vibrational spectroscopy.*", **P. P. Roy**, Y. Kato, H. Kandori and T. Buckup, *Frühjahrstagung der Deutschen*

Physikalischen Gesellschaft (Spring Meeting of the German Physical Society), Mainz, Germany, March **2017**.

"*Exploring excited state vibrational dynamics of Anabaena Sensory Rhodopsin.*", **P. P. Roy**, Y. Kato, H. Kandori and T. Buckup, *International Conference of Photochemistry*, Strasbourg, France, July **2017**.

"*Mapping the ultrafast vibrational dynamics of all-trans and 13-cis retinal isomerization in Anabaena Sensory Rhodopsin*", **P. P. Roy**, Y. Kato, R. Abe-Yoshizumi, H. Kandori and T. Buckup, *International Conference on Ultrafast Phenomenon XXI*, Hamburg, Germany, **2018**

Contributions in Poster presentation

"*Exploring population and vibrational dynamics of Anabaena Sensory Rhodopsin.*" **P. P. Roy**, Y. Kato, H. Kandori and T. Buckup, *Centre for Quantum Dynamics*, Heidelberg, Germany, **2016**

"*Effect of truncation of cytoplasmic domain on ultrafast dynamics of Anabaena Sensory Rhodopsin.*" **P. P. Roy**, Y. Kato, H. Kandori and T. Buckup, *International Conference of Photochemistry*, Strasbourg, France, July **2017**.

List of Abbreviation

AT	all-*trans*
AP	actinic pulse
BBO	beta-barium borate
BR	bacteriorhodopsin
CARS	coherent anti-Stokes Raman (scattering)
CCD	charged coupled device
CI	conical intersection
CPA	chirped pulse amplifier
CPM	cross phase modulation
DA	dark adapted
DFWM	degenerate four-wave-mixing
ES	excited state
ESA	excited state absorption
FC	Franck-Condon
FFT	fast Fourier transformation
fs	femtosecond
FSRS	Femtosecond Stimulated Raman Spectroscopy
FWM	four wave mixing
FWHM	full width at half maximum
GVD	group velocity dispersion
GS	ground state
GSB	ground state bleach
HOOP	hydrogen-out-of-plane
HPLC	high performance liquid chromatography
IC	internal conversion
IR	infrared

IVR	internal vibrational energy redistribution
IVS	impulsive vibrational spectroscopy
ISRS	impulsive stimulated Raman scattering
kHz	kilo Hertz
LA	light adapted
MRP	microbial retinal protein
nc-OPA	non-collinear optical parametric amplifier
OD	optical density
PA	photoproduct absorption
PDA	photodiode array
PIA	photo-induced absorption
ps	picosecond
PMT	photo multiplier tube
RPSB	retinal protonated Schiff base
SE	stimulated emission
SEP	stimulated emission pumping
TA	transient absorption
UV	ultraviolet
WT	wild type
13C	13-*cis*

Table of contents

Chapter 1

Introduction

Since the advent of femtosecond laser pulses, one of the main objectives of ultrafast spectroscopy has been the recording of atomic motion during a chemical reaction.[1-5] For that purpose, many spectroscopic techniques[6-21] have been developed to follow such changes in polyatomic molecules in gas phase,[22-24] solutions[8, 25-27] or proteins.[28-31] One possible way to explore the molecular dynamics is to map the transient spectral changes during a chemical reaction by time resolved techniques. In this regard, advancement of ultrafast optics in the last decades has played a central role and, nowadays, pulses as short as 10 fs can be routinely generated in labs around the world.[32-37] This has allowed tracking several kinds of photo-induced molecular dynamics in singlet fission,[38-39] molecular photo-switching,[40-43] retinal isomerization[29-30, 44-46] etc. Interest about these ultra-fast photo-induced chemical reactions has been expanding because of their great potential to serve as optoelectronic materials.[47] Natural photo switches like retinal has been intensively researched because of their prospective applications in biogenetic engineering as well as for inspiring technological advances of bio mimetic photo switches for harnessing solar energy.[42-43, 48] In this thesis, full focus has been devoted to study the light induced isomerization reaction of retinal protonated schiff base (RPSB) inside a protein membrane (Figure 1.1). The photo-induced isomerization of retinal is one of the fastest (<ps) photo-chemical reactions in nature, and is based on the interconversion between two structurally distinct isomeric configurations of the RPSB (Figure 1.1(a)). The RPSB is found to be covalently bound to a Lysine residue of the seventh helix of the protein membrane in all retinal pigments of organisms ranging from micro-bacteria to

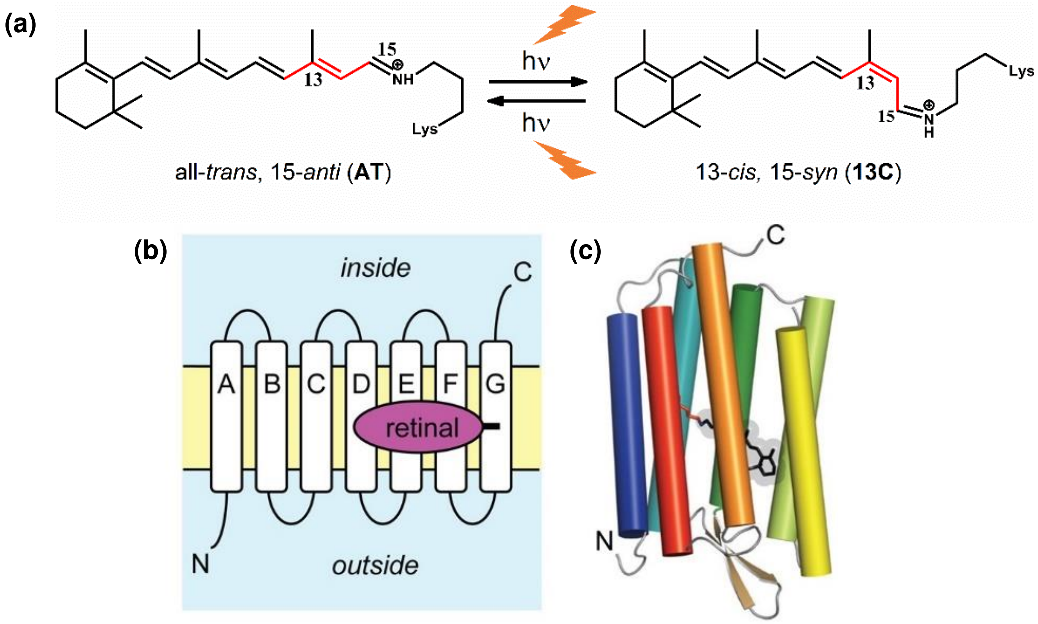

Figure 1.1: (a) Photo-induced reversible interconversion between two isomeric forms of retinal protonated schiff base (RPSB): all-*trans*, 15-*anti* (AT) and 13-*cis*, 15-*syn* (13C) configurations. The bonds in red show the position of isomerization. (b) Topology of the retinal protein membrane containing seven α-helices (A to G) spanning the lipid bilayer. The N-terminus faces the outside of the cell and the C-terminus the inside. (c) Retinal is covalently attached to a lysine side chain on helix G. Cartoon representation of the helical arrangement of a microbial rhodopsin with attached retinal chromophore. Figure (b) and (c) are adapted with the permission from reference 54 (Copyright 2014 American Chemical Society).

mammals (Figure 1.1(b, c)).[49-51] This particular reaction is found to be the central element behind many fundamental biological activities like photosynthesis, vertebrate vision, bacterial gene expressions, ion-pumping etc.[52-54] These are accomplished by initiating a photo-cycle, which converts the solar energy into chemical potential. Because of these profound chemical and biological significance, retinal photochemistry has drawn the attention of experimentalists and theoreticians alike. In the last thirty years, intensive investigations has been performed to inspect the photo-induced molecular dynamics of RPSB in different retinal proteins.[55-60] Results of these studies have successfully identified the key components that tune this ultrafast reaction, but failed to provide a detail mechanism of this process. Following sections present a general description of the retinal photochemistry according to present understanding and, subsequently, points out the strategies that have been taken in this thesis to draw a picture of retinal isomerization with mechanistic details.

1.1 Retinal photochemistry

Retinal proteins are well known to incorporate different structural isomeric forms of RPSB in the ground state for different organisms e.g. 11-*cis* in visual rhodopsin, 9-*cis* in *iso*-rhodopsin, all-*trans* in micro-bacterial retinal proteins (MRP's) like bacteriorhodopsin, halo-rhodopsin etc. Comparative time resolved studies have shown a wide diversity in reaction rates and efficiencies (Table 1.1) among these retinal pigments in spite of having their very similar architectures inside the protein pocket.[29-31, 44, 60-67] For instance, the retinal isomerization in visual pigments takes place within 100 fs[29-30, 68-70] with a quantum yield about 67%,[71] whereas it takes more than 0.5 ps to complete the isomerization with much lower yield for the MRP´s.[72-74] On the other hand, the photo-isomerization of RPSB (all-*trans*) in solution takes place with a much slower rate (>1 ps)[26, 75-76] and leads to the formation of a mixture of different stereo-isomers with a quantum yield of a few percent for each sub-product (16% 11-*cis*, 5% 9-*cis*).[25] All these observations have been interpreted as the electrostatic interaction between the bound RPSB and the amino acid residues of the protein surrounding steers the isomerization reaction.

Bovine (RH) and bacteriorhodopsin (BR), which belong to two different classes (visual pigments vs MRPs), have been most frequently compared in this context. Generally, the retinal isomerization is believed to be initiated by a rapid reorganization of C-C bond lengths within a

Table 1.1: Isomerization reaction rates and quantum yields of RPSB in different retinal proteins and solutions.

Retinal	Configuration of ground state RPSB	Isomerization rate	Quantum yield
Bovine rhodopsin (RH)	11-*cis*	<0.1 ps	~67%
Bacterio-rhodopsin (BR)	all-*trans*	~0.6 ps	~64%
Iso-rhodopsin	9-*cis*	~1 ps	~22%
Halo-rhodopsin (HR)	all-*trans*	~1 ps	~30%
Channello-rhodopsin1	13-*cis*	~0.11 ps	~60%
RPSB in solution	all-*trans*	>1 ps	<20%

few tens of femtosecond after the excitation,[77] to form the sub-picosecond reactive excited state coined as I intermediate.[78] For BR, this state decays non-exponentially to form the 'J' intermediate[28, 78] during the course of internal conversion, which is associated with a weak spectral evolution.[44, 79] Moreover, the cross section of the emission state has been found to be constant throughout the fluorescence lifetime.[79] Therefore, both observations have been taken as a non-ballistic internal conversion in BR. The retinal isomerization in RH, however, differs from that: The dramatic spectral evolution during the internal conversion has been interpreted as a coherent isomerization reaction, where a nuclear wave packet generated by impulsive stimulated Raman scattering (ISRS) evolves in a ballistic fashion towards the ground state potential surface.[29-30, 46, 66]

This contrast between the nature and speed of the isomerization reactions for two different classes of retinal proteins has been often rationalized by the difference in planarity of the ground state structures of RPSB bound inside the cavity of retinal pocket.[80] Structural strains on RPSB inside different protein pockets can originate either due to distinct structural conformations of each isomer or due to changes in the electrostatic interaction between RPSB and the opsin moiety. Structural investigations[49, 80-81] have shown that the 11-*cis* ground state isomer in visual rhodopsin is present as a non-planar, pre-twisted structure, which facilitates the reaction to proceed rapidly.[82] However, for BR, neither NMR studies[80, 83] nor resonance Raman spectra[84] has shown any evidence of such a pre-twisting for the ground state all-*trans* isomer. Furthermore, a quantum chemical computational study[82] of twisted retinal in gas phase showed sub-100 fs dynamics, which further indicates the pre-straining alone can lead to a rapid isomerization process even in absence of any specific electrostatic interaction of RPSB with the surrounding.

Although the geometric orientation of RPSB inside the protein pocket has been proven to be a crucial element, a few comparative time-resolved studies of mutated proteins with wild-type analogs have shown the role of the surrounding protein in catalyzing the isomerization dynamics. For example, the replacement of a charged amino acid residue with a neutral one in bacteriorhodopsin results in a significant deceleration of the reaction rate.[85-86] A similar comparative study by replacing one non-polar residue with a polar one showed an acceleration of the rate.[87] On the other hand, the molecular dynamics of RPSB in solution was found to be almost independent of the dielectric constants and viscosity of the solvent, which suggests that the bond selective isomerization inside the protein pocket is mainly governed by steric effects.[64] All these observations together motivate the investigation of the individual role of the ground state conformation and the opsin moiety on the retinal isomerization mechanism.

1.2 Anabaena Sensory Rhodopsin

One systematic way to address these open questions is to investigate RPSB of two different conformations under the same protein environment. The recently discovered[88] Anabaena Sensory Rhodopsin (ASR) has been assisting to shed new light on this issue.[45, 49, 53, 89-90] Like other MRP's, it comprises of 13-*cis*, 15-*syn* (13C) and all-*trans*, 15-*anti* (AT) in ground state (Figure 1.1). Being a photochromic sensor, the isomeric ratio depends on the wavelength of external illumination light.[89] When it is illuminated with an orange light (~590 nm) it forms a mixture (~40:60) of AT and 13C isomers in a light adapted photo-stationary equilibrium.[90] On the other hand, it adopts a thermally relaxed AT form under a dark adapted condition. Within the photocycle (Figure 1.2), each isomer undergoes isomerization around C13=C14 in a sub-ps time scale that results in a hot photo-intermediate J (13-*cis*, 15-*anti* and all-*trans*, 15-*syn*, respectively). Later, it forms the K-photo product (K_{AT} and K_{13C}) within 100 ps via vibrational relaxation, which undergo further isomerization around C15=N on a longer time scale (<ns) to generate 13C and AT GS, respectively (Figure 1.2). Therefore, ASR is a distinct member among the rhodopsin family, which provides a unique opportunity to track and compare the isomerization reaction in both directions (AT to 13C

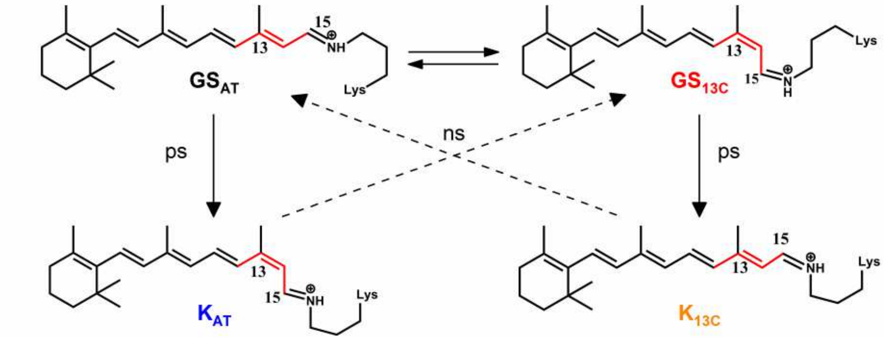

Figure 1.2: Schematic representation of the photocycle of AT and 13C isomer of ASR. After excitation, each isomer undergoes isomerization around C13=C14 bond in sub-ps timescale to form the corresponding hot photo-product, J_{AT} and J_{13C}, which generate K_{AT} and K_{13C} by further isomerization around C15=N on sub-ns time scale to complete the photo-cycle.

and 13C to AT) of the photo-cycle within the same protein environment. This is extremely advantageous in order to disentangle the effect of the ground state conformation of RPSB on its isomerization dynamics.

Recently, a couple of comparative pump-probe studies of AT and 13C isomers of ASR showed a stark contrast in the reaction kinetics.[45, 90] It has been observed that the 13C isomer shows a ballistic kinetics and the isomerization completes within 100 fs, which is very similar to RH.[45, 90] The AT isomer shows, however, about seven fold (~770 fs)[45, 90] slower kinetics, which is reminiscent to BR. This large disparity in the reaction dynamics has been qualitatively explained by the quantum chemical excited trajectory calculations, which suggest the existence of a small barrier or plateau in the excited potential energy surface of AT-isomer but not for the 13C isomer.[91] The quantum yield of the isomerization for each direction is also very different: it is about 2.7 times higher for AT than for the 13C isomer.[92] Lower quantum yield with shorter lifetimes has also been observed in other MRP's. It goes against the Landau-Zener rule of tunneling probability.[93]

1.3 Model of the retinal isomerization reaction

In order to explain the variation of the reaction rates and efficiencies, one needs to have a precise knowledge about the molecular potential energy surfaces. In this regard, a few combined experimental and theoretical research efforts have unleashed a fundamental understanding of molecular energy levels of the retinal. In earlier reports, a two-state barrierless model was proposed for the visual rhodopsin.[29, 68, 72, 94] Later, it was found to be inadequate to explain a number of experimental observations for MRP's, such as temperature dependence of florescence,[95] excitation wavelength dependence of the reaction quantum yield,[71] spectral stagnation of the excited state during internal conversion[79, 96] or multi-exponential excited state dynamics.[44, 97-98] In order to explain these discrepancies, an alternative model (three-state model) was proposed, where an additional electronic state was invoked (Figure 1.3 (a)).[44, 99-102] This model allows for the buildup of a small potential energy barrier due to the avoided curve crossing between closely spaced excited states, $1B_u$ and $2A_g$ (Figure 1.3 (a)). Appearance of this small energy barrier in the first excited electronic state can explain the abovementioned experimental observations.

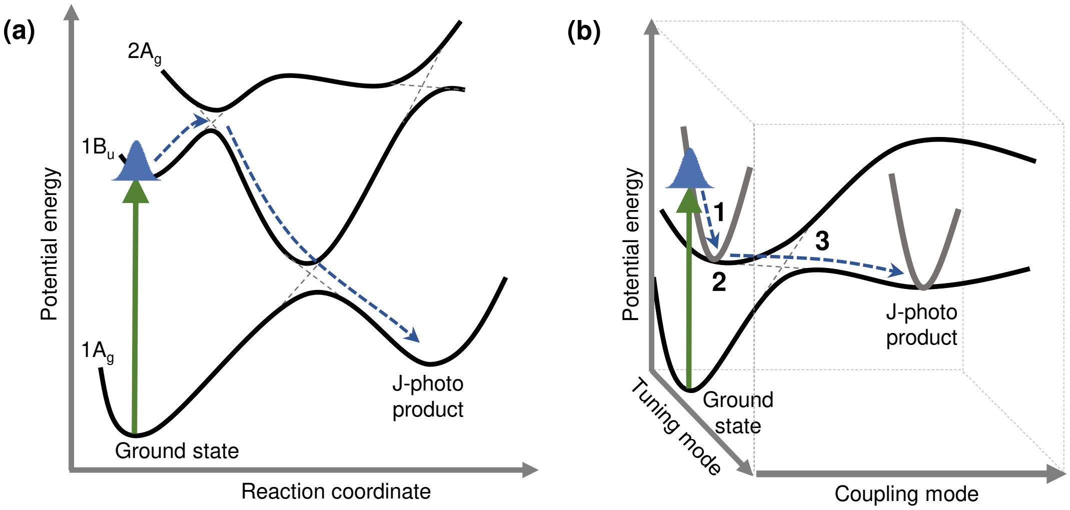

Figure 1.3: (a) Three state model: a non-adiabatic coupling between the closely spaced $1B_u$ and $2A_g$ states generates a barrier. (b) Two-state-two-mode model: a multi-mode view of retinal isomerization reaction. It gives an atomistic insight about the retinal isomerization reaction which is accomplished by three sequential events: (1) bond length alternation (BLA), (2) inter-molecular vibrational energy re-distribution (IVR) and (3) crossing the conical intersection between the ground and excited states to accomplish the isomerization reaction. In each graph, the conical intersections are shown by thin grey dotted lines. The green arrows denote the excitation of the ground state population and the blue Gaussian envelope represents the wave packet, formed by coherent excitation. The blue dotted arrow shows the reactive trajectory.

In both two-state and three-state models, the reaction was described only along a single reaction coordinate that is usually the dihedral angle along the isomerizing double bond of RPSB. However, poly-atomic molecules like RPSB have a number the vibrational modes (C-C, C=C, C=N stretches, CH_3 rocking, skeletal torsions) other than the torsion around C=C and C-C bonds, which participate in the reaction. Thus, a multi-mode view of the potential energy surface is necessary to get the complete picture of the retinal isomerization reaction. This has been accounted recently by several theoretical simulations, which have proposed a two-state-two-mode model.[103-104] Herein, the vibrational modes of RPSB are classified into two groups: One is named ‘tuning modes’, which are required to reach the conical intersection by reducing the energy gap between the ground and excited electronic states; the other is named ‘coupling modes’, which are active in the formation of the conical intersection.[93] This model, which has been supported by a number of experimental evidences,[27, 105-106] provides generalized atomistic insights of the sequential events happening after the photoexcitation of RPSB. Immediately after excitation, a rapid reorganization of bond lengths, which is called bond length alternation (BLA), takes place along the coordinates of the tuning modes within 20-30 fs. This is often defined as ‘initial excited state relaxation’. It causes the system to reach a stationary point in the potential energy surface and at this point, the energy, initially deposited on reactive chemical bonds of retinal like C=C or C-C stretches, is transferred to torsional modes. This process is known as intermolecular vibrational energy redistribution (IVR), which is followed by a space saving isomerization, popularly known as ‘bicycle pedal motion’ of RPSB,[107-108] via a major torsion around a specific C=C bond.

1.4 Coherent vibrational spectroscopy

Despite the general knowledge about the decay time constants associated with inter-electronic state population decays, only little is known about the real time structural changes of RPSB during the isomerization process and more specifically, the roles of each individual vibrational mode to channelize the reaction into the reactive pathway. Time resolved coherent vibrational spectroscopy comes to aid here. In the case of Raman based time-resolved spectroscopy techniques, “vibrational wave packets” are impulsively generated by excitation laser pulses shorter than the vibrational period of the correspond modes. These “vibrational wave packets” evolve along a defined trajectory, determined by the topology of the potential energy surface. The oscillation of the vibrational wave packet leaves its signature as a periodic modulation on top of the exponential electronic population kinetics. Hence, knowledge about the coherently excited wave packet motion along with the population kinetics promises to provide a clearer insight into the excited state trajectory.

Time resolved coherent vibrational spectroscopy can be experimentally implemented in several ways. In two-pulse pump-probe spectroscopy, a spectrally broad ultrashort pump pulse induces such vibrational wave packets (Figure 1.4), which are probed by a delayed probe pulse. In spite of the successfully application of this pump-probe spectroscopy to different systems ranging from low (samples in gas phase or in solution[8, 109]) to very high (light harvesting complexes,[110] carotenoids,[111-112] semiconductors[113]) complexity, extraction of the pure excited state signal is not always straightforward. Vibrational wave packets generated in the excited state potential show usually a much faster dephasing times than in the ground state manifold, leaving a very small

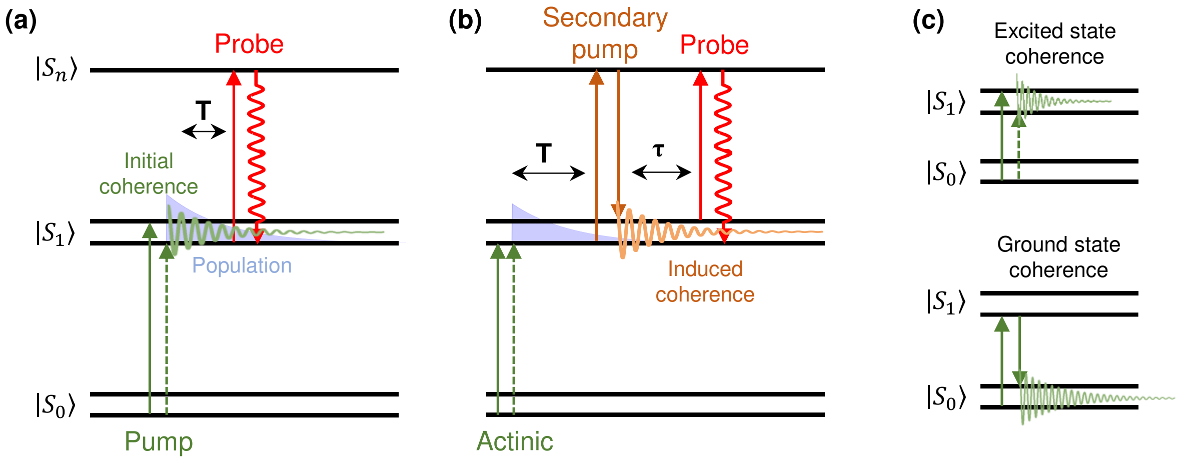

Figure 1.4: (a) Traditional dual pulse pump probe spectroscopy: An ultrashort pump pulse excites a part of the ground state (S0) population and induces coherences, which are tracked by probe pulse at a certain delay (T). (b) Three pulse pump probe spectroscopy: An actinic pulse initiates reaction by exciting a part of ground state (S0) population. Subsequently, an ultrashort second pump pulse (re)induces vibrational coherence at a certain delay (T), which is tracked by the probe pulse (τ). (c) Ground vs excited coherence: An ultrashort actinic pump pulse, resonant to S0→S1 transition, can induce coherence in the ground as well as in the excited state. However, the excited state coherences undergo much faster dephasing than ground state coherences.

contribution in the optical signal. Moreover, the pump spectrum being resonant to S_0 to S_1 transition (Figure 1.4 (c)), can also induce vibrational coherence in the ground-state, which may overlap with the signal of excited state, and make the separation of both contributions very challenging.

A convenient approach to overcome these limitations is to extent the dimensionality of the technique by introducing a second pump interaction (Figure 1.4 (b)). Here, an actinic pulse, which is analogous to the pump pulse in two-pulse pump-probe spectroscopy, initiates the reaction by exciting a part of the ground state population in the excited state. Later, a second pump pulse (re)induces a vibrational coherence at a certain delay (T) after the reaction starts. This solves the abovementioned issues of traditional two-pulse pump-probe techniques as follows: (i) The second excitation can (re)induce the vibrational coherence at any time during the chemical reaction depending on the time delay between actinic and secondary pump pulse (T) and hence, is not anymore limited by the dephasing time of the initial coherence. Thus, the transient structural change can be followed from the beginning until the completion of the reaction. (ii) By tuning the actinic spectrum to the $S_0 \rightarrow S_1$ transition and the second pump spectrum to the $S_1 \rightarrow S_n$ transition, a selective induction of the excited wave packet is possible (Figure 1.4 (b)). This provides a huge advantage to characterize and follow the vibrational modes associated to specific electronic states.

Thus, the time resolved coherent vibrational spectroscopy, having this immense potential to capture the structural dynamics during ultrafast reaction, promises to address the following long-standing questions in the context of retinal photo-chemistry: (i) the importance of ground state retinal conformation in tuning the reaction dynamics; (ii) the characterization and activation mechanisms of each individual vibrational mode; (iii) the key modes driving the reaction along the reactive trajectories; (iv) the influence of the surrounding retinal protein in catalyzing the isomerization process; (v) the discrepancy in the relation between reaction rates and efficiencies. All these together help to shed more light on the topology of the molecular potential energy surfaces with finer mechanistic details and provide a deeper insight into the molecular origin of such diverse isomerization reaction dynamics of the retinal proteins.

1.5 Outline of thesis

Following these points of motivation, chapter 2 of this thesis introduces a theoretical basis for the time-resolved non-linear spectroscopic techniques. A brief description of third- and fifth-order nonlinear techniques has been presented within the framework of a response function formalism. This theoretical basis has been used to interpret the experimental data presented later.

The first half of chapter 3 describes the implementation of different time resolved spectroscopic techniques, discussed in chapter 2. In the second half, the analysis algorithms, which have been used for the data processing to retrieve the molecular information, are presented.

Chapters 4 to 7 cover the experimental results, analysis and their interpretations to explore the impact of ground state retinal structure (Chapter 4-5) and the role of opsin moiety (Chapter 6-7) on the retinal isomerization reaction.

Chapter 4 introduces a comparison of the population dynamics between the AT and 13C isomers of RPSB in ASR. In order to evaluate the population dynamics, the time resolved electronic spectra of the RPSB has been evaluated by measuring the transient absorption signals under the dark and light adapted conditions. This highlights the importance of the ground state configuration of RPSB on its isomerization dynamics.

Chapter 5 is dedicated for a comparative study of the vibrational coherence dynamics between the AT and 13C isomers of the RPSB in ASR. The evolution of transient Raman spectra of the RPSB has been mapped by exploiting impulsive vibrational spectroscopic techniques. This depicts a common picture of the sequential events happening during the isomerization reaction of both isomers. However, the ground state vibrational spectra as well as the time scale of the vibrational spectral evolution after the photoexcitation exhibits a stark difference between the AT and 13C isomers. Based on these observations, the molecular origin behind the large disparity in the reaction kinetics of the AT and 13C isomers was rationalized.

Chapter 6 illustrates the role of the protein constructions surrounding the RPSB in its photo-isomerization dynamics. For that purpose, two different point mutations were carried out in ASR. A set of comparative transient absorption and (pump-) DFWM studies between the wild type and its mutants has showed a large impact of mutation on the electronic as well as vibrational dynamics of the RPSB. Moreover, the mutation has been found to show an asymmetric effect on the photo-induced dynamics of the AT and 13C isomers of the RPSB.

Chapter 7 presents the role of cytoplasmic domain of the opsin moiety on the ultrafast photocycle of the ASR. For that goal, a comparative study of the photo-induced molecular dynamics between wild type and C-domain truncated ASR has been done by transient absorption spectroscopy.

Chapter 8 summarizes the major findings and conclusions derived from the presented investigations. In addition, a few possible outlooks have been presented, which can address the questions remained unanswered in this work

Chapter 2

Introduction to Time Resolved Nonlinear Spectroscopy

2.1 Nonlinear polarization

When an oscillating external electric field interacts with a medium, it creates a macroscopic oscillating polarization. The fundamental concept of coherent nonlinear spectroscopy lies behind the description of this macroscopic polarization. In general, the induced polarization is directly proportional to the incident electric field strengths. Depending on the strengths of the incident electric fields different terms can contribute to the polarization, each of which is generated by a specific number (n) of light-matter interactions:

$$P(\omega_s) = \sum_{n=1}^{\infty} P^{(n)}(\omega_s) = \sum_{n=1}^{\infty} \varepsilon_0\, \chi^{(n)}(\omega_s; \omega_1, \omega_2, \dots, \omega_n) E_1(\omega_1) E_2(\omega_2) \dots E_n(\omega_n) \tag{2.1}$$

Here, ε_0 is the electric permittivity in vacuum and χ is the susceptibility, which is dependent on the refractive index of the medium. $\omega_1, \omega_2, \dots, \omega_n$ are the frequencies of the interacting electric fields and ω_s is frequency of the emitted electric field. In equation (2.1), P and E are vector quantities, whereas χ and ω are tensor and scalar variables, respectively. For the sake of simplicity, all the variables in the equations used in this chapter, are written without any distinct representation for scalar, tensor or vector variables.

For an isotropic medium, the even order macroscopic polarization terms in equation (2.1) are cancelled out due to the symmetry and only the odd terms remain[114-115]:

$$P(\omega_s) = \varepsilon_0 \begin{pmatrix} \chi^1(\omega_s;\omega_1)E_1(\omega_1) + \chi^3(\omega_s;\omega_1,\omega_2,\omega_3)E_1(\omega_1)E_2(\omega_2)E_3(\omega_3) \\ \ldots + \chi^{2N-1}(\omega_s;\omega_1,\omega_2,\ldots,\omega_{2N-1})E_1(\omega_1)E_2(\omega_2)\ldots E_n(\omega_{2N-1}) \end{pmatrix} \tag{2.2}$$

Equation (2.2) describes the light induced macroscopic polarization in frequency domain. To describe evolution of the system during and after each light-matter interaction, it is more convenient to express the polarization as a function of time. It can be done by using the time dependent Schrödinger equation and treating the light-matter interaction in a semi-classical perturbative approach assuming all the interactions happening in a weak field regime ($<10^{15}$ W/cm^2).[116] The full derivation of the time dependent light induced macroscopic polarization by a semi classical treatment has been introduced in the references[114, 116-117]. Only a brief description will be presented here.

The Hamiltonian of the system (equation (2.3)) can be expressed as sum of a time independent term, H_0 and a time dependent term, $V(t)$, where the latter one represents a perturbative potential, generated due to the light-matter interactions:

$$H = H_0 + V(t) \tag{2.3}$$

$$V(r,t) = -\int dr\, E(r,t)\, P(r,t) \tag{2.4}$$

In quantum mechanics, the system is usually described in terms of wave function, ($|\psi\rangle$). However, an alternative approach is the density matrix formulation ($\rho = |\psi\rangle\langle\psi|$). This is suitable to deal with systems in condensed phase, which represent mixed states consisting of a statistical ensemble of several quantum states ($|\psi_i\rangle$). Thus, substitution of the wave function ($|\psi\rangle$) by the density matrix (ρ) in the Schrödinger equation leads to equation (2.5) (see reference[114, 117] for the detail derivation), which is often named as Liouville-Von Neumann equation:

$$\frac{\delta\rho}{\delta t} = -\frac{i}{\hbar}[H,\rho] \tag{2.5}$$

It describes the time evolution of the density matrix. By solving[114] the equation (2.5), an expression for the density matrix can be obtained using perturbation theory as,

$$\rho = \rho_{eq} + \sum_{n=1}^{\infty} \rho^{(n)} \tag{2.6}$$

where,

$$\rho^{(n)} = \left(-\frac{i}{h}\right)^{n} \int_{-\infty}^{t} d\tau_n \int_{-\infty}^{\tau_n} d\tau_{n-1} \dots \int_{-\infty}^{\tau_2} d\tau_1 \left[V_n(\tau_n), \left[V_{n-1}(\tau_{n-1}) \dots, \left[V_1(\tau_1), \rho_{eq}\right]\right]\right] \tag{2.7}$$

Here, ρ_{eq} represents the density matrix of the system in equilibrium i.e. the system prior to any light-matter interactions. V_n represents the perturbative potential, generated after nth light-matter interaction at time τ_n (Figure 2.1(a)) and $\rho^{(n)}$ is nth order density matrix, describing the state of the system after n number of interactions. Knowing $\rho^{(n)}$, the induced macroscopic polarization can be expressed as the expectation value of $\mu\rho^{(n)}$, where μ denotes the dipole operator (see references[114, 117]):

$$P^{(n)}(t) = Tr\left[\mu(t)\rho^{(n)}(E,t)\right] \tag{2.8}$$

'Tr' represents the trace. Substituting $\rho^{(n)}$ in the equation (2.7) into (2.8) yields equation (2.9), which describes nth order polarization in time domain.

$$P^{(n)}(t) = \int_{0}^{\infty} dt_n \dots \int_{0}^{\infty} dt_1\, R^{(n)}(t)\, E(t - t_n)\, E(t - t_n - t_{n-1}) \dots E(t - t_n \dots - t_1) \tag{2.9}$$

where,

$$R^{(n)}(t) = \left(\frac{i}{\hbar}\right)^{n} \theta(t_1)\, \theta(t_2) \dots\, \theta(t_n) Tr\left[\left[[\mu(t_n + t_{n-1} + .. + t_1), \hat{\mu}(t_{n-1} + .. + t_1)], \dots \mu(0)\right] \rho_{eq}\right] \tag{2.10}$$

Here, t_1, t_2,…, t_n represent the time intervals between two successive interactions (see Figure 2.1). $\theta(t_n)$ is a heavy-side step function. $R^{(n)}(t)$ is known as the total response function, which describes the evolution of the system during and after each light-matter interaction. Moreover, a comparison between the equation (2.1) and (2.9) shows that the total response function is basically the time

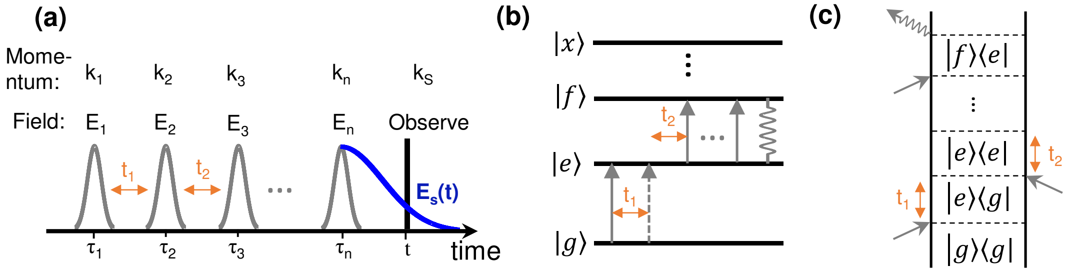

Figure 2.1: (a) General scheme of the pulse sequence for $\boldsymbol{n}^{\text{th}}$ order nonlinear interaction. Here, E_1, E_2,.., E_n represent the envelopes of electric fields of the interacting pulses and corresponding momentums are denoted by k_1, k_2,…, k_n, respectively. E_s and k_s represent the electric fields and momentum of the emitted electromagnetic signal. Energy ladder and double-sided Feynman diagram representations of this $\boldsymbol{n}^{\text{th}}$ order nonlinear interaction are shown in (b) and (c).

domain counter part of the susceptibility ($\chi^{(n)}$) in frequency domain. Hence, like $\chi^{(n)}$, the total response function, $R^{(n)}(t)$ contains all the information about the molecular properties like energy gaps between the states (electronic, rotational or vibrational transition frequency), interaction with the bath (dephasing) etc. Thus, it is the key term to describe n^{th} order nonlinear interactions.

Since the total response function represents a physical quantity, the commutator in equation (2.10) can be expressed as the sum of two complex conjugate pairs, R_i and $R_i{}^*$. Each R_i term is called a response function, sum of which constitutes the total response function, $R^{(n)}$:

$$R^{(n)}(t) = \left(\frac{i}{\hbar}\right)^n \theta(t_1)\,\theta(t_2)\,...\,\theta(t_n)\sum_i R_i{}^{(n)}\,(t_1, t_2, ..., t_n) - R_i{}^{(n)^*}\,(t_1, t_2, ..., t_n) \tag{2.11}$$

For n number of light matter interactions in a system consisting of given number of energy levels, the expansion of the commutator in $R^{(n)}(t)$ (equation (2.10)) results in a certain number of response functions, $R_i{}^{(n)}$. Each of the terms can be interpreted diagrammatically in two possible ways: the energy ladder representation or the double-sided Feynman diagram (Figure 2.1). According to the general convention, ket and bra side interaction of the incident field with the density matrix ($\rho = |\psi\rangle\langle\psi|$), shown in the double-sided Feynman diagrams, are represented by solid and dashed arrows, respectively in the ladder diagram. The wavy arrow at the end of n^{th} interaction represents the emitted signal.

Knowing the form of light induced macroscopic polarization, $P^{(n)}(t)$ (equation (2.10)), the electric field of the emitted signals, E^{emit} can be derived by solving the wave equation[114] that results in:

$$E^{emit}(t_1, t_2, \dots, t_n, t) \propto \frac{i\omega_s l}{\eta(\omega_s)c} P^{(n)}(t_1, t_2, \dots, t_n, t) \tag{2.12}$$

where, c is the velocity of light, l is the sample path length and $\eta(\omega_s)$ is the refractive index of the sample at ω_s, frequency of the emitted signal. Due to the energy and momentum conservation, the frequency (ω_s) and direction (that defines the momentum: $\overrightarrow{k_s}$) of the emitted electromagnetic signal are determined by that of the interacting fields ($\omega_n, \overrightarrow{k_n}$), which is named as the phase matching condition:

$$\omega_s = \sum_{n=1}^{\infty} \pm\omega_n \,, \qquad \overrightarrow{k_s} = \sum_{n=1}^{\infty} \pm\overrightarrow{k_n} \tag{2.13}$$

2.2 First-order response function

For a single light-matter interaction, the total response function (see equation (2.10)) can be expressed as follows:

$$R^{(1)}(t) = \left(\frac{i}{\hbar}\right) \theta(t)\, Tr\left[[\mu(t), \mu(0)]\, \rho_{eq}\right] \tag{2.14}$$

In analogy of equation (2.11), it can be written as:

$$R^{(1)}(t) = \left(\frac{i}{\hbar}\right) \theta(t) \left[{R_1}^{(1)}(t) - {R_1}^{(1)^*}(t)\right] \tag{2.15}$$

where,

$${R_1}^{(1)}(t) = \left(\frac{i}{\hbar}\right)^n \theta(t)\, Tr\left[\mu(t)\, \mu(0)\, \rho_{eq}\right] \tag{2.16}$$

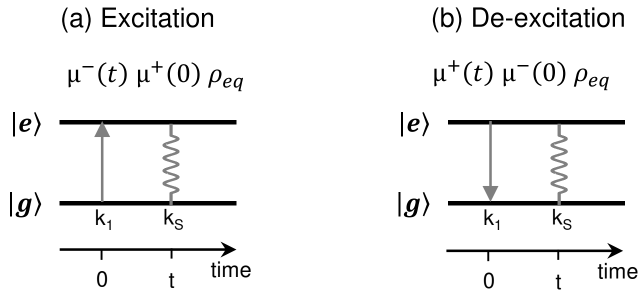

Figure 2.2: Representation of first order response function where, the excitation and de-excitation are represented as $\boldsymbol{\mu}^+$and $\boldsymbol{\mu}^-$, respectively.

Equation (2.16) is interpreted as a single light-matter interaction at time zero and subsequently, emission of the signal, which is recorded at time, t ((Figure 2.2)). Now, this single interaction can cause either excitation or de-excitation to climb up or down the energy ladder (Figure 2.2). Hence, the dipole operator, μ in the response function, ${R_1}^{(1)}(t)$ is presented as $\mu^+$and μ^- for the interaction causing the excitation and de-excitation, respectively.

2.3 Third-order nonlinear spectroscopy

Third-order spectroscopy is the lowest order nonlinear spectroscopy (see equation (2.2)) for any isotropic medium and the most commonly used spectroscopic technique. Third-order response function for a three level system yields a number response functions within the rotating wave approximation,[114] where rapidly oscillating terms are neglected (only valid if the incident electric field is near resonance with the atomic transition and intensity is low). Three of the response function terms are shown in equation (2.17) to (2.19):

$$ {R_1}^{(3)}(t) = Tr\left[\mu^-(t_4)\mu^+(t_3)\mu^-(t_2)\mu^+(t_1)\rho_{eq}\right] \tag{2.17} $$

$$ {R_2}^{(3)}(t) = Tr\left[\mu^-(t_4)\mu^+(t_1)\rho_{eq}\mu^-(t_2)\mu^+(t_3)\right] \tag{2.18} $$

$$ {R_3}^{(3)}(t) = Tr\left[\mu^-(t_4)\mu^+(t_3)\mu^+(t_1)\rho_{eq}\mu^-(t_2)\right] \tag{2.19} $$

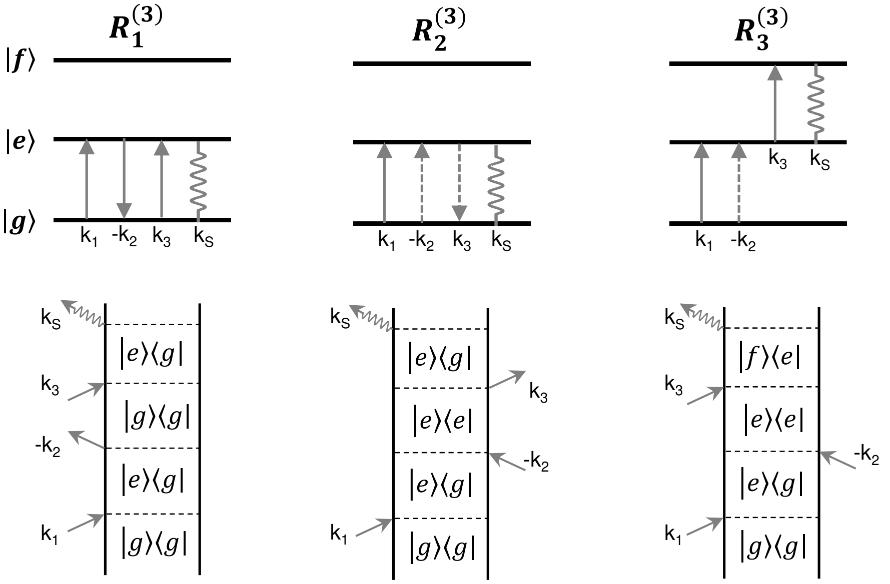

Figure 2.3: Representation of third order response functions for a three level system in the energy ladder (top) and the double sided Feynman diagrams (bottom). Solid and dotted arrows in the energy ladder diagram represents ket and bra interactions, respectively. $\boldsymbol{R_1}$, $\boldsymbol{R_2}$ and $\boldsymbol{R_3}$ represent three different responsive pathways which are named ground state bleach (GSB), excited stimulated emission (ESE) and excited state absorption (ESA), respectively in the context of transient absorption spectroscopy. Here, the diagrams representing the third order interaction under the phase matching condition, $k_s=k_1-k_2+k_3$, are shown.

A diagrammatic representation of each term has been shown in Figure 2.3. In all three cases, the first interaction on the ket side of the density matrix when the system is in equilibrium, ($\rho_{eq} = |0\rangle\langle 0|$) creates an electronic coherence between ground ($|g\rangle$) and excited ($|e\rangle$) electronic states which evolves within time duration, t_1. Then a second interaction takes place, which can cause population either in ground state (${R_1}^{(3)}$) or in excited state (${R_2}^{(3)}$ and ${R_3}^{(3)}$). Third interaction again induces an electronic coherence between $|g\rangle$ and $|e\rangle$ for ${R_1}^{(3)}$and ${R_2}^{(3)}$ by excitation on ket and de-excitation on bra side, respectively. In the terminology of transient absorption spectroscopy, these two non-linear responsive pathways are known as ground state bleach (GSB) and excited stimulated emission (ESE), respectively. On the other hand, third interaction in R_3 causes an excitation on the ket side and an electronic coherence between two excited electronic states $|e\rangle$ and $|f\rangle$. This pathway is named as excited state absorption (ESA) in the context of transient absorption. Three terms (${R_1}^{(3)}, {R_2}^{(3)}, {R_3}^{(3)}$) mentioned here, represent the light-matter interaction under the phase matching condition, $k_S=k_1-k_2+k_3$ (usually called non-rephasing pathway[114, 117]), which has been maintained for all the transient grating measurements, carried out in this thesis. In general, three more terms appear for third-order nonlinear spectroscopic signals under different phase matching conditions: $-k_1+k_2+k_3$ (rephasing pathway) and and $k_1+k_2-k_3$ (quantum coherence pathway) (see references[114, 117] for further details).

In the case of transient absorption spectroscopy, the first two pulses create a hole in the ground state by exciting a part of the ground state population in the excited state. As the system evolves in between the second and the third interactions, this population either returns back to the ground state or it passes to another stationary state (forming new photo-product) causing partial refilling of initially created holes. Usually the population relaxation from one state to another is described by an exponential function (see equation (2.20)). The time constants of these exponential decays can be acquired by varying the time delay between the second and third interactions. This gives the essential information about the molecular dynamics.

Although the system has been described by a simple energy diagram consisting of three electronic levels, for any molecule, each electronic level contains several vibrational levels. Therefore, the first two interactions can lead the system either in an electronic population state (diagonal element

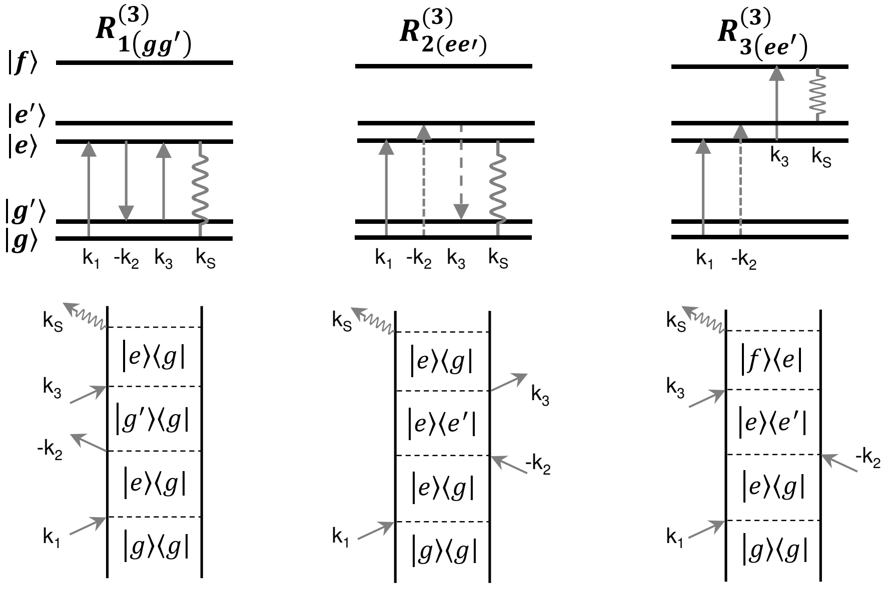

Figure 2.4: Representation of a few possible vibrational coherence pathways for the third order light matter interaction by energy ladder (top) and double sided Feynman diagrams (bottom) under the phase matching condition, $k_s=k_1-k_2+k_3$. Solid and dotted arrows in energy ladder diagram represents ket and bra interactions, respectively. Subscripts gg' and ee' denote the vibrational coherence created in the ground and excited state, respectively after first pair of interactions.

of the density matrix) or in a vibrational coherence state (off-diagonal element of the density matrix). Thus, in addition to the population pathways shown in Figure 2.3, the third order non-linear response function also contains vibrational coherence pathways depicted in Figure 2.4. In order to prepare the vibrational coherence pathways, there is one essential condition for the first pair of pulses to fulfill: The pulse width should be shorter than the period of molecular vibration. Hence, if the excitation pulse is short enough, the third order signal not only contains the information about the population decay but also contains the information about the vibrational coherence, which appears as a damped oscillatory feature on top of the population decay signals. Note in Figure 2.4 that both the ground (gg') and excited state (ee') vibrational coherences contribute to the third order signal when the excitation spectrum is resonant to $|g\rangle \rightarrow |e\rangle$ transition frequency.

Soon after the optical excitation, the excited population (diagonal element of the density matrix) and coherence (off-diagonal elements of the density matrix) decay with time constants, T_1 and T_2, which are known as the population relaxation time and the dephasing rate of coherence, respectively. T_1 denotes the life time of corresponding electronic level, whereas T_2 depends on the interaction of the system with the bath. Hence, the propagation of the elements in time dependent density matrix is usually described by following equations:

$$\text{Diagonal element:} \qquad \rho^{aa}(t) = \exp[-g_{aa}(t,\, T_1)]\rho_{eq}^{aa} \tag{2.20}$$

$$\text{Off diagonal element:} \qquad \rho^{ab}(t) = \exp[-i\omega_{ab}t - g_{ab}(t,\, T_2\,)]\rho_{eq}^{ab} \tag{2.21}$$

Here, ω_{ab} is the transition frequency between the eigenstates, a and b. The functions, g_{aa} and g_{ab} are called the line shape functions, which determine the electronic and vibrational spectral shapes, respectively. Using these equations, each response pathway (equations (2.17) to (2.19)) can be fully expressed (see references[114, 116-117] for more details).

Implementation: Third-order nonlinear spectroscopy has been implemented in this thesis by two different ways: (i) Transient absorption (TA) and (ii) Four wave mixing (FWM) transient grating (Figure 2.5). Although both of these techniques provides the same molecular information they differ in respect to the first pair of light matter interactions, which changes the phase matching condition of the generated signals. In TA, the first pair of interaction comes from the same laser

(a) Transient absorption

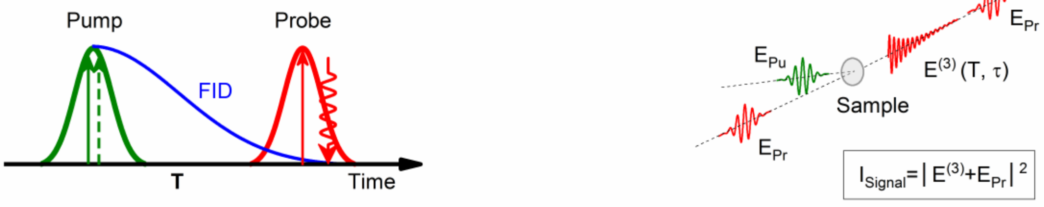

(b) Degenerate four wave mixing

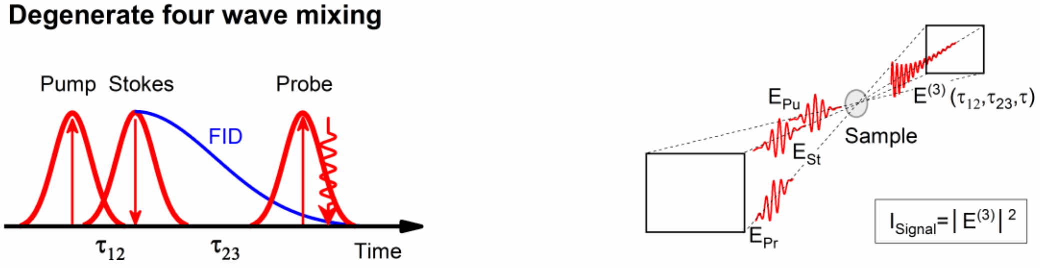

Figure 2.5: Schematic representation of the pulse sequence used in (a) Transient absorption (TA) and (b) Degenerate four wave mixing (DFWM) experiments. The pump and probe pulses are represented by green and red colors as they usually have different spectra. The delay between pump and probe pulse is denoted by T. Generated signal is detected in self-heterodyne fashion, where the probe pulse acts as a local oscillator. In DFWM, all three pulses, pump, stokes and probe, are degenerate and all of them are presented in red colors. In case of DFWM, the three incident beams are arranged in a folded BOXCARS geometry and the non-rephasing homodyne signal is generated at the phase matching direction: $\mathbf{k_s} = \mathbf{k_{Pu}} - \mathbf{k_{St}} + \mathbf{k_{Pr}}$.

pulse known as pump, whereas in FWM, the first two interactions come from two different beams named as pump and Stokes.

In TA, the pump and probe pulses usually have different spectral contents. The changes, induced by the pump pulse, are interrogated by the subsequent probe pulse by varying the time delay (T). Since the same pulse provide the first pair of interactions ($\mathrm{k}_1 = \mathrm{k}_2 = \mathrm{k}_{Pu}$), the signal is radiated in the same direction of the probe ($\mathrm{k}_s = \mathrm{k}_{Pu} - \mathrm{k}_{Pu} + \mathrm{k}_{Pr} = \mathrm{k}_{Pr}$). This way of detection is known as self-heterodyne detection, where the probe pulse acts as a local oscillator. Here, the signal along, which is incorporated in the probe beam after the sample, is spectrally resolved in a spectrometer.

For FWM, same laser output is split into three to provide three degenerate pulses: pump, Stokes and probe. Therefore, this is named as degenerate four wave mixing (DFWM) technique. Similar to TA, the delayed probe interrogates the changes, induced by the pump/Stokes pair, at different delays (τ_{23}). In addition, the delay (τ_{12}) between the pump and Stokes pulses can also be scanned, which is sometime useful to characterize the vibrational mode as quantum coherence or population beating.[118] The pump, Stokes and probe beams are often arranged in a folded BOXCARS geometry. The corresponding non-rephasing signal is generated in the phase matching direction ($\mathrm{k}_{s} = \mathrm{k}_{Pu} - \mathrm{k}_{St} + \mathrm{k}_{Pr}$), which is different from the direction of any of three incident pulses and hence, the signal is background free. This way of detection is known as homodyne detection. On the one hand, the FWM signal, being background free, has higher signal to noise ratio than TA. On the other hand, the vibrational coherence survives shorter in homodyne FWM signal than that obtained by heterodyne technique like TA. This is due to an intrinsic interference between population grating and vibrational coherence.[118] This is disadvantageous especially to probe the excited state coherence, which has extremely short population decay times and results in a broad spectral width in the Fourier transformed spectra.

2.4 Fifth-order nonlinear spectroscopy

Fifth-order nonlinear spectroscopy involves a primary (first pair of pulses: actinic pulses (AP)) and secondary (second pair of pulses: pump/Stokes) interaction. The primary interaction populates the excited electronic states (may induce vibrational coherence also), while the secondary interaction (re)induces the vibrational coherences. These vibrational coherence is followed by a probe pulse. It provides two major advantages over the third-order nonlinear techniques. Firstly, the higher lying electronic states, which are not accessible by primary excitation either because of the large energy gaps or due to the symmetry forbidden transition, can be accessed by the secondary impulsive excitation. Secondly, the excited state coherence dynamics, which is very difficult to investigate by third-order techniques because of extremely short lifetimes of the excited state, can be thoroughly interrogated by (re)inducing the coherence at a different delay after the primary excitation.

Similar to the third-order nonlinear interactions (equation (2.17)-(3.19)), the fifth-order interactions can also be evaluated under the framework of response function formalism. Some examples of fifth-order response functions are shown below:

$$R_1{}^{(5)}(t) = Tr\left[\mu^-(t_6)\mu^+(t_3)\mu^-(t_2)\mu^+(t_1)\rho_{eq}\mu^-(t_4)\mu^+(t_5)\right] \tag{2.22}$$

$$R_2{}^{(5)}(t) = Tr\left[\mu^-(t_6)\mu^+(t_1)\rho_{eq}\mu^-(t_2)\mu^+(t_3)\mu^-(t_4)\mu^+(t_5)\right] \tag{2.23}$$

$$R_3{}^{(5)}(t) = Tr\left[\mu^-(t_6)\mu^+(t_5)\mu^-(t_4)\mu^+(t_3)\mu^+(t_1)\rho_{eq}\mu^-(t_2)\right] \tag{2.24}$$

$$R_4{}^{(5)}(t) = Tr\left[\mu^-(t_6)\mu^+(t_5)\mu^-(t_4)\mu^+(t_3)\mu^-(t_2)\mu^+(t_1)\rho_{eq}\right] \tag{2.25}$$

$$R_5{}^{(5)}(t) = Tr\left[\mu^-(t_6)\mu^+(t_5)\mu^-(t_4)\mu^+(t_1)\rho_{eq}\mu^-(t_2)\mu^+(t_3)\right] \tag{2.26}$$

$$R_5{}^{(5)}(t) = Tr\left[\mu^-(t_6)\mu^+(t_3)\mu^+(t_1)\rho_{eq}\mu^-(t_2)\mu^-(t_4)\mu^+(t_5)\right] \tag{2.27}$$

The corresponding diagrammatic representation for each of these response pathways is shown in Figure 2.6. Since the main goal behind the implementation of the fifth-order technique in this thesis

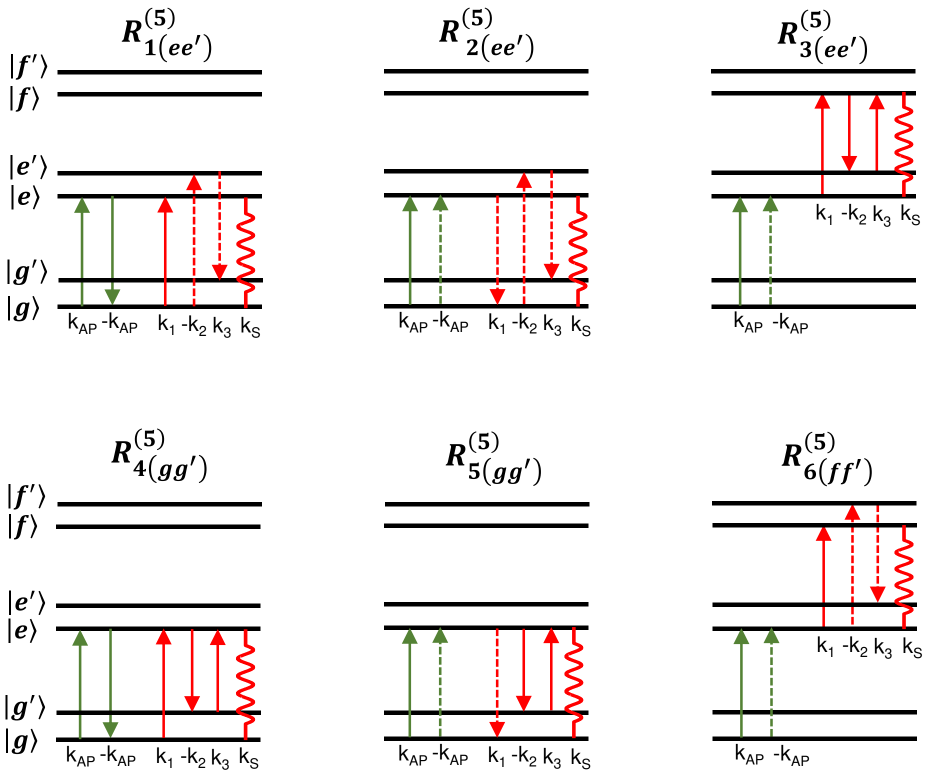

Figure 2.6: Representation of a few possible response pathways for the fifth order light matter interaction by energy ladder diagrams. The solid and dotted arrows in energy ladder diagram represent ket and bra interactions, respectively. Subscripts $\boldsymbol{gg'}$, $\boldsymbol{ee'}$ and $\boldsymbol{ff'}$ denote the vibrational coherence created in the ground ($\boldsymbol{g}$), excited ($\boldsymbol{e}$) and upper excited ($\boldsymbol{f}$), respectively by secondary interactions. Here, the diagrams representing the vibrational coherence pathways for the fifth order light-matter interaction under the phase matching condition, $k_s=k_1-k_2+k_3$, are shown.

is to track the vibrational dynamics, only the diagrams leading to the coherence pathways, are depicted in Figure 2.6. Here, the first pair of interactions i.e. the primary excitation by AP, shown by green arrows in Figure 2.6, creates a population (or coherence) in the ground or excited state, which evolves before the third interaction takes place. Rest of the interactions by the subsequent three pulses (named as FWM pulses) take place in similar manner as presented earlier for the third-order technique (Figure 2.3). However, unlike a third-order technique, a part of the ground population has already been transferred in the excited state before the FWM pulse sequence arrives. Thus, the secondary excitation (second pair of pulses, shown by the red arrows in Figure 2.6) can induce vibrational coherence not only in the excited state (e) and ground (g) states, but also in the higher lying excited (f) state. The relative contribution of the excited and ground state coherences can be controlled by a careful choice of the primary and secondary excitation spectra though. Since the goal of the fifth-order spectroscopy is to track the excited state wave packet (see section 1.4), the spectra resonant to $|g\rangle \rightarrow |e\rangle$ and $|e\rangle \rightarrow |f\rangle$ transition are usually

(a) Pump-impulsive vibrational spectroscopy

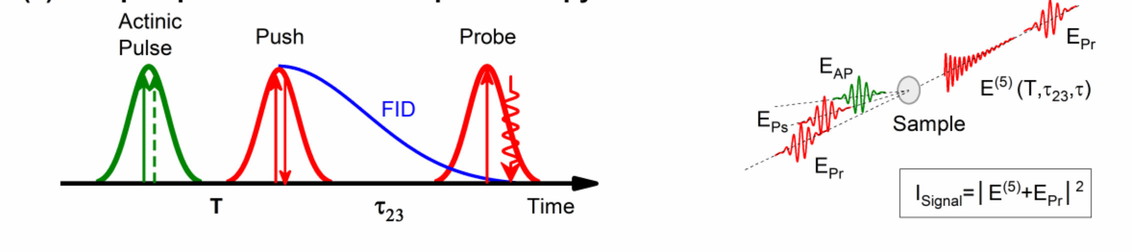

(b) Pump-degenerate four wave mixing

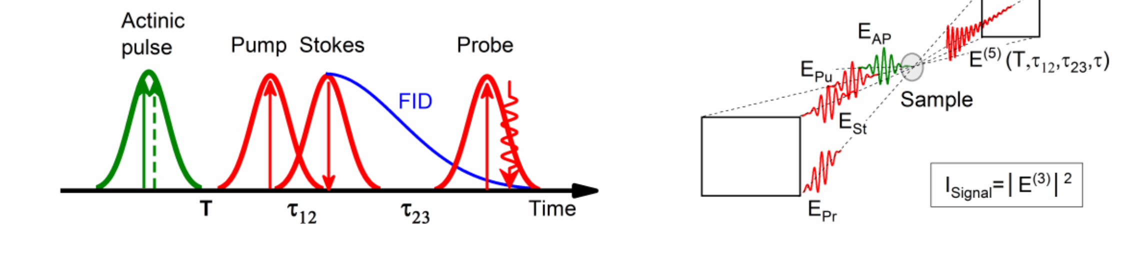

Figure 2.7: Schematic representation of the pulse sequence used in (a) pump impulsive vibrational spectroscopy (pump-IVS) and (b) pump degenerate four wave mixing (pump-DFWM). The actinic and FWM pulses are represented by green and red colors, respectively. The delay between actinic and push (a) or pump/Stokes (b) pulse is denoted by T. The pump-IVS signal is detected in self-hetero-dyne fashion, where the probe acts as local oscillator. In case of pump-DFWM, three incident beams are arranged in an extended folded BOXCARS geometry and homodyne signal is generated at the phase matching direction, $\mathbf{k}_s = \mathbf{k}_{AP} - \mathbf{k}_{AP} + \mathbf{k}_{Pu} - \mathbf{k}_{St} + \mathbf{k}_{Pr}$.

selected for the primary and secondary excitation; thus the contributions of the excited state vibrational dynamics ($R_3{}^{(5)}, R_6{}^{(5)}$) predominates over the ground state vibrational dynamics ($R_1{}^{(5)}, R_4{}^{(5)}$) in the fifth-order signals. However, an overlap of the secondary excitation spectrum with the stimulated emission band can also lead to a substantial contribution of the excited state dynamics due to the stimulated emission pumping (SEP) response pathway ($R_2{}^{(5)}$).

Implementation: Similar to the third-order technique fifth-order technique can also be implemented in two different ways: (i) pump-impulsive vibrational spectroscopy (pump-IVS) and (ii) pump-degenerate four wave mixing (pump-DFWM), which differ in terms of signal detection methods. In both cases, a pulse having a spectrum resonant to the steady state absorption of the sample (i.e. $S_0 \rightarrow S_1$ transition) is used as the AP.

In the case of pump-IVS, the second pair of excitations is provided by the same pulse, named as push ($k_1 = k_2 = k_{Ps}$). Therefore, the signal is generated in the same direction of the probe ($k_s = k_{AP} - k_{AP} + k_{P_s} - k_{Ps} + k_{Pr} = k_{Pr}$) and detected in heterodyne fashion, where the probe acts as a local oscillator.

In the case of pump-DFWM, the secondary interactions are provided by two different pulses (pump/Stokes). Thus, the signal is generated in the corresponding phase matching direction of the extended folded BOXCARS geometry ($k_s = k_{AP} - k_{AP} + k_{P_u} - k_{St} + k_{Pr}$) and detected in a background free homodyne fashion.

2.5 Detection frequency dependence of vibrational coherence

The vibrational coherence in the four wave mixing signals, obtained by using a broad excitation spectrum, show an intrinsic detection wavelength dependence.[118] This is because of the following reason. In order to induce a vibrational coherence of certain frequency, a pair of spectral components in the excitation spectrum is required, which have corresponding frequency difference between them. Hence, for a high frequency vibrational coherence, a large difference in frequency between the selected pair of frequency components is required (Figure 2.8 (a)). A spectral pair selected from two edges of the excitation spectrum have a large difference in frequencies and hence, is most probable to induce high frequency coherence by coherent excitation of the

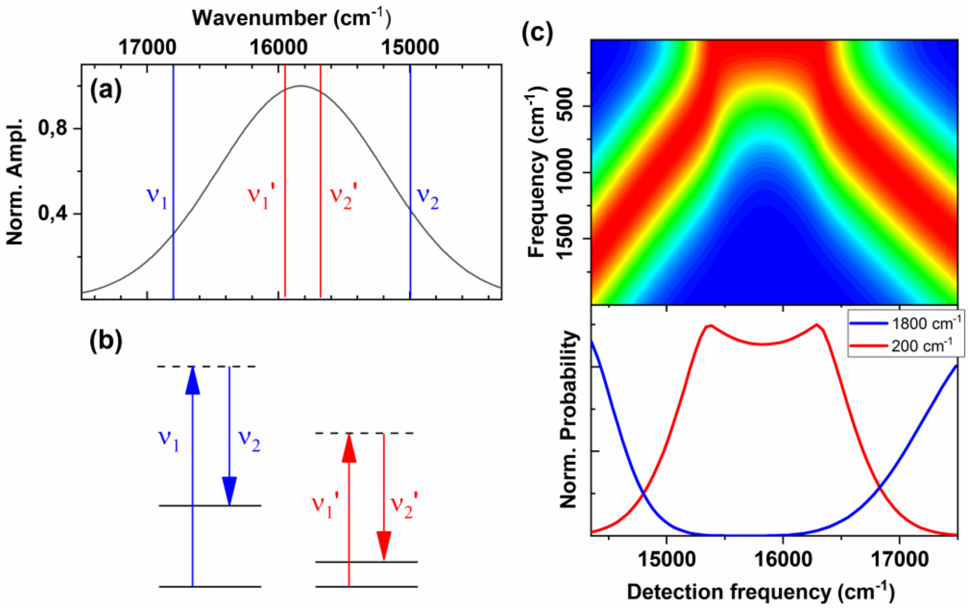

Figure 2.8: Detection frequency dependence of the four wave mixing signals. (a) A broad degenerate spectrum for the FWM pulses were simulated. The red and blue pair of vertical lines represent different pair of frequency components selected from the edge and middle of the excitation spectrum, respectively which are capable to induce the high and low frequency vibrational coherence, as depicted in (b). (c) Probability of induction of vibrational coherences of different frequency as a function of detection frequency. This data was simulated by taking spectrum as an excitation spectrum. The probability of induction of a vibrational coherence with frequencies 200 and 1800 cm^{-1} at different detection frequencies.

vibrational states widely separated in energy (Figure 2.8 (b)). On the other hand, the frequency pairs selected from middle of the spectrum have small differences in frequency and hence, they are more probable to induce low frequency coherences. Thus, the relative amplitude of high frequency coherence decreases from edge to center detection wavelength. The probability of induction of the coherence, with frequencies ranging from 0 to 2000 cm^{-1} was calculated as a function of detection frequency (Figure 2.8(c)). It has been done using Kramer-Kronig relationship,[115] which determines the frequency dependence of the emitted electromagnetic fields as a function of frequencies of the incident electric fields. Here, the spectrum shown in Figure 2.8 (a) was taken as both excitation and probing spectra for this simulation. Figure 2.8 (c) shows that indeed the relative induction probability of high frequency (e.g. 1800 cm^{-1}) coherences compared to the low frequency (e.g. 200 cm^{-1}) coherences decreases from the edge to the center detection frequencies of the corresponding employed spectrum.

Chapter 3

Experimental Details and Data Analysis

This chapter focuses on the experimental methods used for the investigations of isomerization dynamics of ASR throughout this thesis. First, the preparation of ASR sample and the HPLC analysis, used to determine the isomeric composition, have been briefly described. Later, the experimental setups required to realize the time resolved nonlinear techniques, presented in the previous chapter, have been discussed. Finally, the methodology of data analysis to retrieve the molecular information regarding the ultrafast dynamics of ASR have been elaborately presented.

3.1 Sample preparation and HPLC analysis

All the ASR samples were prepared by Dr. Kato and Yoshizumi from the group of Prof. Kandori in Nagoya Institute of Technology, Japan. The preparation of the samples was carried out according to a standard reported protocol as described thoroughly in references.[88-89, 92] In brief, a purified ASR sample was concentrated and dialyzed against a buffer solution containing 200 mM NaCl, 25 mM Tris HCl to maintain pH at 7.0. DDM (n-Dodecyl-β-D-Maltopyranoside, Anagrade, Anatrace) was added to help the protein to get stabilized by forming micelle. The concentration of DDM was kept at 0.01%, which is lower than that used in the previous report[45, 90] (0.02%). However, it was still above the critical micelle concentrations of DDM (0.007%). The purpose behind the reduction of DDM concentration was to minimize the formation of bubbles while circulating the sample through the flow cell during the femto-second measurement. High performance liquid chromatography (HPLC) and dark adaptation kinetics measurement were also done with the same concentration of DDM.

Being a photochromic light sensor, the ratio of the retinal isomers in ASR (all-*trans* and 13-*cis*) depends on the light adaptation condition. Under the dark adapted (DA) condition, it consists almost exclusively all-*trans* isomers, whereas it contains a photo-stationary mixture of all-*trans* and 13-*cis* isomers after continuous irradiation with an external light source.[89] For a quantitative determination of the isomeric ratio under two different adaptation condition, a HPLC analysis was done. The dark adaptation was realized by keeping overnight the sample in dark, whereas the light adaptation was done by continuously irradiating the sample with an external light source e.g. LED for 30 minutes. After a complete adaptation, oxime forms of the retinal isomers were extracted by adding a 1000 fold molar excess of hexane and subsequently, denaturizing with ethanol. The solvent used for the chromatography consists of 12% ethyl acetate and 0.12% ethanol in hexane. The flow rate was set at 1.0 ml/min. Since the two isomers have distinct retention times (all-*trans*: 6.1 and 12.8 min; 13-*cis*: 6.9 and 8 min), they showed distinguishable peaks in HPLC graph (Figure 7.1). The isomeric composition (Table 3.1) was determined by taking the ratio of the values obtained by integrating the area under the corresponding characteristic HPLC peak of each isomer. The values of isomeric ratio under different adaptation conditions (Table 3.1) were obtained by averaging five independent measurements.

Table 3.1: The isomeric ratio obtained from the HPLC analysis under dark and light adapted conditions.

Condition	% of all-*trans* isomer	% of 13-*cis* isomer
Dark adapted (DA)	96±2%	4±2%
Light adapted (LA)	36±3%	64±3%

3.2 Optical experimental setups

This section describes the optical experimental setups used for the femtosecond measurements. In general, a chirped pulse amplifier (CPA) system (Coherent Libra) was used as a fundamental laser

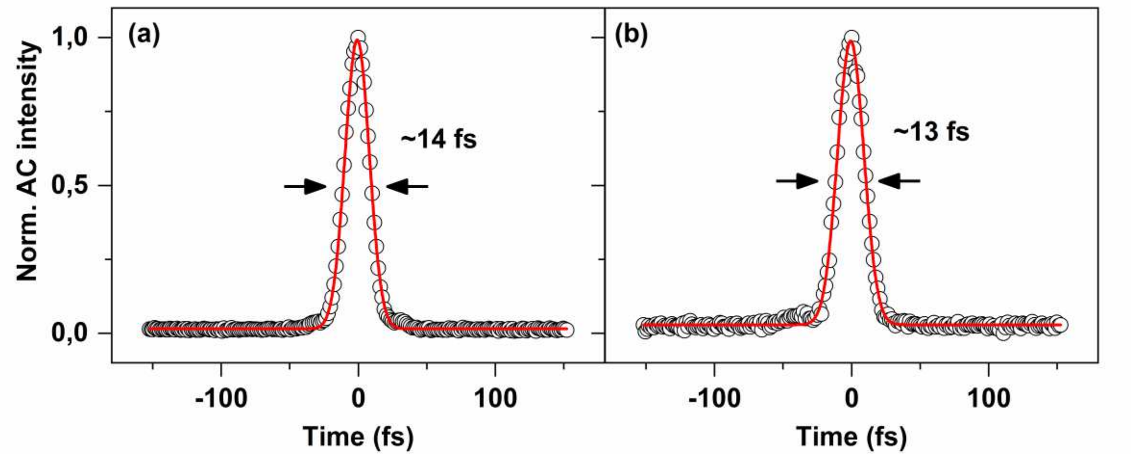

Figure 3.1: Typical auto-correlation traces of nc-OPAs after the compressors. Corresponding spectra were centered at 650 and 540 nm for (a) and (b), respectively shown in Figure 5.1. Red curves represent a Gaussian fit.

source which delivers an output spectrum centered at 795 nm wavelength at a repetition rate of 1kHz. Pulse duration was 110 fs. The energy used was about 700 μJ per pulse. This output was split into two halves to drive two home built non-collinear optical parametric amplifiers (nc-OPAs). Each nc-OPA was tunable in the visible region from about 450 to 750 nm and capable of generating ultrashort pulses with a typical time width of 13-20 fs after compression with a prism pair (Figure 3.1). The pulse durations were determined by an auto-correlator based on second harmonic signal generated by a 40 μm thick BBO crystal. The short pulse durations and spectral tunability of the nc-OPAs allowed to investigate the sub-ps dynamics of retinal proteins by probing different spectral features appearing in the spectral region from 450 to 800 nm (Figure 3.3). For this goal, four different techniques, transient absorption (TA), degenerate four wave mixing (DFWM), pump- degenerate four wave mixing (pump-DFWM) and pump-impulsive vibrational spectroscopy (pump-IVS), were exploited as discussed in Chapter 2. In the following section, the experimental setups, used for each of these experiments, are presented.

3.2.1 Transient absorption (TA)

TA requires two pulses (see Figure 2.5): one is used as a pump and other as a probe. The output from one of the two nc-OPAs was used as a pump pulse (Figure 3.2). Centre wavelength of the

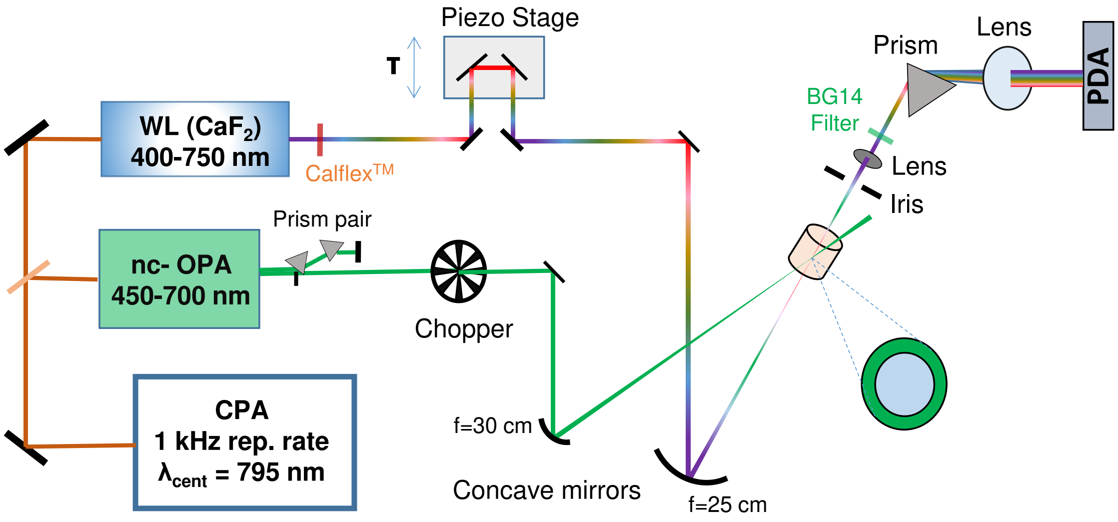

Figure 3.2: Schematic description of the experimental setup used for the transient absorption measurement. Output of nc-OPA, compressed by a prism pair, was used as pump pulse (green line) and a white light continuum was used as probe pulse. The pump was chopped with synchronized mechanical chopper. Hyper-spectral detection of the signal was done by dispersing the probe after the sample by a prism into a PDA.

excitation spectrum was tuned to the ground state absorption of the sample under investigation. For probing, a broadband white-light continuum (Figure 3.3), covering the wavelength range from 400 to 800 nm, was generated by tight focusing of ~2 nJ of the CPA output into a 2 mm thick CaF_2 crystal. CaF_2 was chosen as it shows a higher transmission in the UV-range i.e. below 450 nm compared to other materials used for the white light generation e.g. Sapphire (Figure 3.3). Probing this UV-region (400-450 nm) is crucial to track the excited state dynamics of ASR as the excited state absorption appears strongly only in this particular spectral range in within the available probing window in our setup. However, CaF_2 has a low damage threshold. In order to avoid any damage, it was placed on a mechanically rotating holder, which was rotated continuously so that the laser beam does not hit the same spot repeatedly. As an alternative to the white light, the compressed output from the other nc-OPA can also be used as probe pulse. However, for the broadband TA measurements, white light was preferred. In order to get rid of the residual of CPA output remaining in the white light continuum, a Calflex™ filter (Figure 3.3) was placed after the white light generation stage. Usually, the white light is highly chirped as it has to travel through optically dense materials causing group velocity dispersion (GVD).[119] This was taken into account during the data analysis as discussed later. The time resolution of the TA experiments was

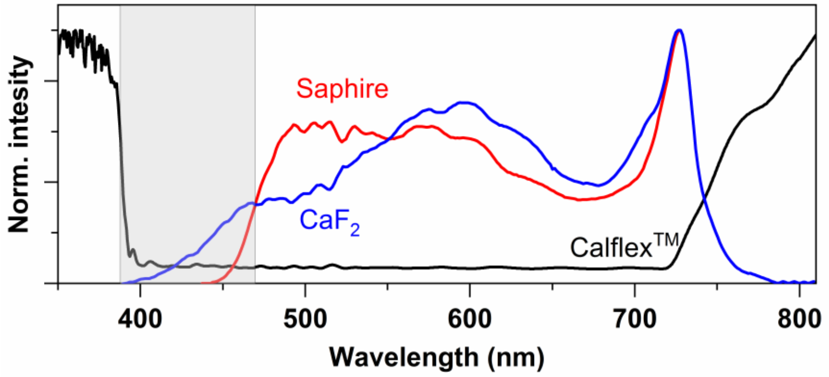

Figure 3.3: The comparison of the normalized spectra of white light continuum generated by focusing a part of the CPA output (795 nm) in a sapphire plate (red) and CaF$_2$ crystal (blue), collected after passing through a Calflex^{TM} filter. The latter show a significant intensity in the UV region (grey shaded), while the intensity of the former decays to zero below 450 nm. The normalized transmittance of the Calflex^{TM} filter is shown by the black line.

determined by fitting the coherent artifact (see section 3.3.1). This was 50±10 fs in case probing with the chirped white light and was improved to 30±5 fs, when the compressed output of nc-OPA was used as the probe pulse.

The delay between the pump and probe pulses was controlled by a piezo motor in order to realize a rapid scan.[120] Both pump and probe beams were focused and overlapped inside the sample by two different concave mirrors of a focal length 30 and 25 cm, respectively. The spot diameters of respective beams inside the sample were about 100 and 60 µm. The energy of the pump pulse was attenuated to 50 nJ which corresponds to 1.8 $\times 10^{13}$ photons/cm^2. The polarization of the pump beam was parallel with respect to white light probe. A synchronized mechanical chopper was used to block each second pump pulse so that the difference absorption (ΔA) can be calculated by taking a logarithmic difference between the intensity of probe with and without the interaction of the pump[119]:

$$\Delta A = -\log\left(I_{probe}^{pump\ on} / I_{probe}^{pump\ off}\right) \tag{3.1}$$

The pump beam was spatially filtered by an iris after the sample, whereas the probe beam was spectrally dispersed by a prism and subsequently collimated by a lens into a multi-channel detector photo-diode array (PDA) (Figure 3.2). By tuning the distance between the prism and the collimating lens, the extent of dispersion can be controlled, which in turn determines the number of pixels of the PDA illuminated by the incoming probe. In order to acquire a high S/N ratio, half of the detector array was illuminated instead of using total 256 pixels in the detector. The average spectral resolution was 2.5 nm per pixel in that case. Furthermore, a 2 mm thick BG14 filter was used to avoid oversaturation of the PDA above 500 nm without affecting the intensity at the UV-region (< 450 nm).

3.2.2 (pump-) Degenerate four wave mixing (DFWM)

A separate experimental setup compared to TA measurement was used for the (pump-) degenerate four wave mixing (DFWM) measurement. DFWM requires three pulses: pump, Stokes and probe,

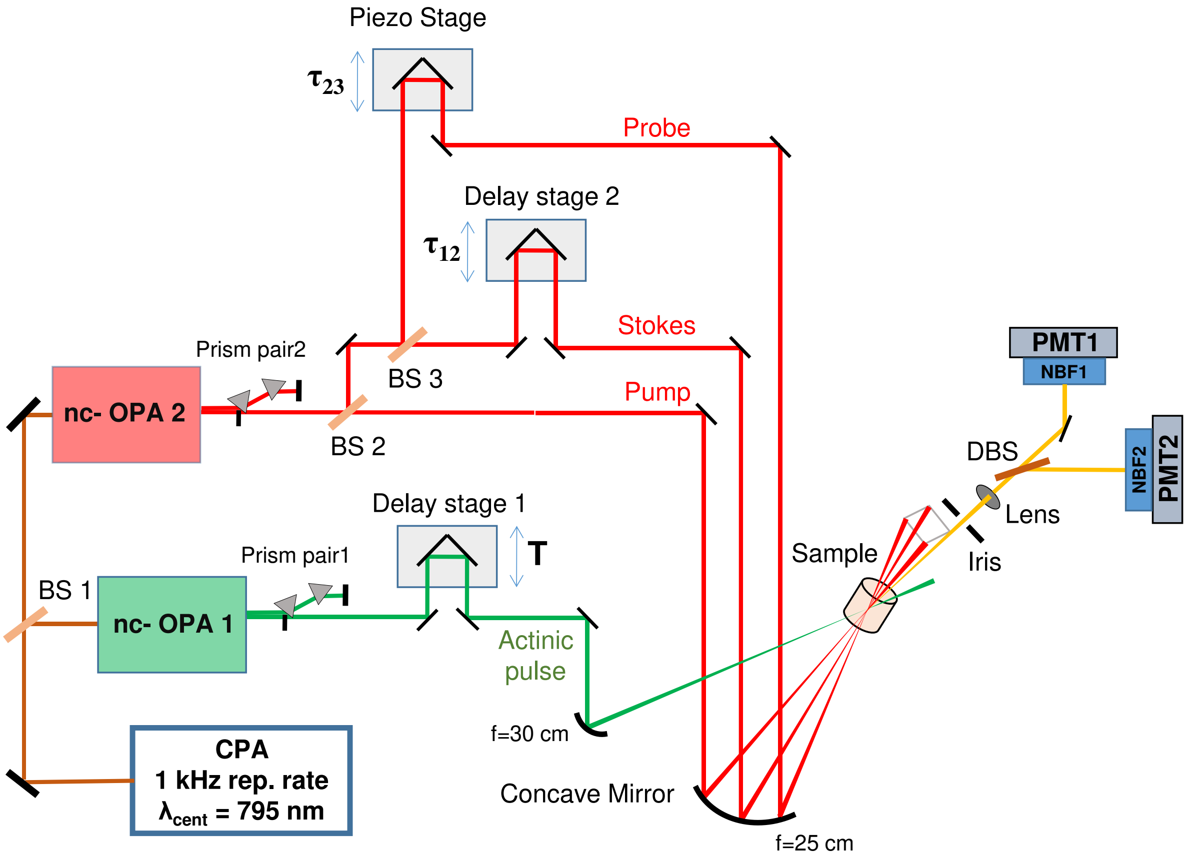

Figure 3.4: Schematic description of the experimental setup used for pump-DFWM experiment. Delay (T) between actinic pulse (green line) and DFWM pulses (pump, Stokes and probe) (red lines) was controlled by a mechanical delay stage. The delay between pump/Stokes and probe (τ_{23}) pulses was controlled by a piezo motor. The delay between the pump and Stokes pulses (τ_{12}) was kept fixed to zero for all measurements. The DFWM beams were arranged in a folded box-car geometry. Generated homodyne signal (orange line) was spectrally resolved. The signal was divided by a dichroic beam-splitter (DBS) and detected in a photo-multiplier tube (PMT) after passing through a narrow band interference filter (NBF) of 10 nm bandwidth.

with degenerate spectrum. Three pulses together are often named as DFWM pulses, which were derived by splitting the output from one of the nc-OPAs into three parts (Figure 3.4). The delays between pump and Stokes (τ_{12}) and that between Stokes and probe (τ_{23}) were finely tuned by pizzo driven computer controlled stage. While the delay τ_{23} was scanned, τ_{12} was kept fixed to zero for all DFWM measurements. In the case of pump-DFWM measurements, an additional pulse named actinic pulse (AP) is required, which is analogous to the pump pulse in the TA measurement, is preceded by the DFWM pulses. The delay (T) between AP and DFWM pulses was controlled by a mechanical delay stage. Polarizations and energies of all pulses were adjusted by placing two polarizer plates on the optical pathway of each beam before reaching the sample. The polarization of AP, pump and Stokes pulses was set parallel to the probe pulse's polarization. AP and DFWM pulses were focused and overlapped inside the sample by concave mirrors with focal length 30 and 25 cm, respectively. The spot diameters were 90 and 50 µm, respectively. The energies per pulse were set to 100 nJ for AP, 50 nJ for pump/Stokes pair and 20 nJ for the probe pulse.

The DFWM beams were arranged in a folded BOXCARS geometry.[11, 18] In this configuration, the signal was generated from the sample in a specific phase matching position and was spatially separated from the incident beams by an iris (homodyne detection). The signal was collimated by a fused silica lens and subsequently, split into two parts by a dichroic beam splitter (DBS), which allowed to record it simultaneously in two different photo-multiplier tube (PMT). A narrow band pass filter with a bandwidth of 10 nm was used in front of each PMT, which allowed a spectrally resolved detection of (pump-) DFWM signals.

3.2.3 (pump-) Impulsive vibrational spectroscopy (IVS)

The experimental setup of pump-Impulsive vibrational spectroscopy (pump-IVS) is shown in Figure 3.5. Pump-IVS, being a higher order (5th order) spectroscopic technique than TA (3rd order), requires one additional pulse (push) other than AP (analogous to pump pulse in TA) and probe as used in TA. The AP was derived from one of the nc-OPAs. The degenerate push and probe pulses, often named as IVS pulses together, were obtained by splitting the output of the other nc-OPA. Note that, the compressed output from the nc-OPA was used as probe pulse instead of the chirped white light. This is because the former provides a higher time resolution (<30 fs) than the latter (~50 fs). High time resolution is actually an essential criteria for capturing rapid molecular

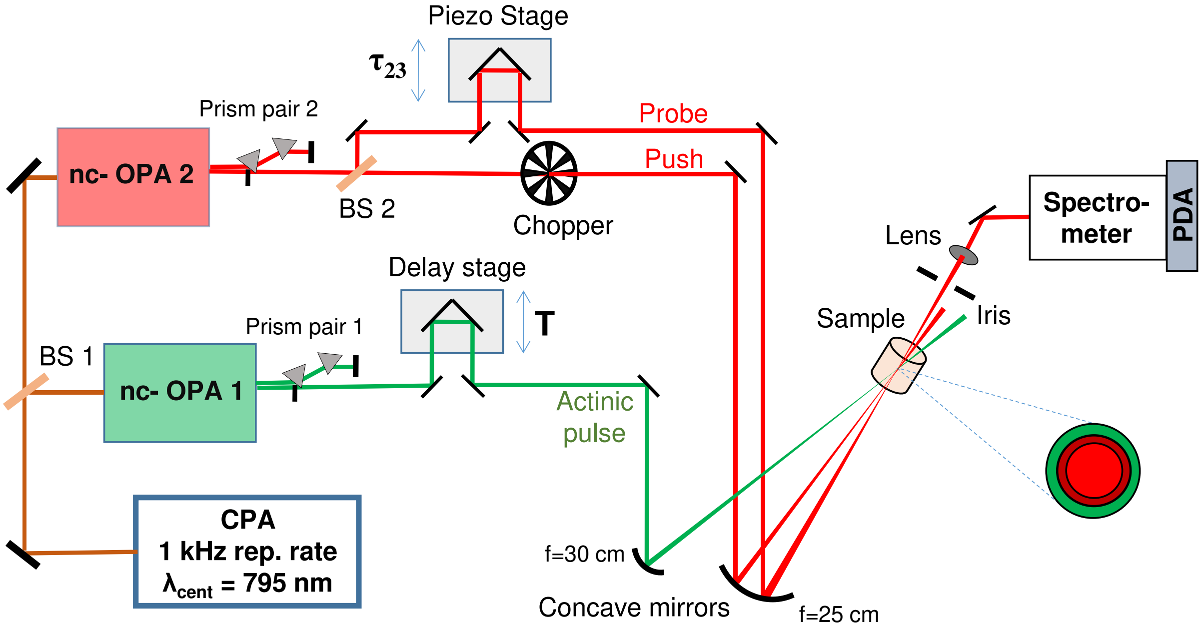

Figure 3.5: Schematic description of experimental setup used for pump-IVS experiment. Delay (T) between actinic (green line) and push (red line) pulses was controlled by a mechanical delay stage. The delay between push and probe (τ_{23}) was controlled by a piezo. A synchronized mechanical chopper was used to chop each second push pulse. The generated self-heterodyne signal was detected in a grating based PDA.

oscillations, particularly those molecular modes of RPSB, which vibrate with extremely short period (~20-40 fs).

The energies for the AP, push and probe pulses were attenuated to 100, 50 and 20 nJ, respectively. The diameters of the AP, push and probe beams inside the sample were set to 100, 80 and 60 μm, respectively. The delay between the AP and push/probe pulses were controlled by mechanical delay stage. A chopper was placed in the optical pathway of the push beam so that the IVS signal can be calculated by taking a logarithmic difference between the intensity of the probe with and without the interaction of the push pulse:

$$\Delta A = -\log\left(I_{probe}^{push\ on} / I_{probe}^{push\ off}\right) \quad (3.2)$$

The probe beam, transmitted after the sample, was spatially filtered by an iris and was attenuated by a neutral density filter to avoid the oversaturation of the detector. Subsequently, it was dispersed by a grating based spectrometer and detected in a multi-channel PDA.

3.2.4 Implementation of a flow cell setup

A flow cell setup (Figure 3.6) was implemented to circulate the sample continuously during the measurements under the above mentioned optical setup. The use of the flow cell addressed two issues: (i) Continuous exposure to the pulsed laser beam may result in formation of an undesired light induced photo-product, which may contaminate the molecular signal of ASR; (ii) the heat generated by the continuous hitting by the laser beam with the sample can cause a thermal denaturation of the protein.

Thickness of the flow cell (from *Starna Gmbh*) was 0.5 mm and the outer diameter of associated tubing (masterflex Chendurance Bio L/S 13) was 3.1 mm, which consumes total amount sample as low as 1.5 ml. With this setup, the main goal was to replenish the sample inside the cell between two consecutive laser pulses. With 1 kHz repetition rate of the laser source (Libra CPA), it needs a minimum flow rate of 4 ml/min to achieve this desired goal. This condition was met a suitable motor (Easy load II R/A 13-18), which can drive the flow cell with a minimum rate 6 ml (at 100 rpm) to maximum rate of 36 ml (at 600 rpm) per min. However, the flow rate was optimized to 6 ml per min to avoid the formation of bubbles inside the sample, which leads to a scattering of the incident light and therefore, gives rise to noise in the measured optical signals.

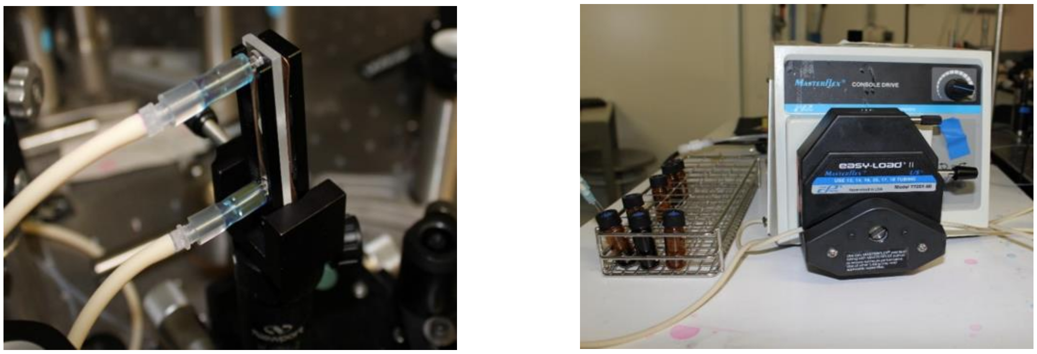

Figure 3.6: Flow cell setup: flow cell connected with the tubes (left) and the motor driving the sample inside the cell (right).

3.3 Data analysis

3.3.1 Time correction

Coherent artifact: Coherent artifacts[121] are generated by a non-linear mixing of two incident pulses, when both overlap in time domain. This artifacts are intrinsic to any multi-pulse experiments like TA, DFWM and IVS. Three different phenomena, responsible for the generation of these artifacts, are two photon absorption (TPA),[122] stimulated Raman scatterings (SRS)[123] and cross phase modulation (CPM).[124] TPA describes the simultaneous absorption of two photons from two consecutive pulses. It is usually pronounced in the UV-region (below 400 nm) as the electronic energy gaps of almost all organic solvents are resonant to the frequencies of the two photon transitions with interacting visible pump and probe pulses.[121] Since the probing window (400 to 800 nm) in all our TA measurements is well beyond the UV-region, TPA is less likely to appear in the TA data set. Furthermore, TPA increases with the intensity of the lasers and contributes significantly only under high photon fluence. As the experiments were carried out under sufficiently low photon density (<10^{14} photons/cm^2), only a minor contribution of the TPA is expected. A second contribution of coherent artifact comes from the SRS, which originates due to the frequency difference between two incident pulses. The CPM is the third and major component of the coherent artifacts appearing in all our time resolved data set, which is generated due to the phase modulation of the probe pulse by the preceding excitation laser pulse(s). This can be expressed by the following equations (see references[121] for the detailed derivation).

$$\begin{aligned} S_{CPM}(t) = {} & A_1\left(te^{-2t^2/\tau^2} - (t-\tau_{GVD})e^{-2(t-\tau_{GVD})^2/\tau^2}\right) \\ & + A_2\left((1-4\,t^2/\tau^2)e^{-2t^2/\tau^2} - (1-4(t-\tau_{GVD})^2/\tau^2)e^{-2(t-\tau_{GVD})^2/\tau^2}\right) \\ & + A_3\Big((3-4\,t^2/\tau^2)(-4\,t^2/\tau^2)e^{-2t^2/\tau^2} \\ & - (3-4(t-\tau_{GVD})^2/\tau^2)(-4\,(t-\tau_{GVD})^2/\tau^2)e^{-2(t-\tau_{GVD})^2/\tau^2}\Big) \end{aligned} \tag{3.3}$$

Here, τ is determined by the width of the cross correlation trace between the two interacting pulses, whereas τ_{GVD} depends on the group velocity mismatch originating because of their difference in refractive indexes. A_1, A_2 and A_3 are the scaling factors where, A_2 and A_3 get significant amplitude only when there is significant extent of non-linear temporal chirp in any of the two interacting pulses.

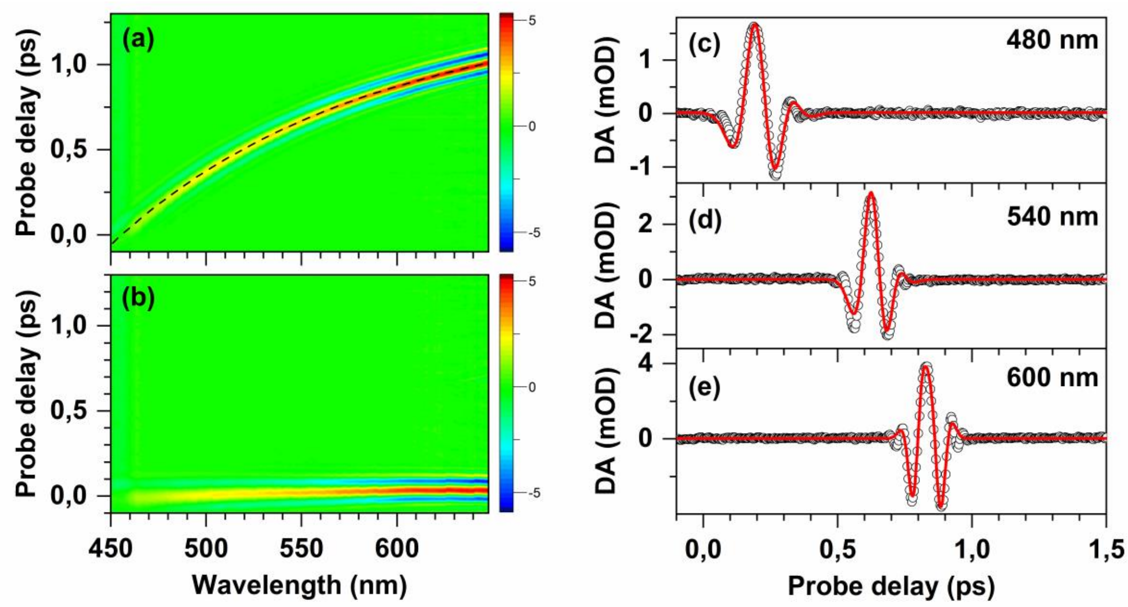

Figure 3.7: Dispersion correction of broad band TA data set. Graph (a) shows the TA data on solvent (buffer solution in this case) and (b) represents that after dispersion correction. (c) Fitting (red lines) of the coherent artifacts (black dots) at different probing wavelengths by the equation (4.3) to evaluate the time zero values. The evaluated time zero values were fitted by a 3rd order polynomial shown by a black dotted line in graph (a).

<u>Dispersion correction of TA data</u>: Different frequency component of the probe pulse overlaps with the pump pulse at different time due to the group velocity mismatch and leads to a relative time shift of the raw transients detected at different wavelengths (Figure 3.7 (a)). The coherent artifact helps to carry out the time correction of the raw data set. In order to do this time correction, the coherent artifact between the pump and probe was measured by performing a TA on the solvent, that is devoid of any molecular signal of the sample. The coherent artifact at each detection wavelength, was fitted by the equation (3.3) (Figure 3.7 (c)-(e)), which evaluates the time zero values. The evaluated time zero values were plotted as a function of the detection wavelengths and fitted by a low order polynomial (usually third order), shown as a black dotted line in Figure 3.7 (a). Afterwards the transient was shifted in time accordingly (Figure 3.7 (b)).

<u>Determination of time delay in multi-pulse experiments</u>: In order to study the transient spectral change during the ultrafast reaction (sub ps) like the retinal isomerization by multi-pulse

experiments like (pump-) DFWM or (pump-) IVS, it is very crucial to precisely determine the time delay between the employed pulses. Therefore, a pure coherent artifact between each pair of the employed pulses was measured by performing a set of TA measurement on the solvent. Each coherent artifact was fitted with equation (4.3) to evaluate the time zero value. The difference between the time zero values of the coherent artifact was taken a time delay between the corresponding pulses. For example, if the coherent artifact obtained for pump/probe and Stokes/probe pair at t_1 and t_2, respectively the difference (t_1-t_2) was taken as time delay between pump and Stoke pulses. Following this method, an error in determination of the inter pulse delay was obtained as small as ±5 fs.

3.3.2 Transient Raman spectra

The (pump-) DFWM or (pump-) IVS transients, obtained by scanning the probe delay (τ_{23}), consist of an exponentially decaying non-oscillatory component as well as an oscillatory component representing the vibrational coherences (see section 2.3 and 2.4). Therefore, in order to obtain the vibrational information, the non-oscillatory contributions in the DFWM and IVS transients, were subtracted by a bi-exponential fit (Figure 3.8 (a, b)). In each case, 1 ps of the transients was fitted,

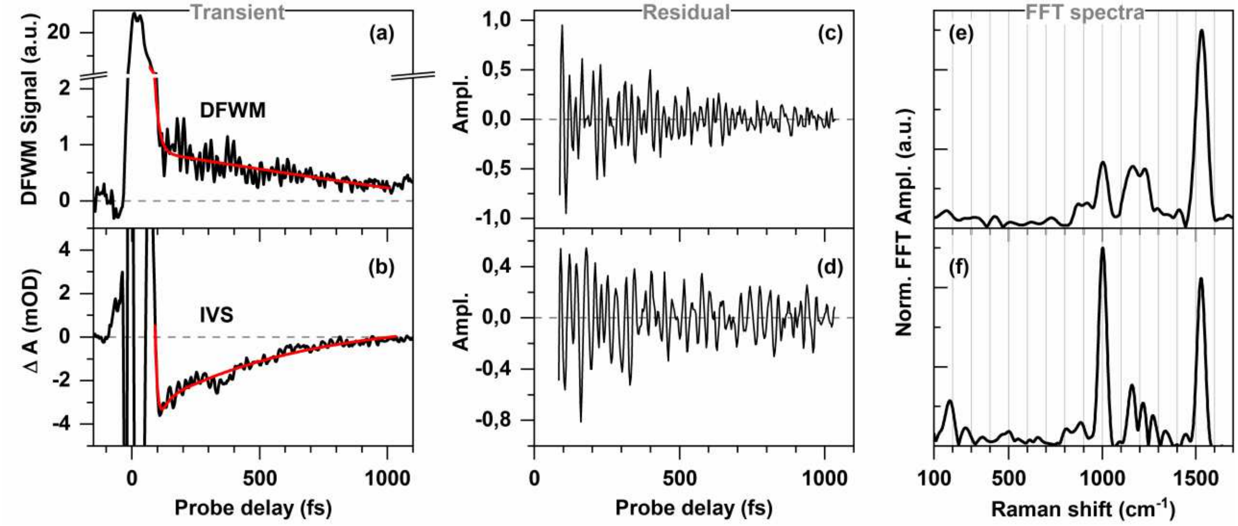

Figure 3.8: Non-resonant (a) DFWM and (b) IVS transients. The non-oscillatory signal was subtracted in each case by a bi-exponential fitting (red line) before FFT. The corresponding oscillatory signal, obtained after fitting DFWM and IVS transients, are shown in (c) and (d) respectively. Here, a Butterworth filter has been applied on the residuals to cut-off the low frequency component below 100 cm^{-1} in order to suppress noise. The corresponding FFT spectra obtained in DFWM and IVS experiments are shown in (e) and (f) respectively.

leaving out the initial ~80 fs to avoid the coherent artifact. A typical algorithm[11, 18] was followed to convert the remaining oscillatory signals (Figure 3.8 (c, d)) from time domain to the spectral domain (Figure 3.8 (d-e)). The residuals were multiplied by a Gaussian window with a FWHM of 800 fs followed by zero padding before performing a fast Fourier transformation (FFT).

DFWM vs IVS: The signal to noise ratio in the (pump-) DFWM measurements was almost one order of magnitude better than that in the (pump-) IVS measurements. For the (pump-) DFWM measurements, each transient was averaged 60 times, whereas it was averaged 600 times for the (pump-) IVS measurement to achieve a comparable S/N ratio. This difference in the S/N ratio is due to the self-heterodyne detection of the IVS signal, which suffers from the fluctuation of the intensity of local oscillator probe. In contrast, the DFWM signal, being a homodyne technique, is background free and thus, less noisy.

The widths of the Raman line, obtained from the DFWM measurements, were broader compared to that obtained from the IVS study (Figure 3.8 (e) vs (f)). This is a well-known effect of the homodyne detection in (pump)-DFWM on the decay of the oscillatory signal[118]: Oscillatory contributions in the residual decay faster in the DFWM signal compared to IVS signal (Figure 3.8 (c) vs (d)). The intrinsic interference between population grating and vibrational coherence results in a faster decay of the oscillation and consequently makes the FFT spectra broader. This also causes the small deviations in the spectral peak positions between DFWM and IVS FFT spectra (see e.g. Figure 5.2), especially for those vibrational modes (e.g. 1100-1400 cm^{-1}) which are very closely spaced.

3.3.3 Decomposition of isomeric contributions

All femtosecond studies on ASR were done under dark adapted (DA) and light adapted (LA) conditions, under which it contains distinct compositions of two ground state conformers: AT and 13C (see Table 3.1). Thus, the optical signals (e.g. absorption) under DA and LA conditions can be expressed as the linear combination of individual signals from AT and 13C isomers (Figure 4.2):

$$[\mathrm{DA}] = \mathrm{a} * [\mathrm{AT}] + (1 - \mathrm{a}) * [13\mathrm{C}] \tag{3.4}$$

$$[\mathrm{LA}] = \mathrm{b} * [\mathrm{AT}] + (1 - \mathrm{b}) * [13\mathrm{C}] \tag{3.5}$$

where, a and b are the fractions of AT-isomer presents in DA and LA sample, respectively. Here, the values of a and b are taken as 0.96 and 0.36, respectively, according to the HPLC analysis for wild type ASR reported by Cheminal *et al.*[90]. For known values of a and b, pure contributions of AT and 13C isomer can be retrieved as follows,

$$[\mathrm{AT}] = \frac{(1 - \mathrm{b}) * [\mathrm{DA}] - (1 - \mathrm{a}) * [\mathrm{LA}]}{(\mathrm{a} - \mathrm{b})} \tag{4.6}$$

$$[13\mathrm{C}] = \frac{\mathrm{a} * [\mathrm{LA}] - \mathrm{b} * [\mathrm{DA}]}{(\mathrm{a} - \mathrm{b})} \tag{4.7}$$

Retrieval of the ground state absorption spectra of the 13C isomer (see Figure 4.1) was done by following this procedure.

The TA data were also treated in the same way to separate the isomer specific contribution (see Figure 4.3). Here, the LA data set was multiplied by a factor, f, calculated from the ratio of molar extinction coefficient of AT (ε_{AT}) and 13C (ε_{13C}) form.

$$\mathrm{TA}_{\mathrm{AT}} = \frac{(1 - \mathrm{b}) * \mathrm{TA}_{\mathrm{DA}} - (1 - \mathrm{a}) * \mathrm{f} * \mathrm{TA}_{\mathrm{LA}}}{(\mathrm{a} - \mathrm{b})} \tag{4.8}$$

$$\mathrm{TA}_{13\mathrm{C}} = \frac{\mathrm{a} * \mathrm{f} * \mathrm{TA}_{\mathrm{LA}} - \mathrm{b} * \mathrm{TA}_{\mathrm{DA}}}{(\mathrm{a} - \mathrm{b})} \tag{4.9}$$

$$\mathrm{f} = \frac{\varepsilon_{\mathrm{AT}}}{\mathrm{b} * \varepsilon_{\mathrm{AT}} + (1 - \mathrm{b}) * \varepsilon_{13\mathrm{C}}} \tag{4.10}$$

f is calculated to be 1.07 assuming ε_{AT}: $\varepsilon_{13C} = 1.2$ reported earlier.[45, 90] In order to get the correct transient spectra for each isomer, multiplication with this factor is necessary because the molar extinction coefficients are different for these two isomers (see Figure 4.1) and hence, it gives rise to different amplitudes in the TA signal at same intensity of pump pulse.

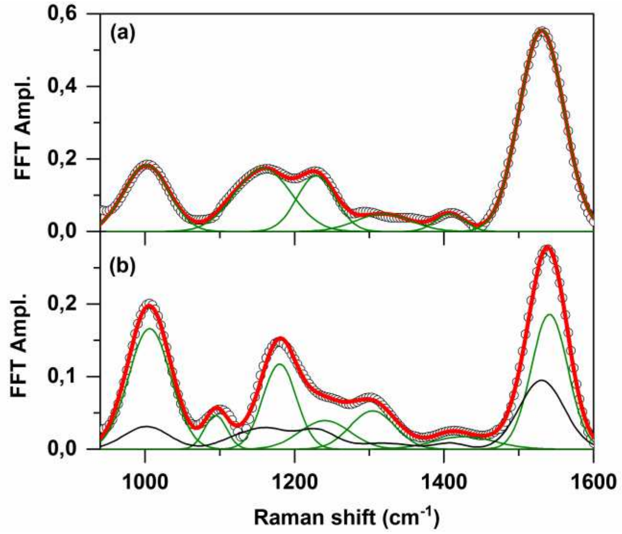

Figure 3.9: Multi-Gaussian fit of (a) DA and (b) LA non-resonant DFWM FFT spectra probed at 590 nm. The series of Gaussians represented by green curves in each graph. Black line in (b) represent the spectra of AT isomer which is kept constant during this constrained fit.

A similar concept with a slightly different approach was implemented to retrieve the pure Raman spectrum (Figure 3.8 (c)-(d)) of each individual species appearing in the photo-cycle (see Figure 1.2). For example, the ground state Raman spectrum obtained under LA condition is basically a sum of the spectra of AT and 13C ground state isomers. To retrieve the pure spectrum of 13C, it is necessary to know the spectrum of AT, which can be obtained under DA condition (~96% AT). Therefore, the Raman spectrum measured under DA condition was fitted (Figure 3.9 (a)) with equation (4.11), which is the sum over a series of Gaussians (G_i):

$$FFT_{AT\ GS} = \sum_{i}^{n} a_i * G_i\ (\nu_i, \omega_i) \tag{4.11}$$

Here, each Gaussian (G_i) represents an individual mode with the amplitude a_i, central frequency ν_i and width ω_i. Thus, all the Raman modes appearing for the AT isomer were obtained. After evaluation of pure ground Raman spectrum of AT ($FFT_{AT\ GS}$), this information can be used to disentangle the pure spectrum of 13C GS by a constrained fit:

$$FFT_{LA\,GS} = \sum_{j}^{n} a_j * G_j\ (\nu_j, \omega_j) + f * FFT_{AT\,GS} \tag{4.12}$$

Here, the fitted spectrum ($FFT_{AT\,GS}$) obtained from the previous multi-Gaussian fit was kept constant and the parameters (a_j, ν_j, ω_j) of a new set of Gaussians, which represent the modes of the 13C isomer, were varied to fit the LA non-resonant DFWM FFT spectrum (Figure 3.9 (b)). The factor, f in equation (4.11) depends on the percentage (36%) of AT present under the LA condition. Since the DFWM signal is directly proportional to the square of the molecular concentration, f should be equal to the square of the fraction of AT isomer present in LA ASR: $(0.36)^2$=0.13. The fitted value obtained for the factor (f=0.14 ±0.02) matches this value very well. The same approach was taken to obtain the spectra of the K-photoproducts of each isomer (K_{13C} and K_{AT}, see Figure 5.3).

Chapter 4

Population dynamics of Anabaena Sensory Rhodopsin

There are two main objectives of this chapter. The first motive is to compare the photo-induced ultrafast dynamics of ASR with that reported for other retinal proteins. The second as well as the major motive is to illustrate the influence of the ground state retinal configuration on the isomerization dynamics. For that purpose, the photo-induced isomerization dynamics of all-*trans* (AT) and 13-*cis* (13C) isomers of retinal protonated schiff base (RPSB), bound inside the retinal pocket of Anabaena Sensory Rhodopsin (ASR), were compared. In particular, we exploit a set of broadband femtosecond transient absorption (TA) measurements with sub-50 fs time resolution to follow the transient electronic population decay until 6 ps after the photoexcitation. First, the photo-induced dynamics of ASR have been described in analogy with that reported for other retinal proteins. Subsequently, we disentangled TA signal associated with each isomer from the raw TA data set measured under dark and light adapted conditions that comprises different ratios of ground state isomers. Finally, a global target analysis of the broadband TA data sets of AT and retrieved 13C isomers has been done with a kinetic model well known for the retinal proteins. The comparison of photo-induced dynamics of AT and 13C isomer shows that the 13C isomer has almost five fold faster kinetics compared to the AT isomer. The implications as well as the plausible reasons behind this asymmetric behavior between the photo-chemical dynamics of the AT and 13C isomers of ASR have been discussed thoroughly.

4.1 Ground state absorption spectrum

Ground state absorption spectrum of ASR under dark adapted (DA) condition is centered at 548 nm (Figure 4.1 (a)) and contains almost exclusively AT isomer (Figure 4.1 (b)). A continuous irradiation for 30 minutes with a light source (LED) with a center wavelength of 590 nm (illumination spectrum shown by orange line in Figure 4.1 (a)) causes ASR to reach a light adapted (LA) steady state photo-stationary equilibrium between the isomers. In this state, it contains a mixture (64% 13C and 36% AT) of the isomers (Figure 4.1 (b)). It results in a hypsochromic shift and reduction in intensity of the ground state absorption spectrum. This is due to the major contribution of the 13C isomer (64%) (Figure 4.1 (b)), which has smaller molar extinction coefficient and ~10 nm blue shifted λ_{max} compared to the AT isomer.[45, 90]

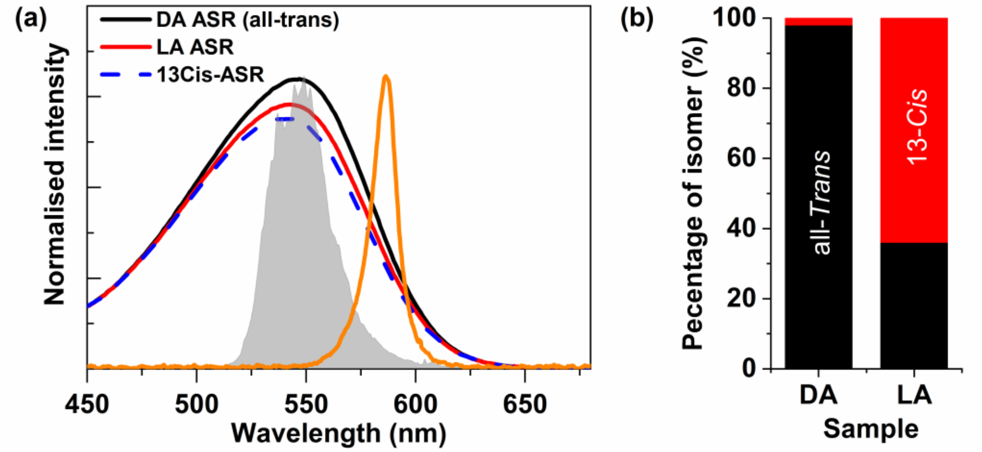

Figure 4.1: (a) Absorption spectra of wild type ASR under dark (black) and light (red) adapted conditions. The pure ground state spectrum of the 13C-isomer (blue dashed) has been calculated by taking a linear combination (exploiting equation (4.6) and (4.7)) of the dark and light adapted spectra using the known isomeric ratio, obtained from the HPLC analysis. Filled grey and solid orange curves in (a) represent excitation and illumination spectrum, respectively. (b) Percentage of all-*trans* (black bar) and 13-*cis* (red bars) isomers of ASR under the DA and LA conditions.

4.2 Pump-probe measurements

Since ASR contains widely different isomeric ratios (Figure 4.1 (b)) in the two different adaptation (DA vs LA) conditions, it is possible to compare the isomerization dynamics of AT and 13C isomers by measuring the transient optical signals (e.g. absorption, fluorescence)[45, 90]. For that purpose, a set of transient absorption measurements was carried out under the DA and LA conditions. The experimental setup used for this study has been explained schematically in Figure 3.2 of the previous chapter. Here, the excitation spectrum was centered at the maxima of the ground state absorption spectra (Figure 4.1(a)) and a white light continuum covering the wavelength range from 400 to 720 nm (Figure 3.3) was used as the probe spectrum. The time resolved UV-Visible broadband difference absorption spectra of wild type ASR, measured under the DA and LA conditions, are shown in Figure 4.2. In both data sets, a fast decaying positive

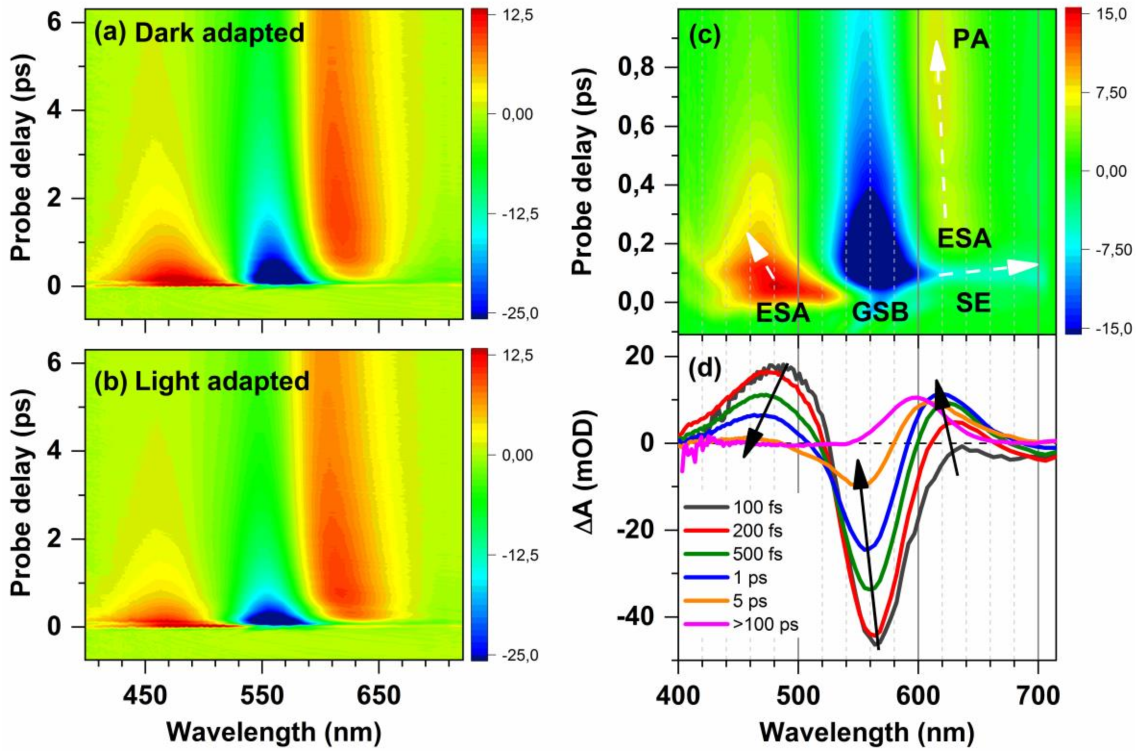

Figure 4.2: Time resolved difference absorption spectra of wild type ASR measured under (a) dark and (b) light adapted conditions. (c) Initial 1 ps of this spectro-temporal evolution of the difference absorption spectra under light adapted condition. Different characteristic peaks: Excited state absorption (ESA), Ground State Bleach (GSB), Stimulated Emission (SE), Photo-product absorption (PA) appear along the probe delays are marked. (d) Spectral cuts at selected probe delays. The transient spectral shifts are shown by the arrows in both (c) and (d).

(~490nm) and negative (~560nm) bands can be observed. These bands are assigned to the excited state absorption (ESA) and ground state bleach (GSB) of the ASR, respectively.[45, 90] In addition, a red shifted positive signal (~620nm) with a delayed rise and slow decaying kinetics can also be detected in both cases. This is assigned to a photo-induced absorption (PIA) band.

A closer look at the initial 1 ps dynamics of these three bands (Figure 4.2 (c)) show that soon after the excitation, an ESA appears around 490 nm. This undergoes a blue shift and decays rapidly in sub-ps time scale. Along this, a red shift of the stimulated emission (SE) band from 620 nm to 700 nm can also be clearly observed in earlier time (<200 fs). Both of this spectral shifts represents an initial excited state relaxation.[45, 90] In addition, a PIA band around 630 nm, which is assigned to a red shifted ESA band, remains covered by the SE band in earlier probe delays and starts to appear only around 200 fs. Afterwards, this photo-induced absorption band rises to reaches the maximum of the TA signal around 600 fs. The rise of this band indicates the formation of a hot photoproduct, which is usually named as ‘J’-intermediate in the photochemistry of rhodopsin.[28, 85] Subsequent decay (<100 ps) along with a continuous red shift of this photoproduct absorption (PA) band hints a vibrational relaxation of the hot intermediate to a nanosecond lived ‘K’-intermediate: all-*trans*, 15-syn for 13C and 13-*cis*, 15-trans for AT (see the photocycle of ASR in Figure 1.2).[45, 89]

4.3 Comparison of isomerization dynamics of AT and 13C isomer

The photo-induced isomerization dynamics associated with each isomer were retrieved by taking a linear combination on the and TA signal measured under the DA and LA conditions (Figure 4.3). Despite the similar appearance of all three characteristic spectral bands and their shifts in the TA data, as discussed in previous section, the 13C-isomer shows faster kinetics compared to the AT isomer at all probing wavelengths. This dynamical difference is depicted clearly in Figure 4.3 (c)-(e). It illustrates that the decay of the ESA (λ_{Probe}=450 nm), the recovery of the GSB (λ_{Probe}=550 nm) as well as the formation of first photoproduct ‘J’ (λ_{Probe}=620 nm) are accelerated for the 13C isomer compared to the AT isomer. This drastic difference in kinetics between these two isomers has been quantified by a bi-exponential fit (Table 4.1) of each transients leaving initial 120 fs to avoid the coherent artefact. It reveals that the initial dynamics of the 13C isomer is more than 2-fold faster than the AT-isomer. For example, the initial ESA signal at 450 nm decays with

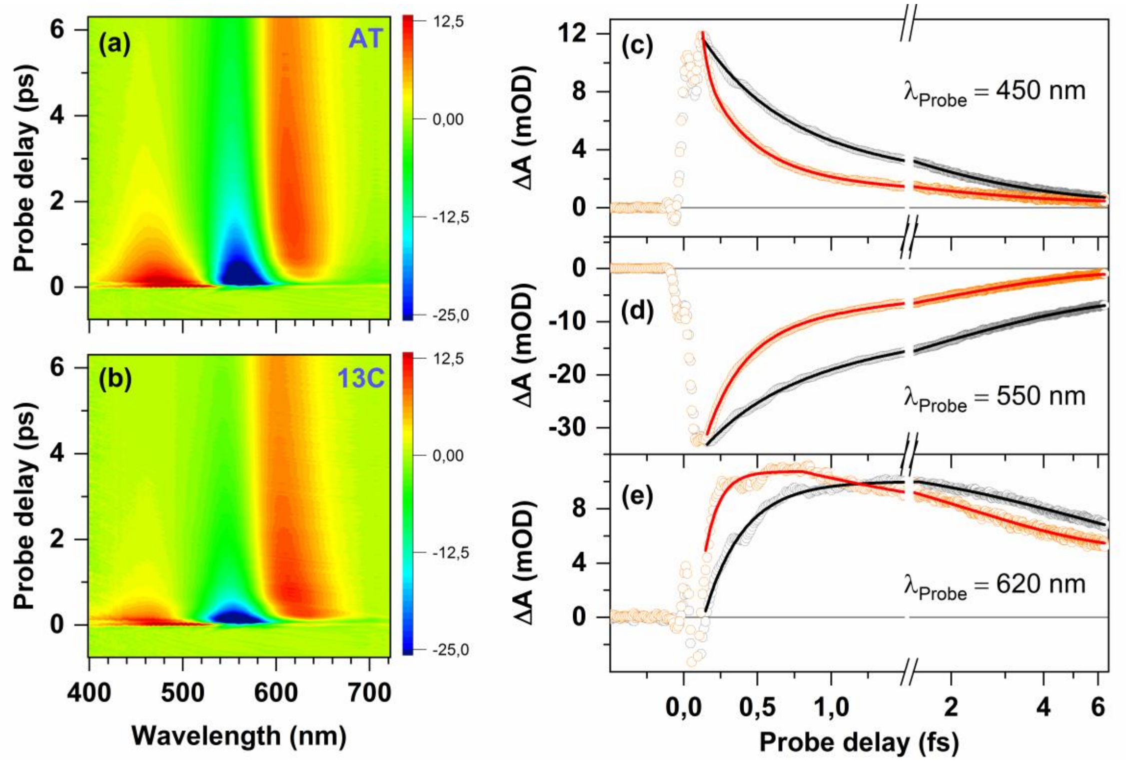

Figure 4.3: Pure contributions of (a) AT and (b) 13C-isomer of wild type ASR on Pump-probe signal, retrieved from that TA data sets measured under dark and light adapted conditions (Figure 4.1) using equations (5)-(7). The transient at three different probing wavelengths: (c) 450 nm, (d) 570 nm and (e) 620 nm for AT (grey) and 13C (orange) isomers are shown on right. Each of the transients are fitted with a bi-exponential model: double decay model for (c) and (d) whereas, a model including a rise and decay component for (e).

Table 4.1: Time constants obtained by bi-exponential fitting of the transients. The transient were taken at different probing wavelengths under DA (~AT), LA conditions and also for retrieved 13C-isomer. The transients at 450 and 550 nm were fitted with bi-exponential decay model (τ_{dec1} and τ_{dec2}) whereas the transients at 620 nm were fitted with bi-exponential one rise-one decay model (τ_{rise} and τ_{dec}) as depicted in Figure 4.3(c)-(e).

Sample	**λ_{Probe}=450 nm**		**λ_{Probe}=550 nm**		**λ_{Probe}=620 nm**	
	τ_{dec1}	**τ_{dec2}**	**τ_{dec1}**	**τ_{dec2}**	**τ_{rise}**	**τ_{dec}**
DA/ AT	510 ±5 fs	2.0 ±0.1 ps	540 ±8fs	2.6 ±0.1 ps	260 ±7fs	5.0 ±0.2 ps
LA	260 ±10 fs	1.3 ±0.1 ps	280 ±5 fs	2.2 ±0.1 ps	130 ±10 fs	3.2 ±0.1 ps
13C	220 ±7 fs	1.2 ±0.1 ps	270 ±8 fs	2.1 ±0.1 ps	100 ±8 fs	2.2 ±0.1 ps

a time constant (τ_{dec1}) of 510 ±5 fs for the AT isomer, whereas, it decays with a time constant of 220 ±7 fs for 13C isomer. Similarly, a stark contrast in the kinetics has also been observed for the rise (τ_{grow}) of the photo-induced absorption band (mixed with ESA and PA): it rises with a time constant (τ_{grow}) of 260 fs for the AT, whereas it is about 100 fs for the 13C.

4.4 Global target analysis

In order to obtain more physical insight into the differences of the dynamics of the AT and 13C isomers of ASR, a global target analysis of the TA data set was carried out. For that, a physically relevant five-component sequential model, which has been well-accepted[44-45, 72, 79, 96, 125-130] for other microbial retinal proteins (MRP's) (such as bacteriorhodopsin, halo-rhodopsin, chanello-rhodopsin, proteo-rhodopsin), was chosen:

$$A \overset{t_1}{\rightarrow} A_1 \overset{t_2}{\rightarrow} I \overset{t_3}{\rightarrow} J \overset{t_4}{\rightarrow} K \overset{t_5}{\rightarrow}$$

In the context of retinal photochemistry, A represent the Frank-Condon excited species, formed just after the excitation, whereas A_1 represents the species generated by the relaxation of the initially excited species via bond length alternation. The decay of the species, A_1 leads to the

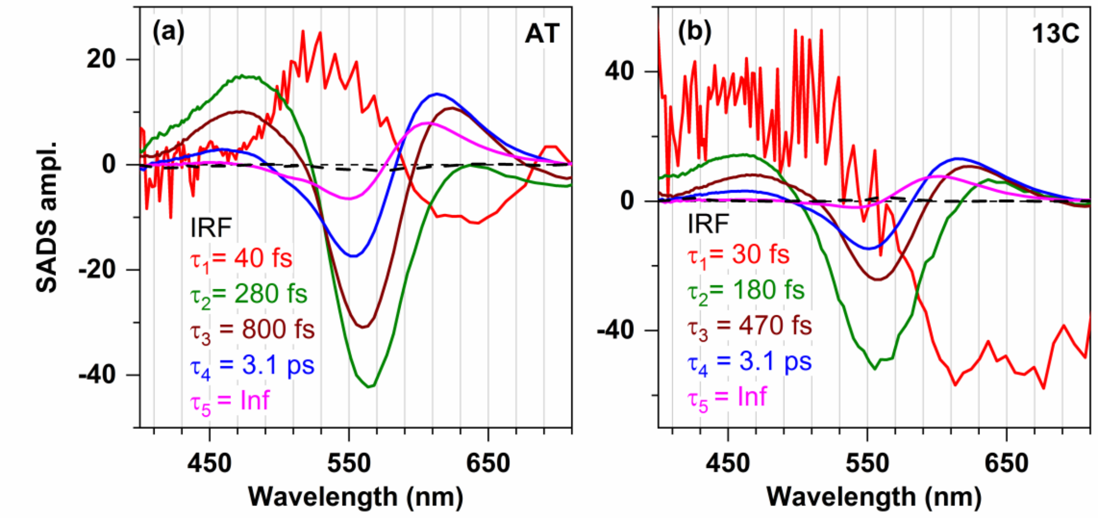

Figure 4.4: Species associated difference absorption spectra (SADS) of (a) AT and (b) 13C isomer obtained from the global fitting with 5 components sequential model. Black dotted curve in each graph represents the instrumental response functions (IRF). Red, green, brown, blue and magenta curves represent the first, second, third, fourth and fifth species, respectively. Associated time constants for each SADS are shown in each graph.

Table 4.2: The parameters obtained by global fitting of pump-probe data sets for AT and 13C isomers of wild type ASR by a five component sequential model: A→A_1→I→J→K→

Sample	t_1	t_2	t_3	t_4	t_5
AT	40 fs (±10)	280 fs (±30)	800 fs (±20)	3.1 ps (±0.3)	Inf
13C	30 fs (±10)	180 fs (±30)	470 fs (±30)	3.1 ps (±0.2)	Inf

formation of a fluorescent intermediate, *I*. The species *K* is known to be the long lived (~µs) photo-product formed after the internal conversion. In fact for bacteriorhodopsin, species *I* and *K* are a well-defined intermediate (I_{460} and K_{610}), which show their absorption maxima at 460 nm and 610 nm, respectively.[28, 44, 72, 79, 131]

The species associated difference absorption spectra (SADS) (Figure 4.4) for both AT and 13C isomers were calculated by an iterative global fitting algorithm with the aforementioned sequential model. The fitting was able to reproduce more than 99% of the experimental data. The SADS obtained by this analysis matches well with that reported by Wand *et al.*[45] The time constants associated with each SADS are summarized in Table 4.2, which also agrees with the reported values.[45] However, the error bars for the determination of the time constants has been improved at least by a factor of three in our study compared to that reported earlier[45] because of the higher S/N ratio in the pump-probe signals (see section 3.2.1).

In line with the previous analysis of bi-exponential fitting (Figure 4.3), the global target analysis with aforementioned model reveals a faster deactivation kinetics for the 13C isomer compared to the AT isomer (Figure 4.4). A comparison of SADS of the first transient species (red line in Figure 4.4) appearing for AT and 13C isomers shows a stronger amplitude at the red wing (> 600 nm) for the latter compared to the former. However, the value of this time constant (t_1) appears to be the same (~30-40 fs) for both AT and 13C isomers within the precision of our measurement. The main difference in kinetics between AT and 13C isomers appears for t_2 and t_3 (Table 4.2), which correspond to the formation of *I* and J species, respectively. The formation of J-species is almost 2-times faster for the 13C isomer compared to the AT isomer. In contrast, t_4, which indicates the relaxation of the hot-photo intermediate 'J', appears to be the same for both isomers.

4.5 Discussion

The broadband TA measurements on ASR illustrates the evolution of the transient electronic spectra as the reaction proceeds. All the general appearance of the spectral bands for ASR (under both dark and light adapted conditions), are reminiscent to that reported for other microbial retinal proteins like bacteriorhodopsin,[44, 72, 79, 125, 130] halo-rhodopsin,[96, 126-127, 132] chanello-rhodopsin,[133] proteo-rhodopsin[128-129]. A stimulated emission band in the near infrared region as well as a blue shifted excited state and a red shifted photo-product absorption spectra compared to the ground state absorption spectra, as observed in the TA data of ASR (Figure 4.2), are quite common characteristics for all these microbial retinal proteins (see Figure 4.5). In addition, the transient spectral shifts of these bands during the reaction (blue shift of ESA and red shift of SE band) are also qualitatively similar (Figure 4.5).

The photo-induced dynamics of ASR has been further analyzed by the global target analysis (Section 4.4) using a kinetic model, which has been proposed earlier to describe the retinal isomerization dynamics. It estimates the first time constant (t_1) as 30-40 fs, which is believed to be associated with a rapid excited state relaxation ($A \rightarrow A_1$) via a structural reorganization of the retinal moiety. This timescale is also in good agreement with that reported for bacteriorhodopsin[134]

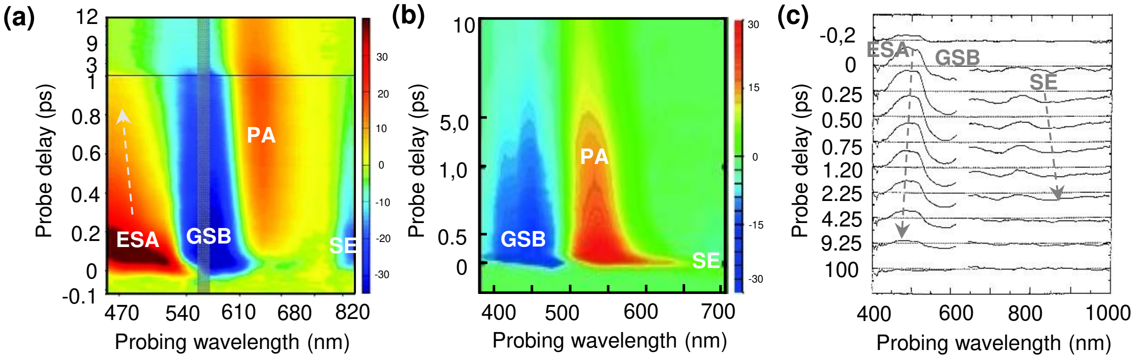

Figure 4.5: Photo-induced isomerization dynamics of (a) bateriorhodopsin, (b) chanello-rhodopsin and (c) halo-rhodopsin measured by transient absorption spectroscopy. Different characteristic bands: ground state bleach (GSB), excited state absorption (ESA), stimulated emission (SE) and photo-product absorption (PA) are shown. Shifts of the spectral bands are highlighted by the white dotted arrows. The graph (a), (b) and (c) are adapted with permissions from the following references: Wand *et al.*[130] (copyright 2012 American Chemical Society), Verhoefen *et al.*[132] (copyright 2010 Wiley-VCH Verlag GmbH & Co) and Kobayashi *et al.*[132] (copyright 1998 American Chemical Society), respectively.

as well as with that predicted by a quantum chemical calculation on visual rhodopsin.[77] Furthermore, the SADS of species 'I' and 'K' match well with the spectrum of the fluorescent state, I_{460} and the long lived sub-μs intermediate, 'K_{610}' of bacteriorhodopsin, respectively.[131, 135-137] Moreover, we observed a non-exponential decay during the internal conversion in analogy with the previous report.[45] In general, the multi-exponential nature of the internal conversion kinetics are quite common features among all the retinal proteins.[44, 72, 79, 96, 125-129, 138] It is interpreted as the channelization of the excited state population to different routes, which lead to either reactive or non-reactive pathways.[44, 126, 139-140] This bifurcation may arise due to an inhomogeneous charge distribution surrounding the retinal chromophore inside the retinal pocket or because of the nature of the excited state topology.[44, 139-140] Whatever it is, this multi-exponential kinetics can be reasonably described as bi-exponential (I→J→K) for both isomers of ASR. Nevertheless, it must be kept in mind that this bi-exponential kinetics is only a crude approximation of a continuous distribution lifetimes[44] representing different reaction channels.

In spite all these qualitative similarities in the appearances of transient species of all microbial retinal proteins including ASR, the reaction rates are found to be widely different as shown in Table 1.1. This infers that the extent of change in electrostatic interaction between the RPSB and surrounding amino acid residues from one to other protein are not large enough to affect the overall electronic spectral features of the transient species, but significant enough to influence the isomerization dynamics.

The influence of the ground state retinal configuration was evaluated by comparing two opposite coordinates of the retinal isomerization reaction i.e. AT to 13C and 13C to AT, within the same protein environment. While the former reaction can be directly accessed from the TA signals measured under the DA condition, the latter needs the retrieval of the associated dynamics from the data set measured under the LA condition. Eventually, the TA signals measured under both DA and LA conditions show very similar gross spectral evolution. However, retrieval of the pure TA signal associated with 13C isomer was possible by subtracting the counterpart of AT signals from LA data set (Section 3.3.3). A comparison of AT and retrieved 13C isomer kinetics reveals a striking dynamical difference. The global target analysis further points out that the AT and 13C isomers differ only in the sub-ps kinetics, whereas the relaxation of the photo-product appears to be the same for both (Section 4.4). In spite of the observation of this difference in kinetics, it is difficult to quantitatively estimate and compare the excited state lifetimes of the AT and 13C ASR.

This is because none of the spectral region within the probing window (400-720 nm), available in this experiments, show any pure excited state dynamics; rather it is always partially overlapped with the GSB signals. However, a quantitative estimation of the excited state lifetimes has been done by Cheminal *et al.*[90] comparing the transients in the near infrared region (>800 nm), where a pure excited state emission band appears i.e. devoid of any ground state dynamics. In addition, it reports an excited state lifetime of 770 ±20 fs and 170 ±40 fs for AT and 13C isomer, respectively. This study also reports a higher relative quantum yield for the AT isomer compared to the 13C isomer, which is in agreement with the absolute quantum yield values estimated by Kawanabe *et al.*: AT (0.24) and 13C (0.38).[89]

The striking contrasts between the reaction rates and quantum yields for the retinal of two different ground state configurations has a profound significance in the context of retinal photochemistry. In this regard, a similar comparison of the reaction rates of 11-*cis* and 13-*cis* with all-*trans* retinal protonated schiff bases (RPSB) in organic solvents showed that *cis*-conformers are only marginally accelerated compared to *trans*-isomers.[26] In contrast, 13C isomer of BR shows almost three times shorter excited state lifetime compared to AT isomer.[130] It is almost 5 times in case of ASR. This has been qualitatively rationalized by a quantum chemical trajectory calculation,[91] which predicts an asymmetric nature in the excited potential energy surface. More specifically, it shows presence of a barrier in the pathway of AT isomer, whereas the same feature is absent for 13C isomer. This causes a dynamical trapping of the excited state population and therefore, it causes a deceleration in the internal conversion rate. These results infer that the same opsin moiety can interact with the two bound retinal isomers different and lead to an asymmetry in two optically active reversed reactions. This disparity in the electrostatic interaction hints at the difference between the bindings of the AT and 13C isomers inside the retinal pocket, which may arise due to difference in geometrical strains generated to fit the specific isomer inside the retinal cavity. In past, protein catalyzed pre-distortion of the ground state structure[49, 80-81, 84, 141-144] has been proven to accelerate the isomerization kinetics for the visual rhodopsin, which exhibits the fastest isomerization rate[29-30, 68] among the family of retinal proteins. However, X-ray crystallography study indicated no significant difference in torsion around active $C_{13}=C_{14}$ bond of the AT and 13C isomers in ASR.[50] Till the date only indirect evidence, which might explain the observed asymmetric photo-chemical dynamics, comes from a FTIR study.[145] This study captures the movement of the amino acid residues connected to the retinal chromophore by tracking FTIR spectral signatures before and after (>100 ps) the completion of isomerization. This comparison showed a larger rotation of the schiff base moiety and consequently a stronger disruption of H-bond attached to the schiff base N-atom for the AT isomer compared to the 13C isomer. This might explain why the AT isomer takes longer time to accomplish the isomerization compared to the 13C isomer. However, this picture is hard correlate with the observation of the energy barrier along the excited trajectory.[91] This is because FTIR study[145] shows the structural difference only before and after (>100 ps) the completion of the isomerization reaction, but tells nothing about the structural change during the excited state evolution of the system from the Franck-Condon excited state to the ground states via the conical intersection. Therefore, it is necessary to track the sub-ps structural changes of the retinal in order to rationalize the molecular reason behind this asymmetric toggling of retinal chromophore in ASR, which will be the presented in the next chapter.

4.6 Conclusion

We present a femtosecond transient absorption study of retinal isomerization of ASR, which accommodates both AT and 13C isomers inside the retinal pocket. The comparison shows a large disparity in the photo-induced reaction dynamics of AT and 13C isomer. The 13C isomer shows a ballistic kinetics and the isomerization completes within 200 fs, which is very similar to visual rhodopsin. The AT isomer shows, about five fold slower kinetics, which is reminiscent to bacteriorhodopsin. In the view of very similar accelerated dynamics for the *cis*-isomers of ASR (13-*cis*), visual rhodopsin (11-*cis*)[29-30] as well as bacteriorhodopsin (13-*cis*),[130] it reiterates the question, whether the ground state retinal configuration is the sole factor to govern the isomerization dynamics. However, a large difference in dynamics between rhodopsin (11-*cis*) and iso-rhodopsin (9-*cis*), both incorporating a cis-conformation in the ground state, speaks against this generalization.[140] Nevertheless, both *cis*-conformers are relatively faster than all-*trans* isomer. This stark contrast of photo-induced dynamics inside the same protein architecture raises the fundamental question about the factor differentiating the protein catalyzed isomerization reaction of the *trans* and *cis* isomers of RPSB. This, in turn, raises the demand to track and compare the structural changes of each isomer as the reaction proceeds, which will possibly reveal the molecular reason behind the asymmetric toggling.

Chapter 5

Vibrational dynamics of Anabaena Sensory Rhodopsin[1]

A large difference in the isomerization dynamics and quantum yields of the all-*trans* (AT) and 13-*cis* (13C) isomers of bound retinal protonated Schiff base (RPSB) inside the protein cavity of Anabaena Sensory Rhodopsin (ASR) has been reported in the previous chapter. This raises the question about the mechanistic origin behind this difference. One way to unveil the reason would be to track and compare the structural change of the AT and 13C RPSB during the time span (<ps) of the isomerization reaction. In this chapter, we apply coherent Raman spectroscopic techniques like pump-degenerate four wave mixing (pump-DFWM), pump impulsive vibrational spectroscopy (pump-IVS) to capture the excited state structural change. Our findings point to distinct features in the ground state structural conformations as well as to drastically different evolutions in the excited state manifold of the AT and 13C isomers. The ground state vibrational spectra show stronger Raman activity of the C_{14}-H out-of-plane wag (at about 805 cm^{-1}) for the 13C isomer than for that of the AT isomer, which hints at a larger pre-distortion for the former in the ground state. Evolution of the Raman frequency after interaction with actinic pulse shows a blue shift for the C=C stretching and CH_3 rocking mode for both isomers. For the AT, however, the blue shift is not instantaneous as observed for the 13C isomer, rather it takes more than 200 fs to reach the maximum frequency shift. This frequency blue shift has been rationalized by a decrease of the effective conjugation length during the isomerization reaction, which further confirms a slower

---

[1] This chapter includes a part of the contents (e.g. data, figures, text) used in the manuscript: "*Mapping the ultrafast vibrational dynamics of all-trans and 13-cis retinal isomerization in Anabaena Sensory Rhodopsin*", P. P. Roy, Y. Kato, R. Abe-Yoshizumi, E. Pieri, N. Ferré, H. Kandori and T. Buckup, submitted to *Phys. Chem. Chem. Phys.*, August 29, 2018.

formation of the twisted state for the AT isomer and corroborates the presence of a barrier in the excited state trajectory previously predicted by quantum chemical calculation.

5.1 Results of non-resonant DFWM experiments

DFWM and IVS experiments, with a DFWM/IVS excitation spectrum, almost non-resonant to ASR ground state absorption (Figure 5.1), were carried out to capture the ground state (GS) vibrational spectra. The FFT spectra obtained after the subtraction of non-oscillatory contributions from the transients (see section 3.3.2), show the activity majorly in the high frequency region (>1000 cm^{-1}) in both DFWM (Figure 5.2 (a)-(d)) and IVS (Figure 5.2 (e)-(h)) experiments. A weak activity in the low frequency region (< 400 cm^{-1}) was also observed, especially at the detection wavelength at 630 nm, where the relative amplitudes of the high frequency (>1000 cm^{-1}) modes are lowered. This variation of relative intensity of low and high frequency modes from the edge (590 nm) to the center (630 nm) detection wavelength of DFWM/IVS spectrum are in agreement with the natural spectral dependence of non-linear signal in CARS-based schemes[118] (see also section 2.5).

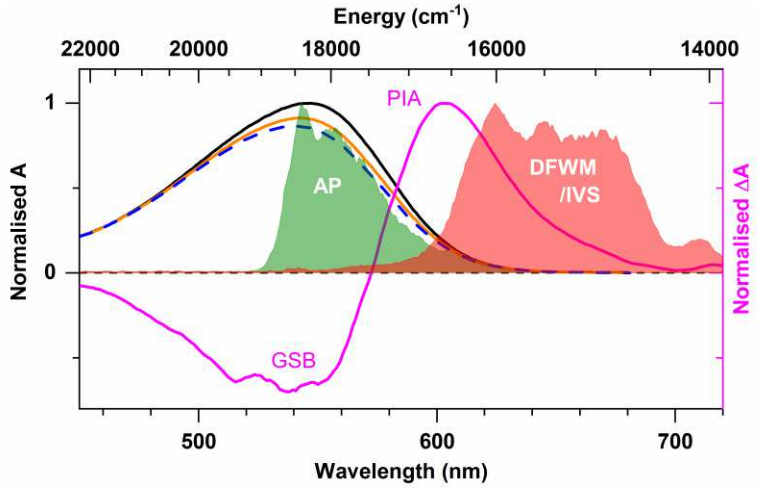

Figure 5.1: Ground state absorption spectra of ASR in dark (AT) and light adapted (mixture of AT and 13C) conditions are shown by black and orange lines, respectively. The spectrum of pure 13C isomer (blue dotted line) was derived by taking linear combination of the dark and light adapted absorption spectra using known isomeric ratio. Normalized difference absorption (ΔA) spectra at pump-probe delay of 100 ps is shown by the magenta curve. Different characteristic bands: GSB (ground state bleach) and PIA (photo-induced absorption) are shown. Green and red (solid in (a) and line in (b)) curve represent the spectrum of the Actinic Pulse (AP) and degenerate pump/stokes/probe (DFWM) or push/probe (IVS) spectrum, respectively.

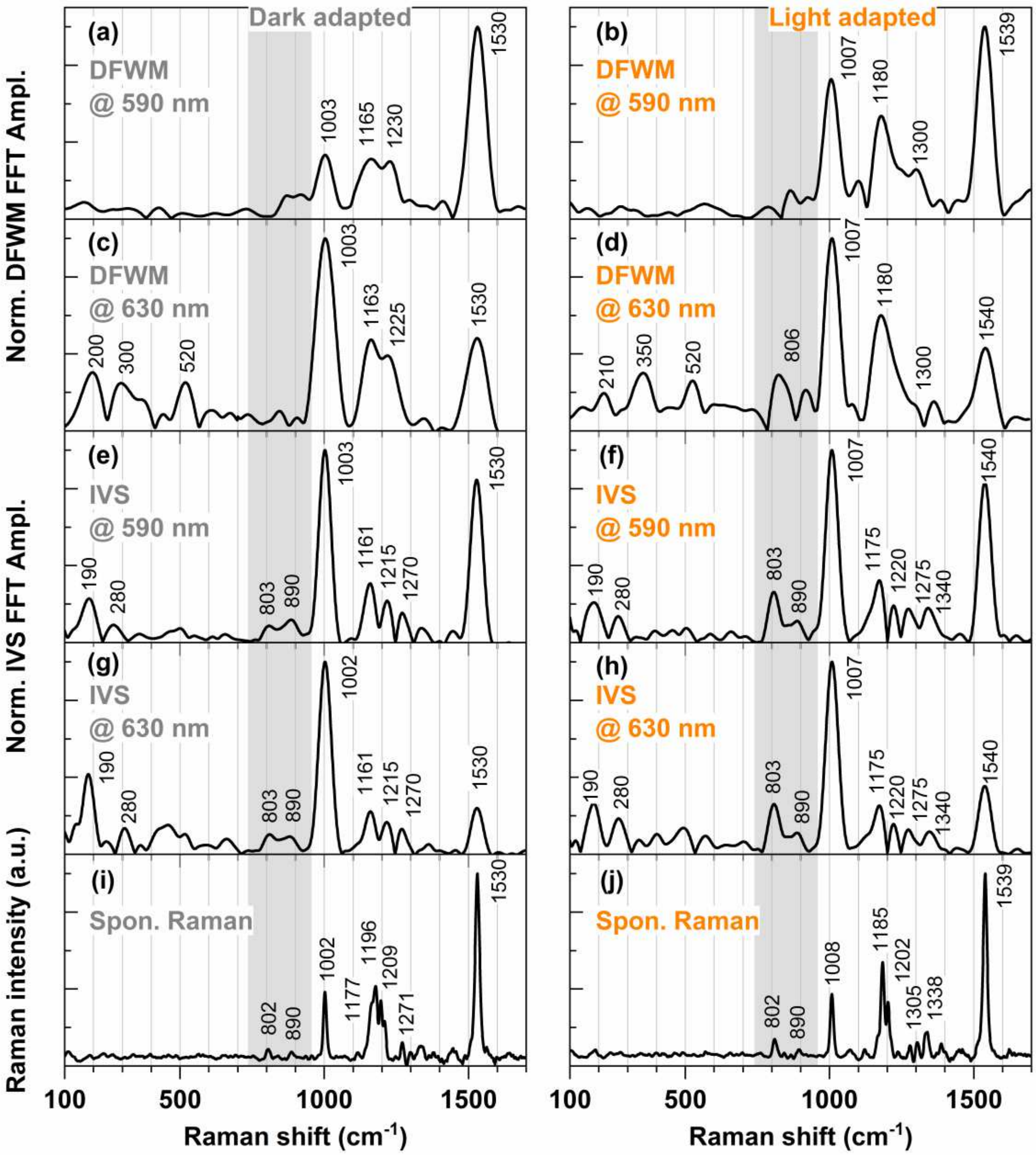

Figure 5.2: The FFT spectra obtained after subtraction of the non-oscillatory components from the transients of DFWM (a-d) and IVS (e-h) experiment probed at 590 nm (a, b, e, f) and 630 nm (c, d, g, h). The left and right column represent the FFT spectra of DA and LA ASR respectively. The spontaneous Raman spectra of DA and LA ASR have been shown on the bottom graphs i and j respectively. The grey shaded area (~750-950 cm^{-1}) represents the characteristic frequency region of the HOOP modes of RPSB.

The comparison between the FFT spectra under dark adapted (DA) and light adapted (LA) conditions shows mainly three characteristic features. Firstly, the modes which appear at 1003 and 1530 cm^{-1} in the DA DFWM FFT spectrum (Figure 5.2 (a) and (c)) shift to 1007 and 1539 cm^{-1} (Figure 5.2 (b) and (d)), respectively, for the LA ASR. Secondly, the DFWM FFT spectrum of DA

ASR shows two peaks around 1165 and 1230 cm^{-1}, while for the LA ASR they appear at 1180 and 1300 cm^{-1}. All these changes are also observed in IVS measurements (compare Figure 5.2 (e) and (g) to (f) and (h)). For instance, the modes around 1100-1400 cm^{-1} also show in IVS qualitatively similar contrasts between the DA and LA ASR as observed in DFWM measurement. Three peaks at 1161, 1215 and 1270 cm^{-1} for the DA ASR (Figure 5.2(e) and (g)) change to 1175, 1220, 1270 and 1340 cm^{-1} under the LA condition (Figure 5.2 (f) and (h)). Finally, the modes appearing in the region of 750-950 cm^{-1} (grey shaded area in Figure 5.2), in particular the mode at about 806 (DFWM)/ 803 cm^{-1} (IVS), shows relatively stronger amplitude for the LA ASR than the DA ASR. This is a very important result which will be discussed later.

The observed GS fingerprint vibrational modes of RPSB have been already well assigned in previous reports.[53, 84, 141, 143, 145-148] We hereby follow the same assignments of the main spectral peaks to specific vibrational motions (Table 5.1). For example, the mode around 1000-1010 cm^{-1} is assigned to CH_3 rock and that around 1530/1540 cm^{-1} is assigned to C=C stretching mode. The

Table 5.1: Comparison of the central frequencies (in cm^{-1}) of the spectral peaks obtained from non-resonant DFWM, IVS and spontaneous Raman measurements (shown in Figure 5.2). Assignment of the modes are done based on value reported on the literatures.[53, 84, 141, 143, 145-148]

Dark adapted (98% AT)			**Light adapted (64% 13C; 36% AT)**			**Assignment of the modes**
DFWM	**IVS**	**Spon. Raman**	**DFWM**	**IVS**	**Spon. Raman**	
200, 300, 520	190, 280	-	210, 350, 520	190, 280	-	Delocalized torsion[143, 147]
900	803, 890	802, 890	810, 900	803, 890	802, 890	Hydrogen out of plane wag[53, 84, 145]
1003	1003	1002	1007	1007	1008	CH_3 rock[53, 141, 145-146]
1165, 1230	1161, 1215, 1270	1177, 1196, 1209, 1271	1180, 1300	1185, 1202, 1305, 1338	1175, 1220, 1275, 1340	C-C stretch + C-C-H in plane rock[53, 141, 145-146]
1530	1530	1530	1530	1539	1539	C=C stretch[53, 141, 145-146]

multiple peaks in the region from 1100 to 1400 cm^{-1} are mostly known as the signature of the stretching vibration of different C-C bonds present in RPSB, often coupled with C-C-H in-plane-rock modes. In addition, the low frequency modes (190, 300 cm^{-1}) are usually assigned to the delocalized torsional modes, whereas the Raman activity in the region 750-950 cm^{-1} (grey shaded area in Figure 5.2) is well known for the hydrogen out-of-plane (HOOP) wags (Table 5.1). In addition, a non-resonant (λ_{exc}=785 nm) spontaneous Raman measurement (Figure 5.2 (i)-(j)) was performed to further corroborate the vibrational spectra obtained from the time resolved experiments (DFWM and IVS). While the non-resonant Raman results match very well most of the frequencies and respective shifts observed with DFWM/IVS (Figure 5.2(a)-(h)), there are three major contrasts: (i) Different frequencies for modes in the spectral region between 1100 and 1400 cm^{-1}, (ii) Complete absence of low frequency modes (<750 cm^{-1}) in the non-resonant Raman measurements (which were active in the DFWM/IVS measurements) and (iii) Different amplitude of the 803/805 cm^{-1} mode. (see section 3.3.2)

5.2 Separation of species specific contribution

While the spectral features observed for DA and LA ASR (Figure 5.2) already mirror the different isomer concentrations, in the following a quantitative extraction of the pure AT and 13C spectra will be performed. In section 3.3.3, it is shown how individual contribution of each species from a spectrum can be seprated, where more than one species contribute e.g. the FFT spectrum of LA ASR which contains the mixture of AT and 13C isomers. Following this approach, the pure spectrum of the ground state of the 13C isomer is obtained (Figure 5.3).

The same approach can also be applied to obtain the spectrum of the K-photoproduct of each isomer (K_{13C} and K_{AT}). In order to obtain the DFWM signals of these photoproducts, each isomer was directly excited by an actinic pulse spectrally resonant with the respective GS absorption (Figure 5.1). The DFWM spectrum was still spectrally resonant with the photo-induced absorption (PIA) band (see Figure 5.1) but delayed at T=100 ps after the AP. This particular delay was chosen as the formation of the vibrationally cold K-photoproduct is known to complete within 100 ps (see Figure 1.2).[45, 90] The pump-DFWM signal in this condition contains several contributions. The signal of DA ASR after 100 ps, for example, contains contributions of the AT GS and of K_{AT},

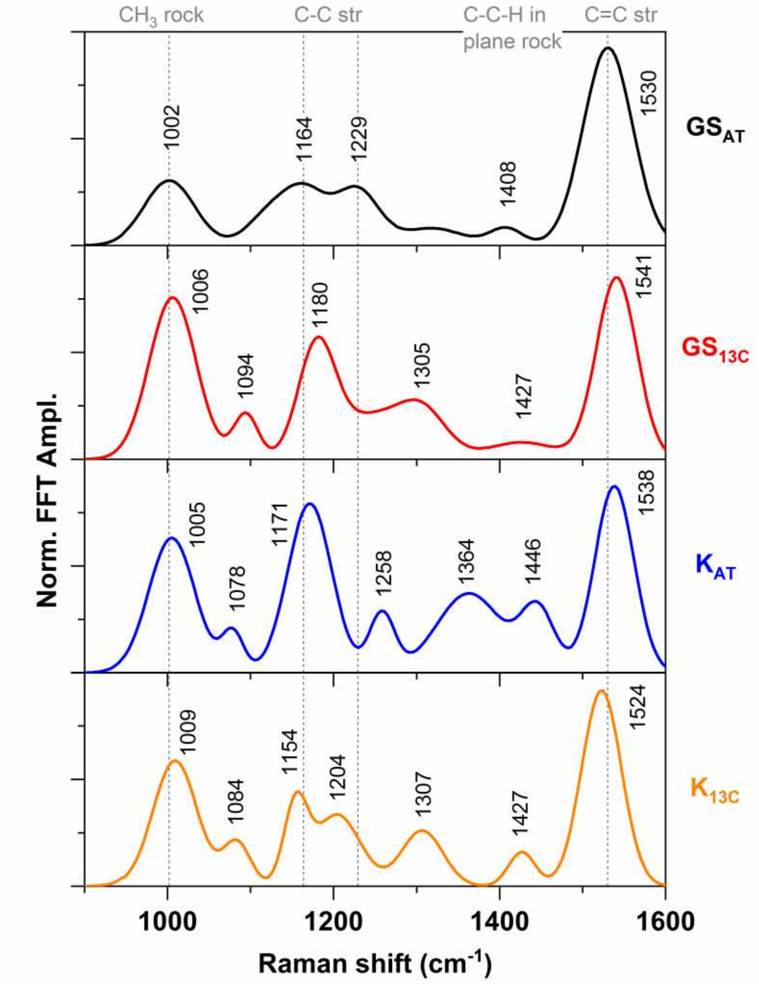

Figure 5.3: The separated pure spectra of AT GS, 13C GS, KAT and K13 are represented by black, red, blue and orange line, respectively. The black dotted lines represent the central frequencies obtained for AT GS.

which are reasonably easy to separate in case of pump-DFWM and less in pump-IVS due to noise (see section 3.3.2). The pump-DFWM signal of the LA ASR, however, is much more challenging: At 100 ps delay, it contains the signal of the GS of both isomers, as well as from both photoproducts. In order to extract the K_{13C}, the spectra of AT, K_{AT} and 13C must be used, which is inherently more susceptible to noise. With this information in mind, the pure spectra of four different stereo-isomers (GS_{AT}, GS_{13C}, K_{AT} and K_{13C}) appearing in the photo-cycle are depicted in Figure 5.3.

Several differences in spectral signatures of these four species can be observed. For example, the C=C stretching mode of 13C GS (1541 cm^{-1}) gets blue shifted compared to that of AT GS

(1530 cm^{-1}). Also, isomerization at C_{13}=C_{14} position causes the C=C stretching mode to shift in the higher frequency from AT GS (1530 cm^{-1}) to K_{AT} (1538 cm^{-1}), whereas it shifts to the lower frequency from 13C GS (1541 cm^{-1}) to its corresponding sub-ns photo-product K_{13C} (1524 cm^{-1}). Similar trend is also observed for the CH_3 rock mode of K_{AT} while for K_{13C}, it gets blue shifted compared to 13C GS. The frequencies and amplitudes of modes in the spectral region between 1100 and 1300 cm^{-1} are very different for each isomer. Finally, it is important to note that the spectral peaks appearing in the region 1300-1450 cm^{-1}, which have been assigned to C-C-H in-plane rock mode (Table 5.1), do not change from 13C GS (1305, 1427 cm^{-1}) to K_{13C} (1307, 1427 cm^{-1}), whereas a significant change is observed from AT GS to K_{AT}. A single weak peak at 1408 cm^{-1} appears for AT GS, while at least two strong peaks appear for K_{AT} (1364, 1446 cm^{-1}) in this region.

5.3 Pump-DFWM experiments in sub-ps time scale

In order to follow the isomerization reaction of both 13C and AT in the excited state, pump-DFWM measurements were performed by varying the actinic pulse delay (T) up to about 1 ps (Figure 5.4). Fourier-transformed spectra for the DA and LA are displayed in Figure 5.4 (a) and (b), respectively. In both samples, two common changes can be observed after the arrival of the actinic pulse (T>0): (i) amplification of the high frequency modes (>1000 cm^{-1}) and (ii) appearance of the strong low frequency modes (100-400 cm^{-1}), in particular for LA ASR (Figure 5.4 (a)), which were very weak in the GS (Figure 5.2). Moreover, a closer look on the high frequency (>1000 cm^{-1}) modes (Figure 5.4(c)) shows a significant spectral shift with the actinic pulse delay. The major spectral shifts of DA and LA ASR happen within 800 and 200 fs, respectively, which matches the

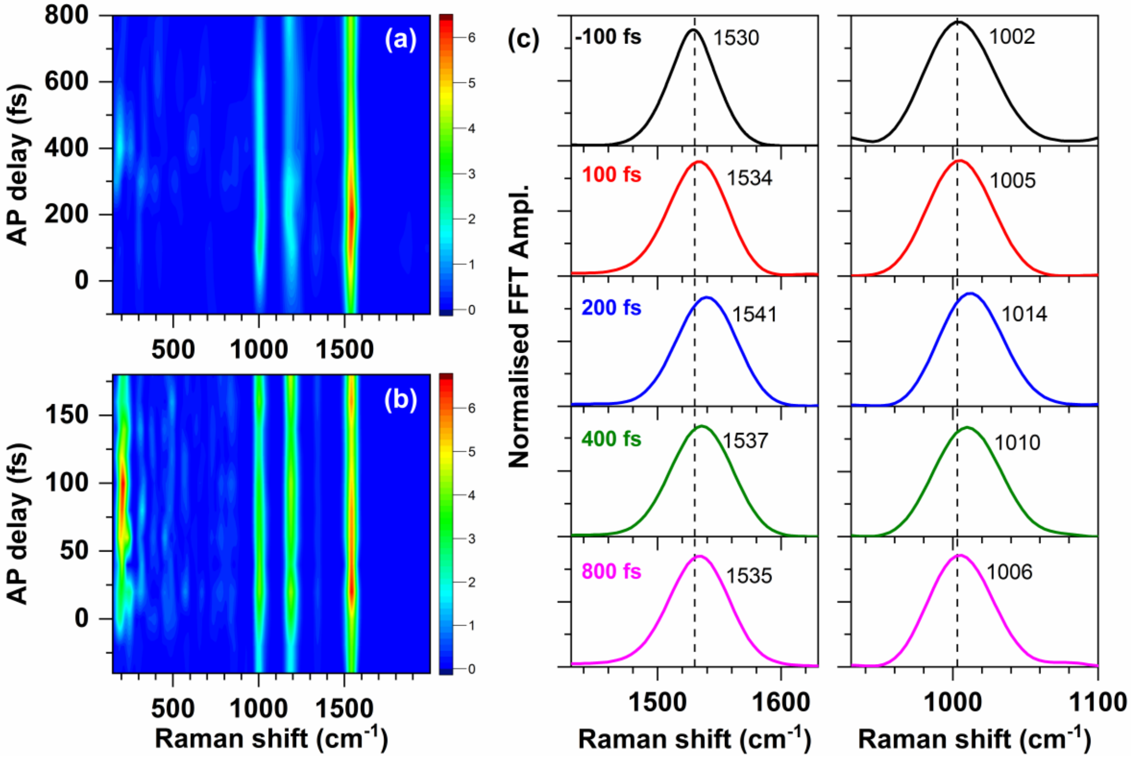

Figure 5.4: The evolution of pump-DFWM FFT spectra probed at 590 nm for (a) DA and (b) LA ASR with the actinic pulse delay. (c) The frequency shift of C=C stretch (left) and CH_3 rocking (right) mode for DA ASR with different actinic pulse delays. The black dotted lines represent the central frequencies obtained for AT GS (Figure 5.3).

excited state lifetime of the AT (770 fs) and 13C (170 fs) isomers.[45, 90] The frequency evolution for each of the characteristic vibrational modes are described in the following.

5.3.1 C=C stretching and CH_3 rock modes

Figure 5.4(c) depicts the evolution of C=C stretch and CH_3 rock modes for DA ASR. Here, a negative time delay means the actinic pulse comes after DFWM interaction, which should basically give the GS vibrational spectra. Hence, the central frequencies of C=C stretch and CH_3 rock modes at T=-100 fs, which appear at 1530 and 1002 cm^{-1}, match the GS frequencies obtained by non-resonant DFWM experiments (Figure 5.2). At initial positive T-delays (until 200 fs), each of these modes shows a rapid blue shift and subsequently a slower red shift (see e.g. DA in Figure 5.4(c)). Although the FFT spectra at T>0 contains the major contribution of the transient species being resonantly probed at the corresponding time, a minor contribution of GS coherence, due to the non-resonant Raman interaction, still contaminates the signal. As a consequence, pump-

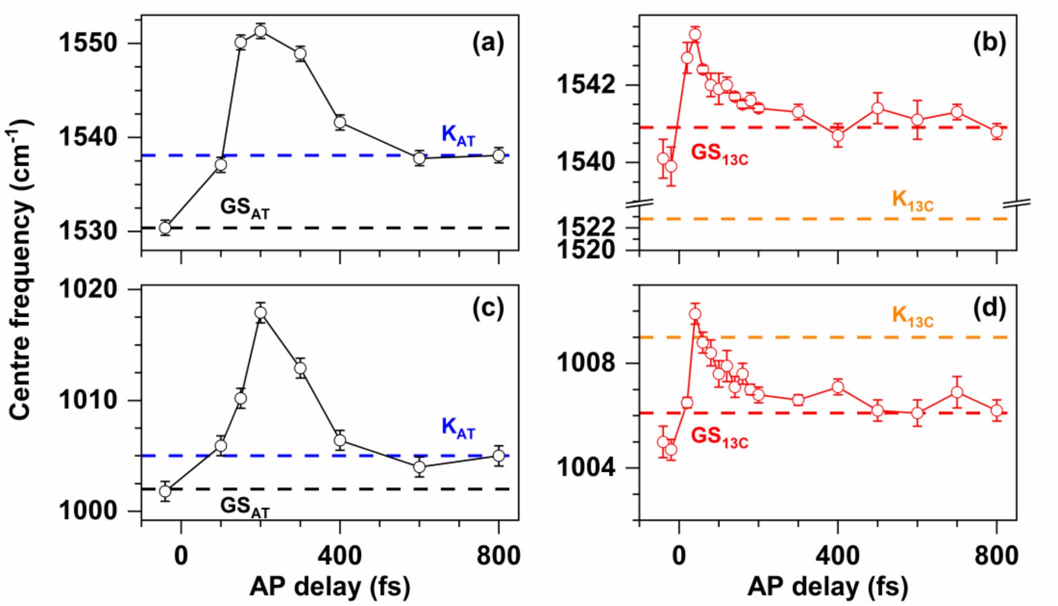

Figure 5.5: The sub-ps evolution of C=C stretching (a, b) and CH_3 rock modes (c, d) obtained for the pure excited state of AT isomer (a, c) and LA (b, d) form ASR. The central frequencies of pure GS (AT and 13C) and K-photo intermediates (K_{AT} and K_{13C}) are shown by black, red, blue and orange dotted lines respectively in each graph. Probe detection wavelength was 590 nm in each case.

DFWM FFT spectra at any positive actinic pulse delay (T) is not the pure spectra of the transient species formed within the corresponding time (T) after the initiation of the reaction by AP. Since the pure GS spectra of AT isomer is already known (Figure 5.3), it is possible to extract the pure spectra of the transient species present at different actinic pulse delays by the aforementioned (section 3.3.3) constrained multi-Gaussian fitting.

By applying this method, the frequencies of C=C stretch and CH_3 rock modes for AT are obtained as shown in Figure 5.5(a) and (c), respectively. AT shows a clear strong blue shift of 21 and 18 cm^{-1} for the C=C stretch and CH_3 rock modes, respectively, at T=200 fs compared to that of GS species (T<0). At longer delays (T>200 fs), it undergoes a red shift to 1538 and 1005 cm^{-1}. These latter two frequencies are the central frequencies of the C=C stretch and CH_3 rocking modes, respectively, of previously extracted pure K_{AT} (Figure 5.3). The separation of all contributions to the transient LA ASR signal is more challenging than for DA ASR. Here, two ground state species are excited (AT and 13C), followed by two excited states and two photoproducts, which leads to much larger frequency uncertainties and ambiguous results. Therefore, the frequency shifts of the C=C stretch and CH_3 rock modes for the LA ASR are shown without extraction (Figure 5.5(b) and (d), respectively). Nevertheless, a similar trend is observed as for AT, i.e. an initial blue shift takes place followed by a red shift. However, the blue shift is much smaller and the whole dynamics is much faster in the LA than for AT (compare e.g. Figure 5.5(a) to (b)). The maximum of the blue shift appears at much earlier actinic pulse delay (about T=40 fs) compared to AT form (about T=200 fs).

5.3.2 Fingerprint (1100-1400 cm^{-1}) region

As observed for the GS spectra (Figure 5.2), the fingerprint region around 1100-1400 cm^{-1} (Figure 5.6) shows a congested spectrum after the actinic excitation, particularly for AT ASR. The double peak feature (1165 and 1230 cm^{-1}) before time zero merges to single major peak (1193 cm^{-1}) along with a minor peak (1330 cm^{-1}) at T=100 fs for AT ASR. Afterwards, the major peak shows

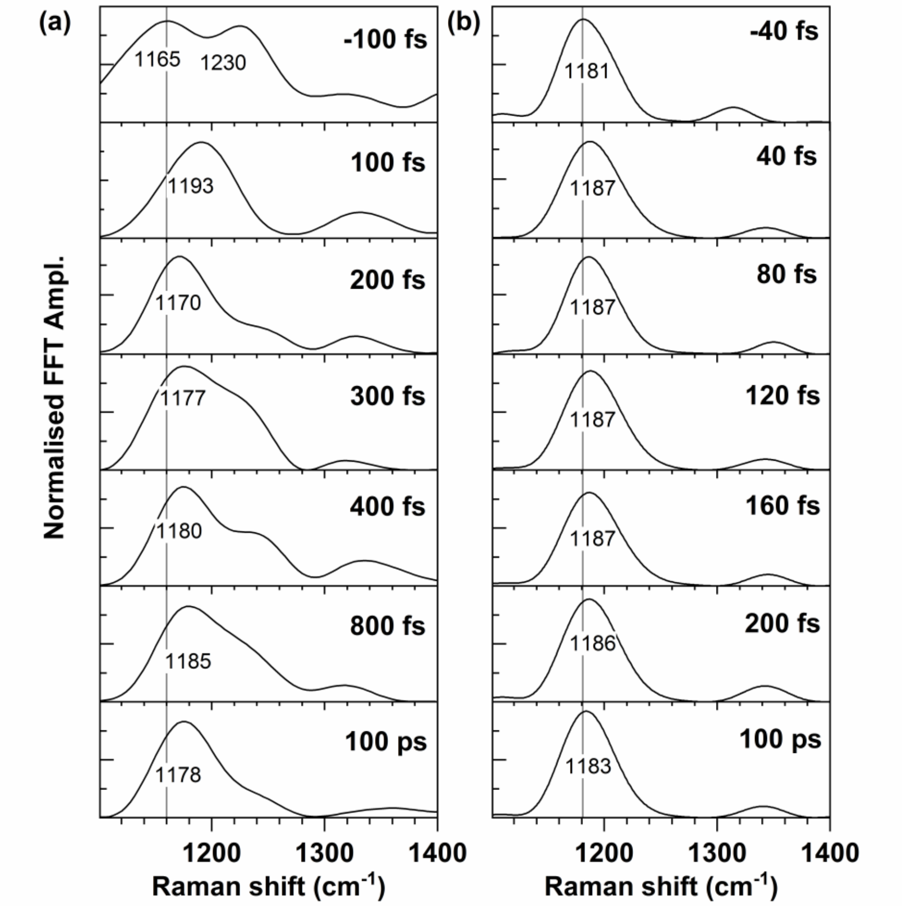

Figure 5.6: The evolution of finger print (1100-1400 cm^{-1}) modes in the pump-DFWM FFT spectra for (a) AT and (b) LA ASR at different actinic pulse delay (T) probed at 590 nm. The vertical lines in (a) and (b) represent the corresponding central frequencies of AT and 13C GS, respectively.

a red shift till 200 fs which is followed by, a slow monotonous blue shift until the formation (200 to 800 fs) of the hot-intermediate, commonly known as J-species in literature. Subsequently, it undergoes a small red shift during vibrational relaxation on a much longer time scale (1 to 100 ps) to form the cold photo-product (K_{AT}). This contrasts to the signal of LA ASR where the major peak at ~1181 cm^{-1} undergoes a blue shift initially (T=40 fs) to 1187 cm^{-1} and does not shift afterwards within the excited state lifetime (<120 fs) of the 13C isomer. It only shows a small (1187 to 1183 cm^{-1}) red shift during the photo-product vibrational relaxation (~1 ps to 100 ps), similar to the AT-isomer.

5.3.3 Low frequency (<400 cm^{-1}) torsion and HOOP modes

An activation of the low frequency modes below 400 cm^{-1} (Figure 5.7(a) and (b)) is observed in dependence of the actinic pulse delay, which was absent or very weak in GS (Figure 5.2). This contrasting activity of low frequency (<400 cm^{-1}) modes is further evidenced in Figure 5.7 at several actinic pulse T-delays. A significant relative amplification of the low frequency modes (~190, ~300 cm^{-1}), compared to the high frequency (>1000 cm^{-1}) modes, is observed at T>0 for

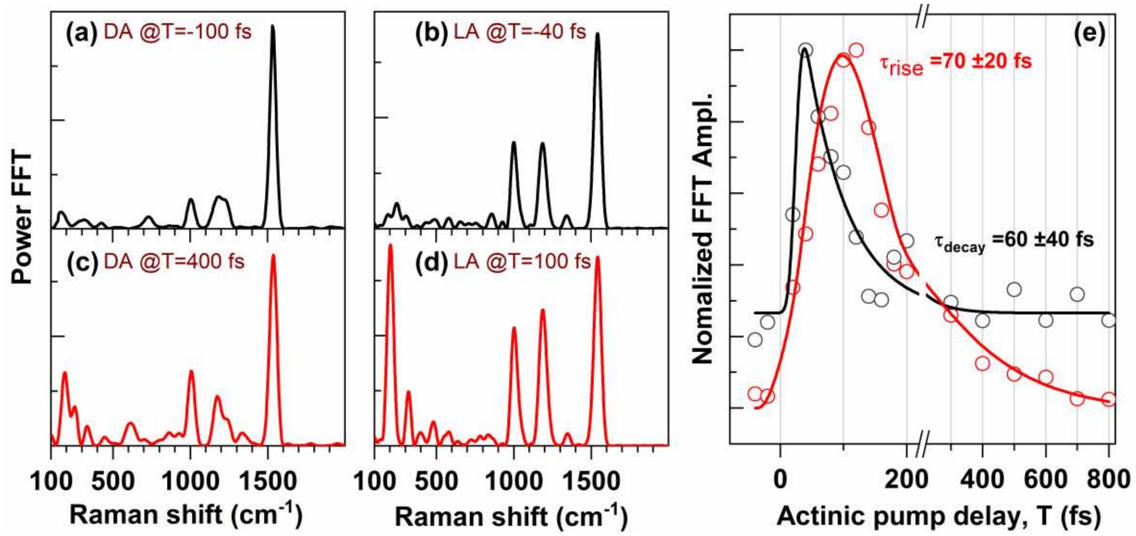

Figure 5.7: The relative amplification of low frequency modes probed at 590 nm (a, b) before (black, T<0) and (c, d) after (red, T>0) the arrival of actinic pulse for DA (a, c) and LA (b, d) ASR. (e) Comparison of the evolution of the normalized FFT amplitude for C=C stretching (black) and low frequency (~190 cm^{-1}) (blue) modes for LA ASR. The former trace was fitted with a mono-exponential decay model while the latter was fitted with bi-exponential model including a decay and rise components. Each of them was convoluted with a Gaussian instrumental response function (IRF). Initial 200 fs of the time axis has been expanded.

DA and LA ASR. Here it is important to note that the low frequency activity of LA ASR is much stronger than that of DA ASR.

The evolution of the amplitude of the low frequency modes is different from other modes shown for LA ASR in Figure 5.7(e). The high frequency mode e.g. C=C stretch has non-zero amplitude before time zero; increases almost instantaneously after the arrival of actinic pulse (T<20 fs). It decays afterwards and shows a constant amplitude even after 600 fs which well beyond the excited state lifetime. In contrast, the low frequency (e.g. 190 cm^{-1}) mode shows almost no amplitude at T<0 as well T> 600 fs. Afterwards, a delayed (~100 fs) rise can be clearly detected. The FFT amplitude of the low frequency (190 cm^{-1}) modes takes about 100 fs to reach the maxima whereas that of C=C stretching mode reaches the maxima within the experimental time resolution after the actinic excitation (T=20 fs). More interestingly, the exponential rise time (70 ±20 fs) of low frequency (190 cm^{-1}) modes matches the exponential decay time (60 ±40 fs) of C=C stretch mode (Figure 5.7(e)). In contrast to this significant evolution in the low frequency (<400 cm^{-1}) region, no significant evolution of HOOP modes (800-1000 cm^{-1}) is observed in our measurements. This will be further discussed and investigated in section 5.4.3.

5.4 Discussion

5.4.1 Ground state Raman activity

Mode Assignment: A strong Raman activity of the vibrational modes mainly in the high frequency (>1000 cm^{-1}) region of the spectra has been observed in non-resonant experiments (Figure 5.2). The convolution of DFWM/IVS spectrum with the GS absorption spectrum (Figure 5.1), gives a FWHM of about 500 cm^{-1} and, therefore, there is a negligible induction probability of a vibrational coherence above 500 cm^{-1} in the ES potential surface. Hence, all modes with frequencies well over 500 cm^{-1} in these non-resonant measurements, including HOOP, CH_3-rock, C-C and C=C modes, are assigned to GS manifold. This is further supported by the spontaneous Raman spectra (Figure 5.2(i) and (j)), which show a good correlation with the FFT spectra obtained from time resolved experiments for frequencies well over 500 cm^{-1}. However, the weak but detectable Raman activity observed in the low frequency region (200 and 300 cm^{-1}) in both DFWM and IVS signal,

Table 5.2: Comparison of the selected fingerprint vibrational modes for all-trans and cis isomers found for ASR in this report and those reported for Retinal protonated schiff base (RPSB) in solution and different proteins: bacteriorhodopsin, visual rhodopsin and chanello-rhodopsin.

Sample	CH_3 rock [cm^{-1}]	C-C stretch + C-C-H in-plane rock [cm^{-1}]	C=C stretch [cm^{-1}]
AT-RPSB in methanol[106]	1010	1160, 1205	1565
Bacteriorhodopsin (AT)[105]	1008	1165, 1210	1530
Visual-rhodopsin (AT)[70]	-	1167, 1322	1541
Visual-Rhodopsin (11-Cis)[70]	-	1173, 1275, 1313, 1363	1550
Chanello Rhodopsin (AT)[149]	1011	1161, 1208, 1281	1531
Chanello Rhodopsin (13-Cis)[149]	1017	1157, 1196, 1301, 1369	1545
ASR (AT) [This thesis]	1002	1164, 1229	1530
ASR (13C) [This theis]	1006	1094, 1180, 1305	1541

does not appear in any spontaneous Raman spectra. If this low frequency activity originates from GS, it should definitely be visible in the spontaneous Raman measurements. Therefore, we assign all low frequency (<400 cm^{-1}) activity detected with DFWM/IVS to the excited state manifold. A detailed discussion about the origin and activation mechanism of these mode will be done in section 5.4.3.

AT vs Cis RPSB: The extraction of the pure GS spectra of AT and 13C isomer (Figure 5.3) enables us to do a quantitative comparison. The central frequencies of C=C stretch and CH_3 rock modes are shifted AT to 13C ASR. This is in good agreement with reported values for ASR.[45] A similar increase of high frequency modes from all-trans to cis isomer has also been reported recently for chanello-rhodopsin[149] and visual Rhodopsin[70](see Table 5.2), which further corroborates the separation of the pure spectra of ASR. Furthermore, the C-C stretch region shows multiple distinguishable peaks between AT and 13C ASR (Table 5.1). Two peaks around 1165 and 1230 cm^{-1}, observed for AT ASR (Figure 5.3), are quite common for retinal chromophores in AT conformation in other proteins (Table 5.2). On the other hand, the appearance of a distinguishable mode above 1300 cm^{-1} for 13C ASR is a general marker of cis form (Table 5.2). In addition, the

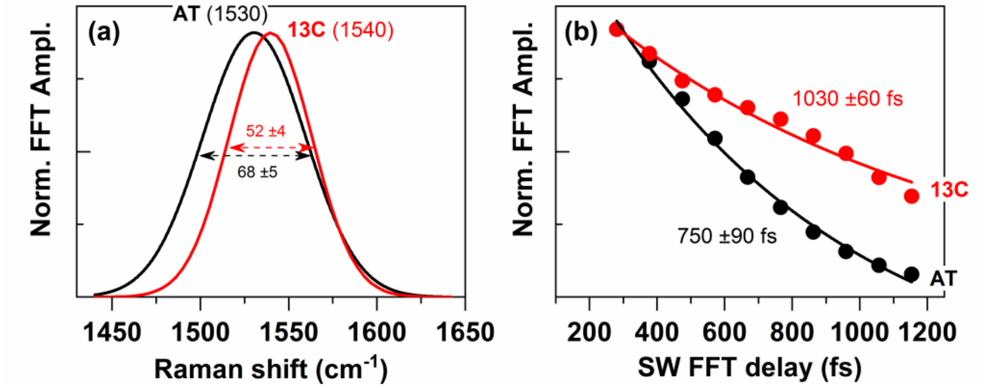

Figure 5.8: (a) Normalized C=C stretching modes of AT (black) and 13C (red) isomer. Where the former has FWHM of 68±5 cm^{-1} the latter has FWHM of 52±5 cm^{-1}. (b) The dephasing time of C=C stretching modes of AT (black) and 13C (red) ground state isomers, obtained by a employing a sliding window FFT algorithm with a Gaussian window with a width of 600 fs and subsequent exponential fit (black and red solid lines).

C-C stretch mode which appears at 1180 cm^{-1} in case of 13C ASR, has been attributed as an indicator for the formation of 13C-isomer of bacteriorhodopsin (BR).[150]

Dephasing of C=C stretch mode: A comparison of pure AT and 13C spectra shows a striking difference in width of the spectra, particularly for the C=C stretching mode (Figure 5.8(a)).[87] The full width at half maximum (FWHM) of this mode for 13C obtained as 52 ±4 cm^{-1} whereas that for AT is 68 ±5 cm^{-1}. This hints at the difference in the dephasing rate of GS vibrational wave packet. A sliding window FFT (Fig. 12) with a Gaussian window of 600 fs for each of DA (~AT), LA and 13C (retrieved from LA) DFWM transients shows indeed the dephasing is faster (750 ±90 fs) for AT compared to 13C (1030 ±60 fs) (Figure 5.8(b)). Hence, the faster dephasing rate hints at stronger coupling of the AT GS with the surrounding bath compared to 13C GS.

HOOP mode activity: The activity of HOOP modes (800-1000 cm^{-1}) in GS (grey shaded region in Figure 5.2) has been interpreted as an indirect indicator of a distorted non-planar structure of RPSB.[142-143] The relative amplitude of the HOOP modes, particularly at 805 cm^{-1}, is higher in LA (major component is 13C) ASR compared to DA (98% AT) ASR. This observation is consistent in each (DA vs LA) of the spectra measured by three different spectroscopic techniques (DFWM, IVS and spontaneous Raman). All these together, hints at the presence of a non-planar structure for the 13C isomer, although it is much less distorted than the 11-cis isomer in visual Rhodopsin.[84, 141-143] A detailed assignment of H-wag modes is, however, necessary in order to specify the region of

Table 5.3: Parameters obtained by performing a constant-pH molecular dynamics simulations (CpHMD)[153] of ASR, with either AT or 13C retinal for 30 ns. This theoretical calculation was done by Dr. Elisa Pieri and Prof. Nicolas Ferré in Aix-Marseille University. Briefly, the ASR models have been built using the 1XIO structure available in the Protein Data Bank. Only the protein structure, the retinal chromophore and the crystallographic water molecules have been kept. The 58-66 missing loop, as well as missing hydrogen atoms, have been added before to embed the protein inside a membrane bilayer model, essentially made of 1-palmitoyl-2-oleoyl-sn-glycero-3-phosphoethanolamine molecules, water molecules and $Na^+ + Cl^-$ counter ions, using the CHARMM-GUI web server.[154] After the release of bad contacts (energy minimization, heating at 300K, equilibration), the full system has been studied at different pH values with CpHMD using the ff14sb Amber force field for the protein,[155] TIP3P for the water molecules,[156] lipid17[157] for the membrane and parameters for retinal derived by Hayashi *et al.*[158] Only the pH=7 results are reported below.

	AT isomer		**13C isomer**	
Parameters	Mean value	Standard deviation	Mean value	Standard deviation
$C_{13}=C_{14}$	1.413 Å	0.030 Å	1.413 Å	0.029 Å
C_{12}-C_{13}-C_{14}-C_{15}	191.6°	7.3°	11.7°	7.2°
C_{11}-C_{12}-C_{13}-C_{14}	176.3°	6.9°	176.3°	6.6°
C_{13}-C_{14}-C_{15}-N	177.1°	6.9°	189.5°	6.5°

distortion in the long Retinal chain. The complete assignment of H-wag modes for ASR has not been reported yet but it is well known for BR from the resonant Raman study by Smith *et al.*[146] In that report, a mode at 800 cm^{-1} was assigned to C_{14}-H out-of-plane wag and showed strong amplitude for 13C isomer whereas it almost disappears for AT isomer, similar to ASR in our study. Later, solid state NMR data[151-152] indicated a difference in the structural rigidity along the $C_{13}=C_{14}$-C_{15} moiety between AT and 13C isomers inside the Retinal pocket of BR. Following the same line, our observation can be interpreted as both isomers are pre-twisted around or close to $C_{13}=C_{14}$ bond of Retinal chromophore but 13C isomer is well more distorted than AT.

The exact position of this distortion and the differences between the two isomers can be further numerically investigated by applying a classical (harmonic) atomistic force field and performing molecular dynamics simulations of ASR embedded in a membrane model (Table 5.3). The geometry of AT and 13C GS inside the Retinal pocket shows that both isomers are equally distorted around the $C_{13}=C_{14}$ bond, i.e. the dihedral angle of C_{12}-C_{13}-C_{14}-C_{15} is found to be +191.6° and 11.7° (Table 5.3) for AT and 13C isomer, respectively. This is in well agreement with the value (~13°) previously reported by QM/MM geometry optimization calculations.[91] These new calculations, however, shows that the isomers significantly differ around the neighboring C_{14}-C_{15}

bond (dihedral C_{13}-C_{14}-C_{15}-N): While AT is nearly planar (177.1°) around the C_{14}-C_{15} bond, the 13C is almost 10° twisted (189.5°). This relatively larger pre-twist around C_{14}-C_{15} bond for 13C isomer corroborates very well the experimental observation of higher amplitude of C_{14}-H wag as discussed above in the previous paragraph.

Photoproduct ground state: Finally, a brief comparison of vibrational signatures of GS isomer with its corresponding K-photoproducts (Figure 5.3) helps to further rationalize the frequency shifts in terms of conformational differences. The conformational changes alter the delocalization of δ and π-electron density for the macro-molecule like RPSB, which explains the frequency shift of CH_3 rock, C-C and C=C stretch and C-C-H in-plane rock modes. The changes in the frequency and amplitude of C-C-H in-plane rock (1300-1400 cm^{-1}) modes (Figure 5.3) are important as these are reported to be affected by the torsion around the active C=C bond.[61] Although the frequency of this mode changes from AT GS (1408 cm^{-1}) to K_{AT} (1364, 1446 cm^{-1}), it remains almost the same for 13C GS (1305, 1427 cm^{-1}) and for K_{13C} (1307, 1427 cm^{-1}), indicating a very similar strain around the C_{13}=C_{14} bond for the latter two isomers. These results also corroborate FTIR studies which illustrated that isomerization causes larger rotation of Schiff base moiety for AT isomer compared to 13C isomer.[145]

5.4.2 Excited state evolution of high frequency modes (>1000 cm^{-1})

The pump-DFWM measurements captured the sub-ps frequency shifts of high frequency modes. In general, the C=C stretch and CH_3 rock modes showed a blue shift and subsequent red shift for both AT and LA (major 13C) ASR. Since the DFWM spectra, used for this measurement, covers the region (580-720 nm) where both excited state absorption and stimulated emission of ASR overlaps,[45, 90] there are two possible origins for the observed frequency shifts: (i) the excited state evolution of the nuclear wave packet or (ii) the vibrational relaxation of the GS wave packet, generated by stimulated emission pumping (SEP) process,[18, 63, 79] in an anharmonic potential energy surface. For the latter, one would expect a red shift just after the excitation.[63] This is because the GS wave packet, generated via SEP, in a higher lying vibrational states is lower in frequency than a relaxed GS wave packet generated via non-resonant ISRS in the lower lying vibrational states. On the contrary, we observed a blue shift compared to the GS. This excludes this possibility and hence, the frequency shift is interpreted as coming mostly due to the excited state wave packet motion. In addition, the time scale of the frequency shifts is significantly different for AT and 13C

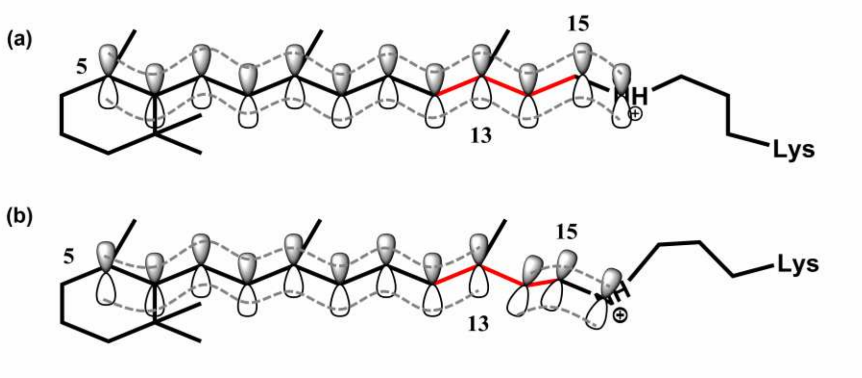

Figure 5.9: The reduction of the effective π-conjugation length from (a) Franck-Condon excited state to (b) twisted transition state (far Franck-Condon region). In (a), there is an extended π-conjugation from C_5-atom to N-atom of the Schiff base which is reduced in (b).

isomers. It matches very well the excited state lifetime of each isomer, which further indicates that the observed frequency shifts originate due to the transient evolution of the ES species from the Franck-Condon region to the GS through the conical intersection.

Sub-ps transient frequency shifts in the fingerprint region have been frequently interpreted as the conformational changes associated with the isomerization process.[61, 159] Here, the blue shift of C=C stretch (Figure 5.5) is interpreted as the reduction in conjugation length due to the rotation around the C_{13}=C_{14} bond during the isomerization. After the excitation by the actinic pulse, the RPSB is promoted to the Franck-Condon point of the excited state where it is still in the same geometry as it is in ground state (Figure 5.9(a)). In this geometry, an extended π-conjugation is present along the Retinal chain by the p_z orbitals from C5 up to protonated Schiff base N-atom. As the isomerization reaction progresses, the RPSB starts to adopt a more non-planar twisted structure (Figure 5.9(b)) towards the photoproduct geometry. During this evolution, the C_{14}-C_{15}-N π-conjugated moiety becomes almost perpendicular to the remaining π-conjugated system (C_5 to C_{13}) at the 90° twisted form (AT*) and the conjugation between two moieties, mentioned before, gets completely disrupted. Hence, the effective conjugation length gets reduced during evolution from the Franck-Condon state towards the 90° twisted form. It is well known for linear conjugated polyenes that the reduction of effective conjugation length causes a frequency blue shift of the C=C stretch mode.[160-161] Thus, decrease in the effective conjugation length explains the blue shift of C=C stretching mode observed here for Retinal in ASR. The blue shift of CH_3 rock mode can also be interpreted in a similar way. The disruption of the C_{13}=C_{14} bond during isomerization reduces the partial positive charge over the C_{13} atom induced by the positively charged Schiff base N-atom. The partial positive charge over C_{13} tends to pull the electron density from the CH_3 moiety (bonded to C_{13}) towards it but the lack of inductive effect in the twisted state pushes the electron density towards the CH_3 moiety. This possibly causes the blue shift of the rock mode of CH_3. This also corroborates the picture of change in electron density during the isomerization of bR, recently captured by the transient femtosecond X-ray spectroscopy.[31] Thus, following our argument, the slower frequency shift observed for AT isomer compared to 13C isomer (~LA) (Figure 5.5) can be interpreted as follows: It takes longer time for the AT isomer to rotate around the C_{13}=C_{14} bond to form the 90° twisted state compared to 13C. This corroborates as well QM/MM calculations[91] which predicted a barrier in the excited trajectory of AT and, therefore, a slower formation of the corresponding twisted state.

The frequency shift of the fingerprint modes in the region from 1100-1400 cm^{-1} are relatively more complicated than the one observed for the C=C stretching mode. This is because different C-C stretching modes (C_8-C_9, C_{10}-C_{11}, C_{12}-C_{13} etc.) of Retinal exhibit distinct closely spaced peaks which overlap in that region. In addition, C-C-H in-plane-rock modes are also sometimes coupled with the C-C stretch which makes the spectral evolution of this finger print modes even more challenging to rationalize. However, the most intense peak below 1200 cm^{-1}, which is known to be mostly uncoupled from C-C-H rock modes, follows a trend which can also be accounted for the change in the effective π-conjugation length. It has been also observed for linear conjugated polyenes[160] that the small reduction in effective conjugation length causes a blue shift of the mode below 1200 cm^{-1} but further reduction of effective conjugation length eventually results in red shift. This matches very well the frequency shift of AT ASR (Figure 5.6), where it undergoes an initial blue shift until 100 fs and subsequently red shifts until 200 fs. This is the delay which has been interpreted above as the time to reach the 90° twisted state for AT ASR. Afterwards, the effective conjugation length is expected to increase again due to the slow formation of relatively planar K_{AT}. Thus, it causes a blue shift of the finger print mode. This effect is much weaker for 13C (~LA) isomer, which results in no observable shift. This once again hints at a smaller rotation around C_{13}=C_{14} in 13C isomer compared to AT isomer in ASR.

5.4.3 Excited state evolution of low frequency (<400 cm^{-1}) and HOOP modes

A central result of pump-DFWM measurements was the observation regarding strong activity of the low frequency modes around 190 and 300 cm^{-1} at positive actinic pulse delay which are absent in the GS (T<0). Very similar low frequency peaks (160, 210 and 300 cm^{-1}) have also been observed previously for ASR in the transient absorption experiments[98] by probing in the near infrared region (950-1450 nm) which is far away from the ground state absorption and only covered by the stimulated emission. Furthermore, a few strong Raman modes below 400 cm^{-1} have been observed in the excited state of RPSB in solution by Kraack *et al.*[106] and also observed more recently for Rhodopsin[67] and chanello-Rhodopsin[149] by Schnedermann *et al.* Moreover, most important, the low frequency modes (e.g. ~190 cm^{-1}) in the pump-DFWM transients show faster dephasing than high frequency modes (e.g. C=C stretch) (Figure 5.10). All these observations together clearly suggest that the low frequency activities are originated from the ES manifold.

Another central result is the lack of HOOP activity in the excited state in our pump-DFWM (and pump-IVS) measurements which is surprising. There are two plausible explanations for this observation. The surrounding protein environment in ASR, which is different compared to Rhodopsin and bR, where the HOOP activity is stronger,[62, 67] can significantly reduce the Raman transition probability of a specific mode by modifying the Retinal pocket. Secondly, the activity of

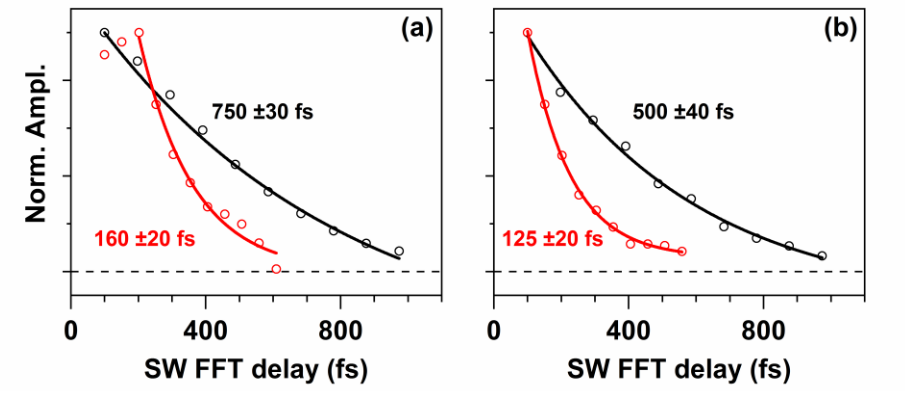

Figure 5.10: The dephasing of C=C stretch (black) and low frequency (190 cm^{-1}) mode (red) for (a) DA and (b) LA ASR, obtained by applying sliding window FFT on the pump-DFWM transient at T=100 fs. An FFT window of 600 fs was used in both cases avoiding initial 100 fs. In both cases low frequency modes dephase 4-5 folds faster than the high frequency C=C stretching mode. However, initial rise of low frequency amplitude in DA ASR showed delayed activation of this mode as illustrated in Figure 5.7 for LA ASR. However, it does not appear in (b) as the sliding window is applied after it finishes the rise (<80 fs).

the HOOP mode of bR has been observed to be strongly dependent on the center wavelength of DFWM spectra, used to create the vibrational coherence.[105] The Raman activity of this mode was found to be mainly enhanced for blue detuned excitation. In contrast, DFWM spectra in our study, were red detuned compared to the ground state absorption (Figure 5.1).

To clarify the lack of HOOP activity as well as to find out the activation mechanism of the low frequency (<400 cm^{-1}) excited state modes, we carried out two additional set of DFWM measurements with two different excitation spectra (Figure 5.11). Spectrum **1** is the same as used before (Figure 5.1) which is almost non-resonant to GS absorption and hence, only capable of exciting GS modes and also possibly the ES modes below 500 cm^{-1} due to small overlap with GS. Spectrum **2**, however, being completely resonant to the GS absorption, can directly excite all GS as well as ES vibrational modes. Two major changes (Figure 5.11) were observed for both DA and LA ASR by tuning the DFWM spectrum, namely (i) amplification of low-frequency and HOOP modes and the (ii) frequency-shift of high-frequency modes.

Relative amplification of low frequency (<400 cm^{-1}) and HOOP modes: The FFT spectra for non-resonant spectrum (Figure 5.11(a)), detected at 590 and 630 nm, show the activity mostly above 1000 cm^{-1} along with a few weak low frequency modes (~190, 300 and 510 cm^{-1}), as observed before (Figure 5.2). In contrast, a strong relative amplification of the FFT amplitude of low frequency modes (<400 cm^{-1}) with respect to high frequency modes (>1000 cm^{-1}), was observed for the FFT spectra in the resonant DFWM experiment (Figure 5.11(b)) compared to the non-resonant DFWM measurement (Figure 5.11(a)). On the one hand, these low frequency (<400 cm^{-1}) modes have been observed to be completely absent in the non-resonant steady state Raman spectrum (Figure 5.2(i)-(j)) and attributed to ES. The weak activity of these modes in the non-resonant DFWM FFT spectrum would mean these are directly activated in the Franck-Condon region of ES surface since there is small spectral overlap of DFWM spectra with the GS absorption. On the other hand, the same set of low frequency (<400 cm^{-1}) modes is strongly enhanced in resonant DFWM measurements, when compared to any other vibrational mode, what suggest that these modes cannot be Franck-Condon active otherwise it should also appear strongly already in the non-resonant DFWM FFT spectra, as other high-frequency modes. These observations can be

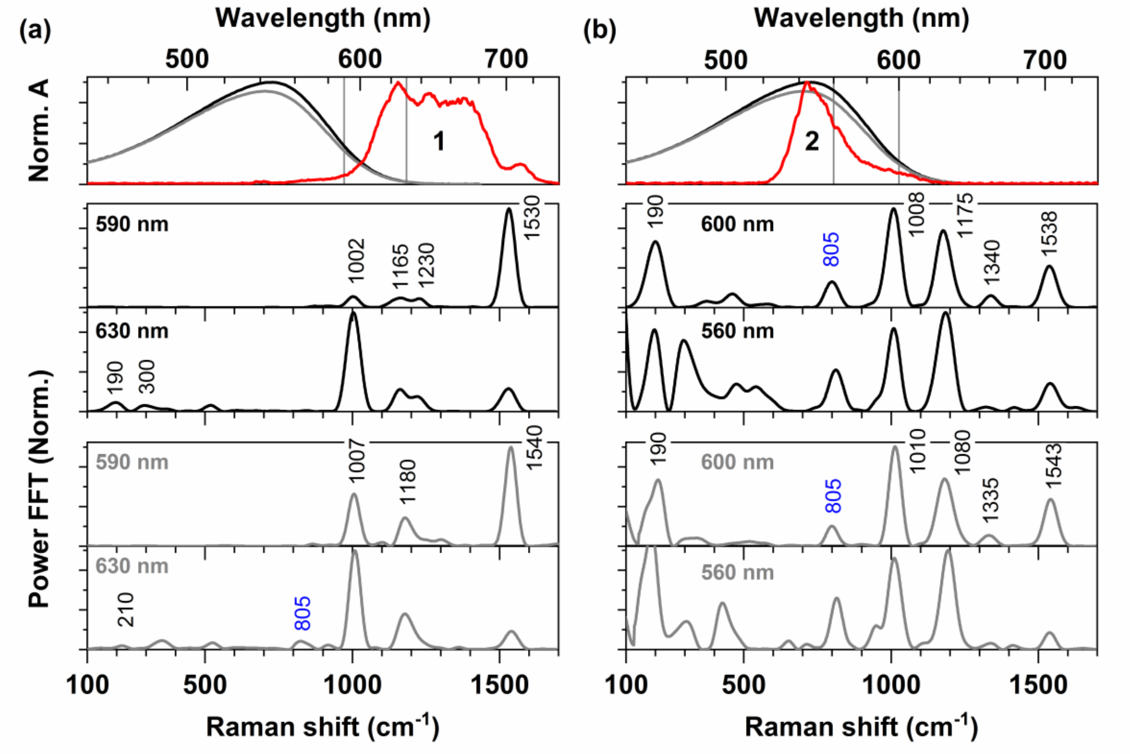

Figure 5.11: DFWM FFT spectra obtained by using near-resonant (1) and resonant (2) excitation spectra for DA (black) and LA (grey) ASR detected at different probing wavelengths shown by vertical grey line in (a) and (b).

combined and explained by an indirect activation mechanism by the high frequency (>1000 cm^{-1}) modes via internal vibrational energy redistribution (IVR) proposed earlier for bR.[105] This is further supported by the observation of the delayed rise of low frequency amplitude compared to the high frequency modes in transient pump-DFWM spectra (Figure 5.7 (e)). Thus, it can be concluded that there are two different activation mechanisms of low frequency (<400 cm^{-1}) modes in the ES manifold: One is weak and directly activated in the Franck-Condon region (detected in the non-resonant DFWM experiments); other is strong and only activated indirectly by the high frequency (>1000 cm^{-1}) modes.

The second question remains about the reason behind the passiveness of the HOOP mode Raman activity in our pump-DFWM experiments. DFWM experiments with two different spectra (Figure 5.11) show that the mode at 805 cm^{-1}, previously assigned as HOOP mode, shows a significantly strong amplitude in resonant DFWM experiment (Figure 5.11(a)) which was very weak in the GS (Figure 5.11(b)). This shows that the HOOP modes are induced only when it is probed with blue-detuned DFWM spectra not with red-detuned DFWM spectrum, used in our pump-DFWM experiment. This observation is very similar to bR[105] and thus, it seems to be an intrinsic molecular property of Retinal.

Frequency shift of the high frequency (>1000 cm^{-1}) modes: The high frequency mode e.g. C=C stretch (1530 cm^{-1} for DA and 1540 cm^{-1} for LA) in non-resonant DFWM FFT spectrum (Figure 5.11(a)) gets blue shifted in resonant DFWM FFT spectrum (Figure 5.11(b)) (1538 cm^{-1} for DA and 1543 cm^{-1} for LA). A similar trend is also observed for CH_3 rocking modes: 1002 cm^{-1} shifts to 1008 cm^{-1} for DA while 1007 shifts to 1010 cm^{-1} for LA. This is expected since non-resonant DFWM FFT spectra contain only GS modes whereas resonant DFWM FFT spectra contain the mixture of GS and ES modes in the high frequency region. As we have shown above, both C=C stretch and CH_3 rock modes show a frequency blue shift in the ES compared to the GS (Figure 5.5).

5.4.4 Pre-twisting and isomerization dynamics

In the context of retinal photochemistry, pre-twisting has been claimed to be one of the potential elements that can accelerate the isomerization process. In particular, the pre-straining inside the protein pocket has been repeatedly shown for visual rhodopsin by both X-Ray crystallography,[49] NMR,[80] resonant Raman studies[84, 141-143] and theoretical simulations[82, 144] which accounts for its fast ballistic IC dynamics. Although non-resonant Raman spectra (Figure 5.2), as reported in this study, speak for a relatively more pre-twisted geometry of 13C isomer in ASR, no significant difference in distortion around the C_{13}=C_{14} between AT and 13C isomers has been pointed out by the X-ray crystallographic study of ASR with 2.0 Å resolution.[50] Very similar observations were made for BR, where the 13C isomer shows 3 times faster kinetics[130] compared to the AT isomer but the structural data report both the isomers to be nearly planar without any indication of protein-catalyzed strain like visual rhodopsin. However, an indirect evidence of weak pre-straining for the 13C isomer was found in the NMR[151] and resonance Raman[146] studies of BR although it seems to be negligible compared to 11-*cis* isomer of visual Rhodopsin. More recently, a closer inspection on the X-ray data depicted a twist around C_{14}-C_{15} bond in 13C isomer but not in AT isomer of bR.[51] Similarly, our classical GS dynamics simulation (Table 5.3) shows no difference in the distortion around C_{13}=C_{14} bond for the AT and 13C isomers; rather it indicates the presence of a twist (~10°) around C_{14}-C_{15} bond for 13C isomer, whereas for AT isomer appears to be almost planar. Thus, this twist around the C_{14}-C_{15} bond, which is adjacent to active C_{13}=C_{14}, plays a center role to accomplish the isomerization faster as claimed for visual Rhodopsin and a small model compound.[162]

This difference in distortions must originate from differences in the packing of the RPSB inside the Retinal pocket. It fits the observation of faster dephasing (Figure 5.8(b)) of GS coherence of the AT than 13C isomers, which can be interpreted as stronger coupling of the AT isomer to the surrounding than the 13C isomer. A recent femtosecond X-ray study[31] of BR has depicted the importance of the specific electrostatic interactions between protein and RPSB to guide the isomerization in certain direction. Hence, this difference in electrostatic interaction between the AT and 13C isomers with the protein surrounding may lead to different trajectories during the reaction. It corroborates a FTIR study[148] which showed that the sub-ps isomerization causes a stronger disruption of the H-bond between the surrounding water molecule and the protonated N-atom of the Schiff base in case of the AT isomer compared to 13C. This H-bond has been previously[45] suspected to be responsible for hindering the rotation of the protonated Schiff base and thus slowing down the isomerization around C_{13}=C_{14} bond. This also matches our observations for the AT ASR of a slower frequency shift of fingerprint modes (C=C and C-C stretches, CH_3 rock), which are sensitive to localized structural changes and have been interpreted as the delayed formation of the twisted transition state for the AT isomer compared to the 13C isomer.

5.5 Conclusion

In this chapter, we have investigated the mechanistic origin of the huge dynamical differences observed in the isomerization of the AT and 13C isomers in Anabaena Sensory Rhodopsin, which address the question raised in the previous chapter. In this regard, the evolution of the GS as well as of the ES structural changes of each isomer has been followed by applying DFWM, IVS, pump-DFWM and pump-IVS spectroscopy techniques. The present experiments were able to unveil three major structural and dynamical differences in the isomerization of each isomer: (i) HOOP activity in the GS is stronger for the 13C ASR than for AT ASR (Figure 5.2), (ii) large (up to 20 cm^{-1}) and delayed transient frequency blue shifts observed for the C=C stretching and CH_3 rock modes in the excited state of AT ASR (Figure 5.5) and (iii) delayed Raman activity increase of low frequency modes (< 400 cm^{-1}) for both AT and 13C isomer where the amplitude appears to relatively stronger for 13C isomer (Figure 5.7).

These experimental findings depict very different isomerization scenarios for each isomer. The stronger HOOP activity at about 805 cm^{-1} in the GS spectra of LA ASR indicates that the 13C isomer is already more pre-twisted in the GS than the AT ASR isomer inside the Retinal pocket. Bearing analogy to BR and support of theoretical calculations, we have assigned this mode to C_{14}-H wag. Our results point to a distortion located around the C_{14}-C_{15} bond of the 13C isomer, which is neighboring to the isomerizing C_{13}=C_{14} bond. The evolution of frequency shifts of high frequency modes, in particular of the C=C stretching and CH_3 rock modes, depicts a much slower formation of the twisted configuration for the AT ASR compared to the 13C ASR.

Finally, a major contrast in the vibrational dynamics of AT and 13C isomer was found in the activation of these low frequency modes which is assigned to the torsional modes delocalized over the Retinal chain. It appears to be much stronger under LA condition compared to DA condition. First, these low frequency modes were assigned to the excited state which are mostly activated by the C=C bond via IVR mechanism in the view of two facts: (i) the delayed rise of its amplitude in the transient nonlinear Raman spectra and (ii) the stronger relative amplification of these modes from non-resonant to resonant DFWM experiments. It is in agreement with the previous results,[27, 104-105] which showed that the delocalized torsional modes of Retinal gets activated by the energy, funneled from the C=C bond via IVR mechanism. Therefore, the stronger activity of these modes would mean more efficient energy funneling. Since it takes more energy for the AT isomer to break the π-delocalization than the 13C isomer (where the π-delocalization is weaker due to the pre-distorted geometry), a large amount of energy is left after initial excited state relaxation process for the 13C isomer, which can be transferred to the torsional modes. Thus, this can account for very strong low frequency delocalized motion of retinal backbone in LA ASR. This observation is also supported by the FTIR study,[145] where it was concluded that the isomerization causes a widely distributed structural change for the 13C isomer but it only causes a localized change near the schiff base region in case of AT isomer.

These discoveries have profound implications in understanding the mechanism of the primary events in retinal proteins. 13C ASR and AT ASR show several dynamic and spectral features known for other respective isomers in other retinal proteins, in particular bR. The indirect activation of low frequency modes via IVR, for example, observed in ASR and bR further stresses the similarities and implies that this mechanism is more general than thought before. Perhaps more important than this is the very distinct evolution of high frequency modes in the excited states of 13C and AT ASR. While e.g. C=C stretching and CH_3 modes are not reactive coordinates per se, they certainly reflect the structural changes taking place at localized positions along the retinal during the isomerization. The delayed decrease of the conjugated double bond length observed for AT ASR in the excited state compared to 13C ASR surely follows the previous proposal about the presence of barrier in the excited state manifold of AT ASR. Nevertheless, our findings suggest that the slower dynamics observed for AT ASR may originate due to more than one factor, namely a barrier in the excited state or the lack of a pre-distortion (compared to 13C) in the ground state. Although the HOOP activity in 13C ASR is much lower than for 11-*cis* in visual rhodopsin, the excited state lifetimes are not very different. This further reinforces that not a single effect is playing a role in determining the excited state lifetime, as has been advocated in the past.

Chapter 6

Effect of Point Mutation on Isomerization Dynamics of Anabaena Sensory Rhodopsin[2]

In the last two chapters, the influence of the ground state retinal configurations on its isomerization dynamics has been thoroughly investigated. Another central element in the retinal isomerization reaction dynamics is the opsin moiety surrounding the bound retinal protonated schiff base (RPSB) inside the retinal pocket. It has been observed that the photo-induced retinal isomerization inside the protein pocket completes in sub-ps timescale with formation of a single stereo-specific product,[29-30, 68-70, 72-74] whereas the same reaction in organic solvents takes much longer time (>1 ps) to complete and generates more than one stereo-isomeric product. [25-26, 75-76, 163] To shed more light on this issue, a few comparative pump-probe studies between of wild-type (WT) and mutants of bacteriorhodopsin (BR) have been performed,[85, 164-166] in which a single charged amino acid residue was replaced by a neutral one. It showed more than four folds deceleration of the reaction rate for the mutants compared to the WT BR. All these observations depict the importance of the protein constructions surrounding the RPSB to drive such a fast highly stereo-selective isomerization reaction. However, none of those studies have confirmed which molecular modes are tuned by the protein-chromophore interaction in order to drive the reaction into the desired reactive trajectory.

---

[2] This chapter includes a part of the contents (e.g. data, figures, text) used in the manuscript: "*Pre-distortion of retinal chromophore due to point mutation of Anabaena Sensory Rhodopsin leads to shorter excited state lifetime*", P. P. Roy, R. Abe-Yoshizumi, H. Kandori and T. Buckup, *in preparation.*

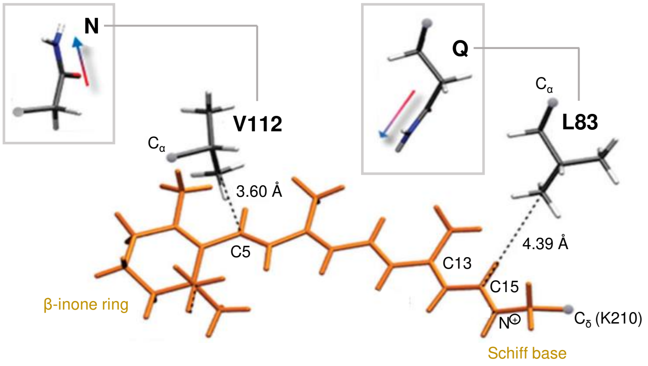

Figure 6.1: Mutation in Anabaena Sensory Rhodopsin was performed by replacing a non-polar amino acid residue by a polar one. In V112N mutant, valine112 (V112) was replaced by asparagine (N), whereas in L83Q, leucine83 (L83) was replaced by glutamine (Q). In the former the mutation was done in close proximity of the β-inone ring and in the latter it was done close to the schiff base moiety of the bound RPSB, respectively. The arrows provide a qualitative view of the dipole moment direction associated with the corresponding wild-type or mutant side-chain. This figure is reproduced from reference 172 with permission from the PCCP Owner Societies (Copyright 2012 Royal Chemical Society)

In addition, it is still not clear whether the electrostatic interaction[85, 167-169] or the steric effect[64, 170-171] or both are responsible for that. One possible way to answer this open question is to compare the isomerization dynamics in the WT and mutated proteins and correlate to the structural changes of the bound RPSB. In this chapter, a comparative study of the population kinetics of WT Anabaena Sensory Rhodopsin (ASR) and its mutants have been done by performing a set of transient absorption (TA) experiments. Later, these have been correlated with the corresponding changes in molecular vibrational modes (both in ground and excited states), which are tracked by recording corresponding Raman spectra with the help of the coherent vibrational spectroscopy. Furthermore, ASR being a unique retinal protein to incorporate all-*trans* (AT) and 13-*cis* (13C) isomers inside the same protein cavity, provides an additional advantage to observe the differential effects of the mutations on the two isomers.

For that purpose, two mutants (L83Q and V112N), each with a single mutation at distinct location of the protein pocket, have been studied in order to rationalize the influences of different part of the opsin moiety in guiding the isomerization reaction. In each mutant, one non-polar amino acid residue, which is in less than 5Å distance from the RPSB, was replaced by a polar one of comparable size (Figure 6.1). In the case of L83Q, the mutation was done in close proximity of Schiff base moiety by replacing a leucine (L) with glutamine (Q), whereas for the V112N, the mutation was done close to β-inone ring of the RPSB by replacing valine (V) with asparagine (N) (Figure 6.1).

6.1 Ground state absorption

The primary effect of the mutation was observed in UV-Visible steady state absorption spectra (Figure 6.2(a)-(c)). The mutation caused a blue shift of ~20 nm for V112N and ~30 nm for L83Q ASR. This indicates an increase in S_0-S_1 energy gap for the mutants compared to the WT ASR, which is in agreement with previous reports.[87, 172] A secondary shift of the absorption λ_{max} was observed by changing the adaptation conditions from dark to light. It results in a blue shift of 6 and 2 nm for WT and V112N, respectively and a red shift of 3 nm for L83Q (Figure 6.2 (a)-(c)).

In order to estimate the isomeric composition in the ground state under dark and light adaptation conditions for each sample, a set of HPLC analysis was carried out (Figure 6.2 (c)). It was found out that both V112N and L83Q ASR contain AT isomers almost exclusively under the dark adapted condition like the WT ASR (Figure 6.2 (c)). Under the light adaptation condition, both mutants

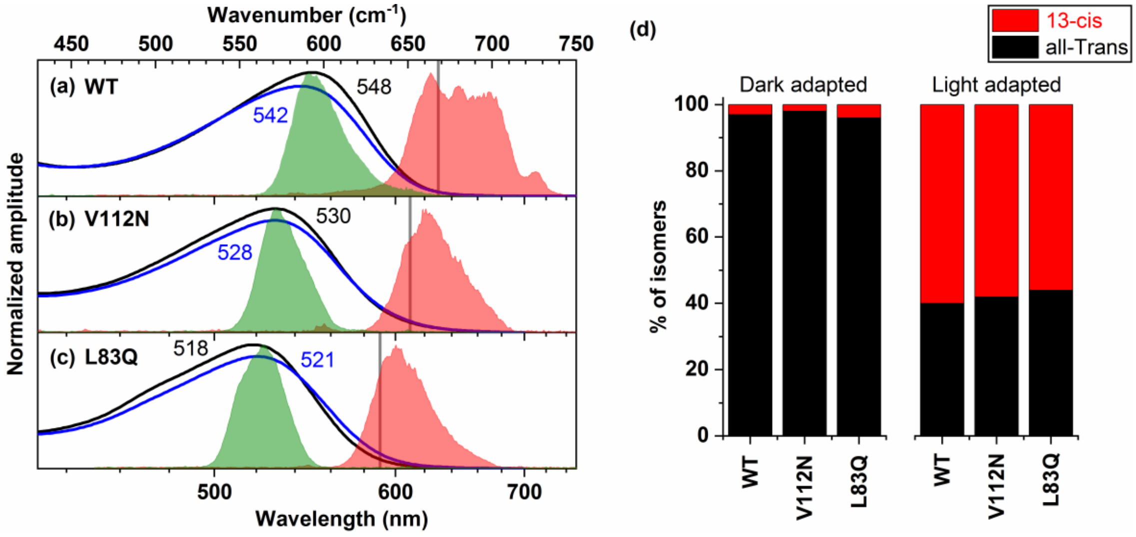

Figure 6.2: Ground state absorption spectra of (a) WT ASR and its mutants (b) V112N and (c) L83Q under dark (black lines) and light (blue lines) adapted conditions. Green solid curves represent excitation or actinic spectrum used for the transient absorption and pump-DFWM measurements, whereas the red solid curves represent degenerate four wave mixing spectrum. Vertical grey line each graph denotes the wavelength of detection of (pump-) DFWM signals. (d) The isomeric ratio of all-trans and 13-cis isomers under dark and light adapted conditions, obtained from HPLC analysis.

contain an isomeric mixture, where the major component is the 13C isomer (~60%). Thus, the secondary shifts of the steady state absorption spectra upon light adaptation are caused by the change in compositions of the AT and 13C isomers. This is again similar to the WT ASR. Here, it is important to note that, an LED with an illumination spectrum centered at 590 nm (as shown in Figure 4.1) was used for the light adaptation of the WT ASR, whereas an LED with an illumination spectrum centered at 490 nm was used for the light adaptation of the mutants. The illumination by such a light source with a spectrum centered at this particular wavelength helps to achieve the maximum difference in the composition between the 13C and AT isomers of each sample in the light adapted photo-stationary equilibrium state. Since each sample under dark and light adapted conditions contain predominantly AT and 13C isomers, respectively (Figure 6.2 (c)), the differences in the optical signals under two adaptation conditions would reflect the distinct features exhibited by the two isomers.

6.2 Broadband transient absorption

A set of broadband TA measurements was carried out to compare population kinetics of the WT ASR with its mutants under both dark and light adapted conditions. For each sample, a spectrum centered at the maxima of the respective steady state absorption spectrum was used for the excitation (Figure 6.2 (a)-(c)). A comparison between TA spectra of the WT ASR and V112N, L83Q mutants at different pump-probe delays under the dark adapted condition has been illustrated in Figure 6.3. It shows a very similar general appearance of the spectral bands (Figure 6.3) for the mutants as observed for WT ASR (see section 4.2 for more details). For instance, a fast decaying excited state absorption (ESA) and a long lived photo-induced absorption (PIA) band was observed in blue (<500 nm) and red (>600 nm) detuned wavelength of a ground state bleach band (GSB) band in each sample. Nevertheless, the maxima of the GSB bands in the mutants were blue shifted compared to the WT, which is expected keeping the blue shifts of corresponding ground state absorption λ_{max} in mind (Figure 6.2). In the far red detuned spectral region (>700 nm) of the GSB bands, a red shifted rapidly decaying negative band was detected for each sample. This is assigned as a signature of stimulated emission (SE) in analogy with the WT ASR. Furthermore, transient shifts of these spectral bands during the initial excited state relaxation (e.g. blue shift of the ESA or red shift of the SE bands) for the mutants are analogous to the WT ASR. Similar features of the

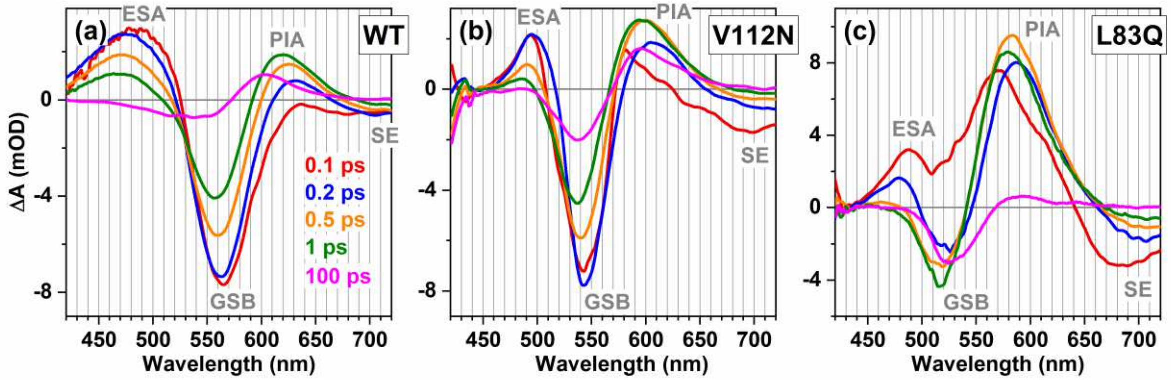

Figure 6.3: The TA spectra of (a) WT ASR and its mutants (b) V112N and (c) L83Q at different pump-probe delays (0.1, 0.2, 0.5, 1 and 100 ps) under dark adapted condition. Different characteristic peaks: Excited state absorption (ESA), Ground State Bleach (GSB), Stimulated Emission (SE), Photo-induced absorption (PA) appear along the probe delays are marked in each graphs. Very similar features in TA spectra are observed under light adapted conditions (not shown here), only the decay constants differ.

TA spectra for all three samples were also observed under the light adapted condition (not shown here).

In spite of these resemblances, two main contrasts appear in the TA spectra for both isomers of the mutants compared to that of the WT ASR. Firstly, the relative amplitude of the PIA band with respect to GSB band appear to be much stronger for the L83Q compared to the WT as well as V112N (Figure 6.3). The reason behind the stronger PIA band could be the shift of the negative GSB signals to blue detuned wavelength for the L83Q, which usually cancels out the positive ESA signal in the WT ASR. The second contrast appears in the decay rates of the spectral bands. They were significantly different in the mutants compared to the WT ASR, which immediately suggest a difference in the isomerization reaction times. A comprehensive analysis of analogous broadband TA data of the WT ASR and its mutants has been presented by Agathangelou *et al.*[87] According to this report the isomerization reaction times can be arranged in a descending order: WT (770 fs) > V112N (230 fs) > L83Q (120 fs) for AT isomers and V112N (290 fs) > L83Q (200 fs) > WT (170 fs) for 13C isomers. Our results are in good agreement with this reported values (fitting of the broadband TA data set has not been presented in this thesis. Readers are referred to the reference[87] for further details.). Hence, it is concluded hereby that the mutations cause a profound acceleration of the isomerization dynamics of the AT isomers, whereas the dynamics of the 13C isomers remain much less affected.

6.3 Coherent vibrational dynamics

After comparing the electronic population dynamics, our aim is to compare the associated coherent vibrational dynamics. As discussed in section 1.4, coherent excitation of vibrational wave packet is possible by using an ultrashort pulse for excitation in the TA measurements. However, in order to track the excited vibrational oscillation, a high time resolution (<30 fs) is required. It was not possible to achieve in the broadband TA measurements shown in last section because a chirped white-light was used as probe. A compressed pulse derived from a nc-OPA, however, can fulfill this criteria of high time resolution (<30 fs) (see Figure 3.1). The corresponding probe spectrum is shown in Figure 6.2 by the solid red curves. With this probe spectrum, the initial 1.5 ps of the spectro-temporal evolution of difference absorption spectra ranging from 570 to 670 nm was captured by varying the pump-probe delay under both dark and light adapted conditions (Figure 6.4 (a)-(f)). This particular spectral range was chosen as the PIA band appears in this region for each sample, where the initial ESA and subsequent photoproduct absorption bands overlap (see

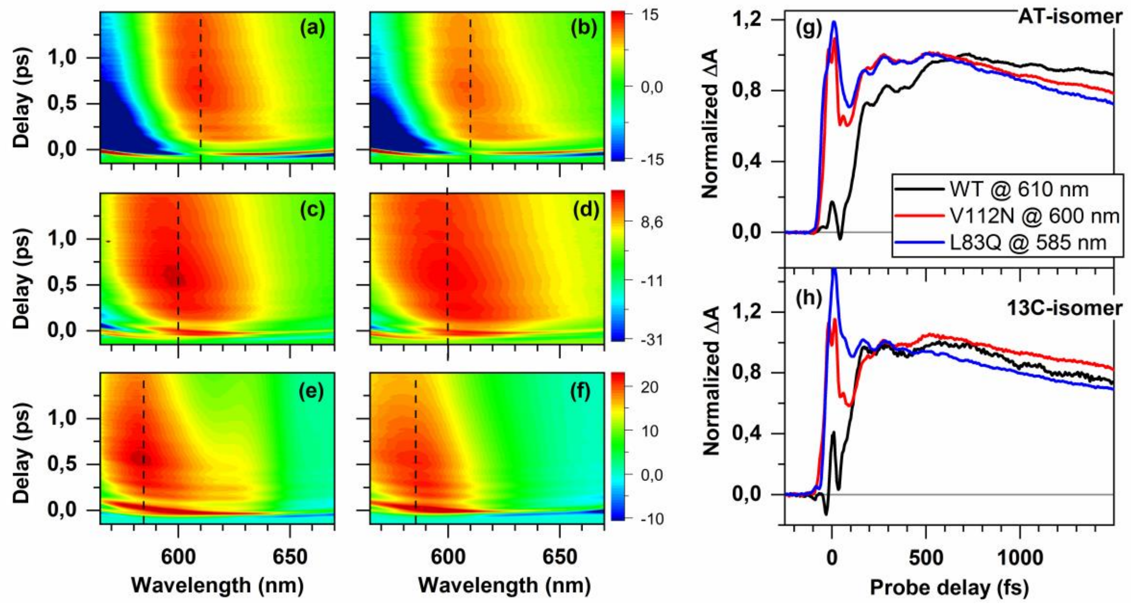

Figure 6.4: The spectro-temporal evolution of difference absorption spectra for wild type (a, b) ASR and its mutants (c, d) V112N and (e, f) L83Q. The graphs on the left (a, c, e) and right column (b, d, f) represent the difference absorption spectra measured under the dark and light adapted conditions, respectively. The retrieved transients for AT and 13C isomers of three different samples (WT, V112N and L83Q) detected at the probing wavelengths: 610, 600 and 585 nm, respectively (shown by black dotted lines in 2D graph), are compared in graph (g) and (h).

Figure 6.3). Thus, it enables one to evaluate the vibrational dynamics predominantly associated with the excited or photoproduct potential surface of each ASR sample and compare them.

Before evaluating the coherent vibrational dynamics, a comparison of the electronic population kinetics has been done to show the agreement of two different sets of TA measurements. For that, the TA signal associated with the individual isomer (AT and 13C) of each ASR sample was extracted by taking a linear combination (see section 3.3.3) of TA data sets measured under the dark and light adapted conditions. In Figure 6.4 (g) and (h), the transients detected at the wavelength around the maxima of the PIA bands for each sample (620 nm for WT, 600 nm for V112N and 585 nm for L83Q ASR) are plotted after normalizing each one to its maximum beyond the coherent artefact (>100 fs). In each transient, the signal rises initially (<1 ps) representing the formation of the photo-product and decays afterwards indicating subsequent relaxation of the vibrationally hot photo-product. A comparison of normalized transients for each isomer of the WT,

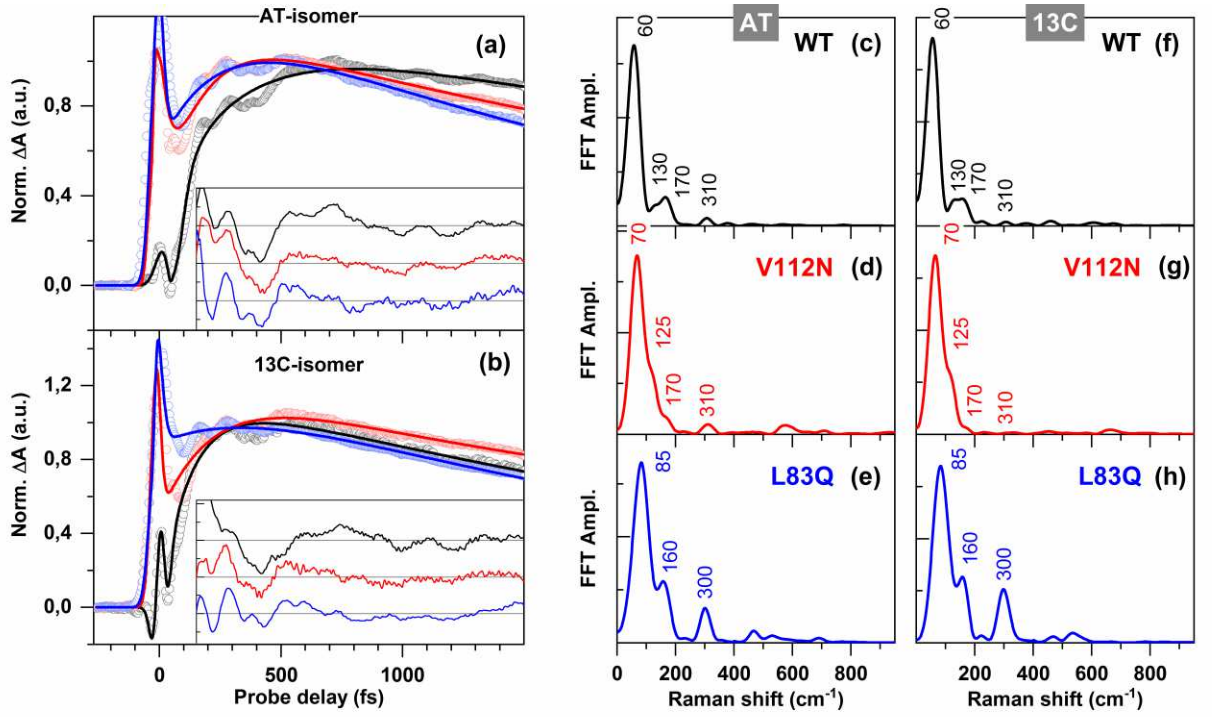

Figure 6.5: The transients of (a) AT and (b) 13C-isomers obtained from transient absorption experiments, where an ultrashort probe pulse was used. The black, red and blue circles represent the transient for WT, V112N and L83Q ASR, respectively and the respective transients were detected at 620, 600 and 585 nm. Each transient was normalized to the maximum signal beyond 100 fs. The oscillatory residuals obtained after subtraction of the population kinetics by a bi-exponential fit (solid lines) of the transients are shown in the inset. (c-h) The respective spectra obtained by a fast Fourier transformation of the residuals.

V112N and L83Q ASR (Figure 6.4 (g)) corroborates the results of previous TA measurement with white-light probe.

The coherent vibrational dynamics appear as an oscillatory feature on top of the exponential decay of the electronic signal (Figure 6.5). It is more evident on the residuals (see inset of Figure 6.5(a) and (b)) obtained after subtraction of the bi-exponential electronic population kinetics from the transient. The residuals exhibit damped periodic modulations (~2 mOD), which are well beyond the noise level (<0.1 mOD). A fast Fourier transformation (FFT) (Figure 6.5(c)-(h)) of the residuals allows to quantify the vibrational modes contributing to the oscillatory residuals. Multiple number of low frequency modes are present below 400 cm^{-1} with a dominant mode appearing around 60-90 cm^{-1} for both AT and 13C isomers of each sample (Figure 6.5(c)-(h)). In addition, a few minor modes appear around 100-350 cm^{-1}. It is difficult to rationalize the minor frequency shifts observed from the WT to the mutants for those closely spaced modes below 200 cm^{-1} as these are strongly overlapping. Nevertheless, the mode at 300 cm^{-1}, which is devoid of any spectral overlap, shows relatively stronger amplitude for the L83Q compared to the WT and V112N ASR. Although all these low frequency (<400 cm^{-1}) modes are detected over the spectral region where the PIA band (see Figure 6.3) predominates, a substantial contribution of the GSB also overlaps. Therefore, the assignment of these modes to a particular electronic state is not trivial and require further inspection.

6.4 Ground state vibrational spectra

In order to extract the pure ground state vibrational modes, a set of DFWM experiments were carried out with a degenerate spectrum (red solid curved in Figure 6.2), which is almost non-resonant to the ground state absorption spectra of the respective samples.. The DFWM transients, shown in Figure 6.6, were detected at 20 nm blue detuned wavelength from the center of the respective the DFWM excitation spectra used for each sample (shown by vertical lines in Figure 6.2). The subtraction of non-oscillatory component from the transient by an exponential fit gives a residual (see insets of Figure 6.6), where the high frequency oscillation with period <40 fs dominates. A Fourier transformation of these residuals yield the Raman spectra shown in Figure 6.7. In contrast to the observations of low frequency (<400 cm^{-1}) modes observed in the TA measurements (Figure 6.5), DFWM FFT spectra (Figure 6.7) show major contributions of

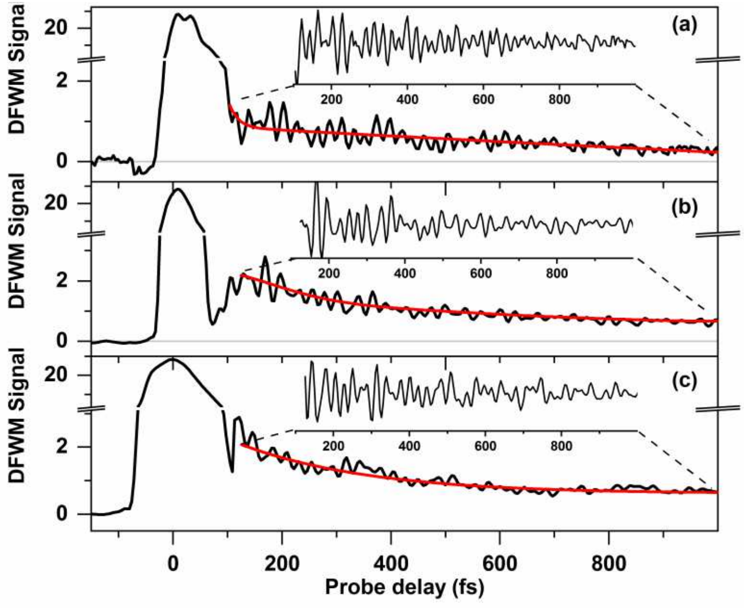

Figure 6.6: Transients obtained for the DFWM experiments of (a) WT, (b) V112N and (c) L83Q mutants of ASR detected at 630, 610 and 590 nm (shown in Figure 6.2) under the dark adapted conditions. The insets show the oscillatory residuals obtained after subtracting the non-oscillatory component by an exponential fit (red lines) of each transient.

vibrational modes appearing in the spectral region above 800 cm^{-1} for all samples; only a very weak activity below 600 cm^{-1} is observed only for WT ASR.

A comparison between the DFWM FFT spectra of the AT isomers (~dark adapted) of the WT and the mutants (Figure 6.7 (a)-(c)) shows two major differences: (i) a considerable Raman activity around 750-950 cm^{-1} (grey shaded spectral region in Figure 6.7) was detected for both the mutants: V112N (805, 900 cm^{-1}) and L83Q (820, 900 cm^{-1}), which are almost absent in case of the WT ASR; (ii) frequency shift of the modes above 1000 cm^{-1} was observed from the WT to the mutants. In particular, the modes at 1003 and 1530 cm^{-1} for the WT ((Figure 6.7 (a)) shift to 1007 and 1535 cm^{-1} for the V112N ((Figure 6.7 (b)) and to 1007 and 1543 cm^{-1} for the L83Q ASR ((Figure 6.7 (c)), respectively. In addition, the double peaks at 1160 and 1230 cm^{-1} for WT merges to a single peak (1186/1180 cm^{-1}) for both the mutants. In contrary to the AT isomers, the mutation does not bring any significant change in the spectra of 13C isomers (~light adapted) (Figure 6.7 (d)-(f)). Neither any significant shift of the modes above 1000 cm^{-1} nor any substantial

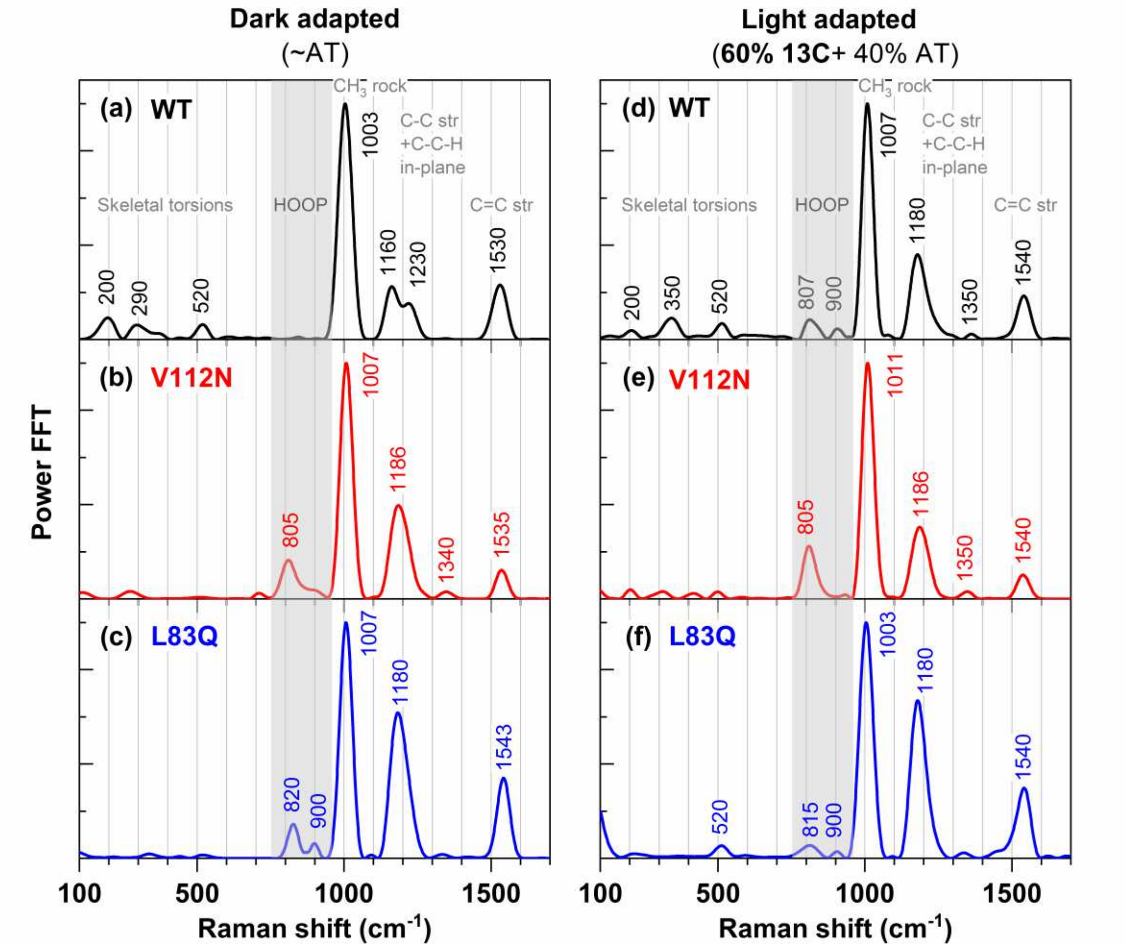

Figure 6.7: The power FFT spectra obtained by fast Fourier transformation of the residuals obtained after the exponential fitting of the DFWM transients (see Figure 6.6) for (a, e) WT (b, d) V112N and (c, f) L83Q under the dark (a, b, c) and light (d, e, f) adapted conditions. Assignment of the vibrational modes are shown on top. The grey shaded area represents the characteristic spectral regions (750-950 cm 1) for hydrogen-out-of-plane (HOOP) modes of retinals.

change in the amplitude of the modes in the region 750-950 cm^{-1} is observed when the Raman spectra of the WT was compared with that of the mutants.

6.5 Pump-degenerate four wave mixing

In order to evaluate the impact of mutation on the excited state evolution of the vibrational modes, a set of pump-DFWM measurements were performed. In these measurements, actinic spectra used for each sample were same as those used for the excitation in the TA measurements of the

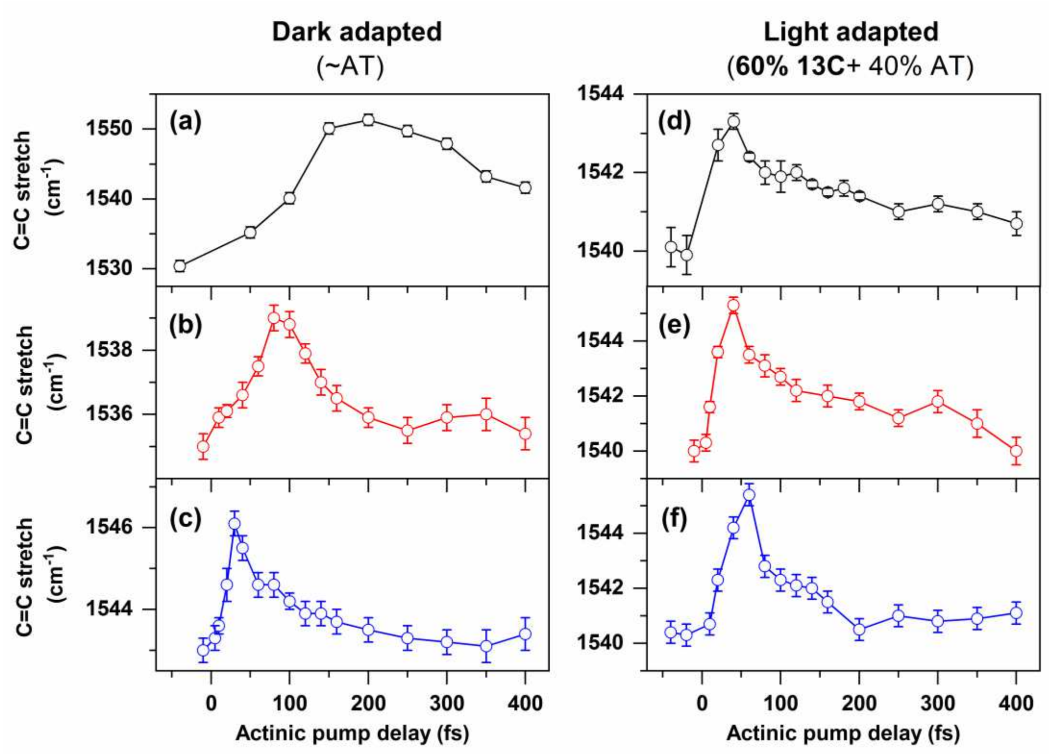

Figure 6.8: Comparison of the frequency shifts of the C=C stretching modes, obtained from a pump-DFWM measurements on (a, d) WT ASR and its mutants (b, e) V112N and (c, f) L83Q dark (a, b, c) and light (d, e, f) adapted conditions. The pump-DFWM signals for the WT, V112N and L83Q ASR were detected at 620, 600 and 585 nm, respectively.

respective samples (see green solid curves in Figure 6.2). The DFWM spectrum (see red solid curves in Figure 6.2) was same that used for the non-resonant DFWM measurements in the last section. This particular spectrum was chosen as it is resonant to initial ESA band (Figure 6.3) of each ASR sample under investigation. This facilitates to track the evolution of the excited state vibrational modes predominantly, by varying the actinic pump delays as illustrated for WT ASR in section 5.3 in the last chapter. The measurements were carried out under the dark (~AT) and light adapted (majorly 13C) conditions to access the differential effect of the mutation on the excited state evolution of AT and 13C isomers of ASR. In general, the evolution of the pump-DFWM FFT spectra shows a transient frequency shift of the high frequency (>1000 cm^{-1}) modes and a relative increase in amplitude of low frequency modes for both mutants as it is depicted for the WT ASR in Figure 5.5and Figure 5.7 in the last chapter. Here, the frequency shift of the mode around 1530-1550 cm^{-1}, which are assigned to C=C stretching mode (see section 5.1), is found to be major contrast between the excited evolution of the vibrational spectra of the WT

ASR and its mutants. All other features are very similar (not shown) to the dynamics observed for the WT.

Figure 6.8 illustrates that both mutants exhibit initially a rapid blue shift and subsequent slow red shift of C=C stretching modes as the reaction proceeds (Figure 6.8). This trend is qualitatively same to that of the WT ASR. However, the timescale, in which it undergoes the blue shift, differs from the WT ASR, particularly for the AT isomers (~dark adapted). It takes ~200 fs for the WT to reach the maximum frequency shift, while it takes only ~80 fs for the V112N and almost instantaneous for the L83Q (Figure 6.8(a)-(c)). In contrast, the 13C isomers (~light adapted) of both WT and the mutants exhibit the blue shift almost instantaneously (Figure 6.8(d)-(f)).

6.6 Discussion

6.6.1 Ground state spectra

All experimental results presented in this chapter illustrate the effect of the point mutations on the isomerization dynamics of ASR. The primary effect of the mutation appear in the steady state absorption, which indicates an increase in the S_0-S_1 energy gap from the WT ASR to its mutants. This change in energetics has been explained by calculating the energy of the electronic states via QM/MM methods.[172] It showed that the relative stabilization (destabilization) of the S_0 (S_1) state with respect to S_1 (S_0) state as a consequence of the substitution of a non-polar (V/L) amino acid with a polar (N/Q) one. In particular, it is well known for the RPSB that $S_0 \rightarrow S_1$ excitation causes

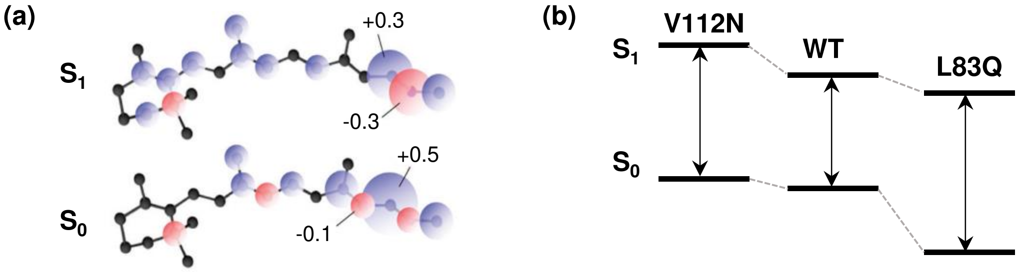

Figure 6.9: (a) Distribution of electronic density in S0 and S1 states, obtained by performing a QM/MM. This figure is reproduced from reference with permission from the PCCP Owner Societies (Copyright 2012 Royal Chemical Society) (e) Schematic representation of the change in S0 and S1 energy levels upon mutation.

the positive charge over the Schiff base N-atom to spread towards the β-inone ring (Figure 6.9 (a)). Consequently, in the S_0 state, the positive charge resides predominantly over the Schiff base region, whereas this positive charge is distributed along the chain in the S_1 state. In the case of L83Q mutants, negative dipole of the glutamine (Q) residue, which is close to the Schiff base N-atom (Figure 6.1), stabilizes S_0 state more compared to S_1 state. This causes a blue shift. For V112N, positive pole of the asparagine (N) residue is oriented towards the β-inone ring and therefore, it destabilizes the S_1 state with respect to S_0 state. As a result, both the point mutations cause a blue shift in their ground state absorption spectra with respect to the WT ASR.

6.6.2 Isomerization dynamics and ground state vibrational spectra

Other than the change in energetics, the major effect of the mutation was observed in the isomerization dynamics (Figure 6.4) and the ground state vibrational spectra (Figure 6.8), especially for the AT isomers of ASR. Comparison of the isomerization dynamics with ground state Raman spectra of respective sample indicates a strong correlation between the acceleration of isomerization dynamics and the FFT amplitude of the ground state modes appearing in the region of 750-950 cm^{-1} (Figure 6.8), which are assigned to the hydrogen-out-of-plane (HOOP) wag motions.[84, 142] In particular, the mutation causes dramatic shortening of the excited state lifetime of the AT isomers, whereas it has a minor effect on the isomerization rate of the 13C isomers. It correlates with the gain in the HOOP activity, which increases significantly for the AT isomers of the mutants compared to the WT, but remains almost equally active for the 13C isomers of both the WT and mutants. In general, the HOOP activity is considered as an indication of structural non-planarity.[62, 84, 142, 146] In our study, the main activity of these modes was observed around 800-820 cm^{-1}, which is assigned to C14-H wag mode for bacteriorhodopsin.[146] Hence, it indicates a distortion either around active C13=C14 bond or neighboring C14-C15 bond of ground state AT isomers in the mutants which is almost absent for WT ASR. The scenario is quite different for 13C isomers, which show a noticeable HOOP activity already for WT and mutation bring only a minor change in its HOOP activity. It hints at similar extent of distortion for 13C isomers of both WT and mutants.

The second major aspect of the mutation was the frequency shift of the ground state modes above 1000 cm^{-1} (Figure 6.8), which are assigned as follows: 1500-1550 cm^{-1} (C=C stretch), 1100-1400 cm^{-1} (C-C stretch often coupled to C-C-H in-plane-rock), 1000-1010 cm^{-1}

(CH_3-rock).[84, 141, 146] The frequency shifts of these localized modes are rationalized as the difference in σ and π-electronic distributions. In particular, the blue shift of C=C stretch modes of AT isomers of WT to the mutants hints at a reduction in π conjugation (see section 5.4.2). In contrast, the mutation does not shift these high frequency modes for the 13C isomers. It is in line with our previous observation of HOOP activity, hinting at a distortion because a non-planarity immediately leads to reduction in π-conjugation in any bio polyene.[160] Moreover, the contrasts between the ground state spectra of the AT isomers of the WT and the mutants are resembling the difference between AT and 13C isomers of WT ASR, which have been accounted as a signature of pre-twist in section 5.4.3.

6.6.3 Low frequency vibrational modes

In contrast to the DFWM FFT spectra (Figure 6.8), a profound activity of the low frequency (<400 cm^{-1}) modes are observed in the TA measurements (Figure 6.5(c)-(h)). The major mode appearing around 60-90 cm^{-1} for all the samples, is reminiscent to a low frequency mode observed over the PIA band for visual rhodopsin (~60 cm^{-1}).[29] A similar low frequency mode was also reported for WT ASR (~55-65 cm^{-1}).[90] In addition, multiple minor peaks around 100-350 cm^{-1} are observed for both WT and mutants. A mode at 170 cm^{-1} was reported for bacteriorhodopsin in both transient absorption[138] and fluorescence[171] measurements. A recent study by Wand *et al.*[98] has

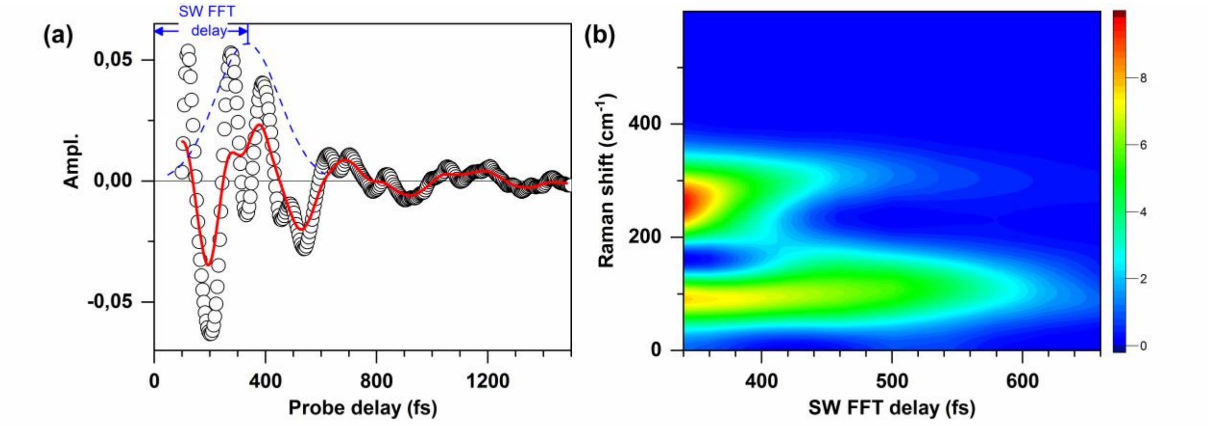

Figure 6.10: (a) The residual obtained after the bi-exponential fit (shown in Figure 6.5) of the transient of the L83Q ASR measured under the dark adapted condition. The red curve represents the resultant after passing though low frequency filter with a cut-off 200 cm^{-1}. (b) Spectrogram obtained by a sliding window Fourier analysis of the residual by applying a Gaussian window, shown by blue dotted line in graph (a), which has FWHM temporal width of 400 fs.

reported multiple modes at 160, 210 and 300 cm^{-1} for the WT ASR as well as for bacteriorhodopsin in the near IR region (950-1200 nm), where only the stimulated emission appears devoid of any ground state dynamics. Hence, these modes were assigned exclusively to the excited state. However, no mode was observed to appear below 100 cm^{-1} in this report. In our study, the dominant mode, appearing below 100 cm^{-1} for all sample, is found to survive longer than 1 ps (Figure 6.10). Hence, it is less likely to be originated from the excited state considering its short lifetime (<0.3 ps except AT isomer of WT). The 300 cm^{-1} mode, however, shows a much faster dephasing rate (<100 fs) compared to the mode below 100 cm^{-1} (~500 fs) revealed by a sliding window FFT analysis (Figure 6.10). It agrees with the previous assignment of 300 cm^{-1} mode as the excited state mode.[98]

It has been well established that these low frequency (<400 cm^{-1}) modes, which represent the skeletal torsion of the retinal backbone, are mainly activated impulsively by the high frequency modes via intermolecular vibrational energy redistribution (IVR) (see section 5.4.3).[27, 104-106] This speaks for its absence in ground state spectra and strong activity in the TA signals. Earlier report for retinal in solution showed the low frequency mode (~120 cm^{-1}) to be independent of the solvent properties.[171] The same mode gets blue shifted (~170 cm^{-1}) inside the retinal pocket of bacteriorhodopsin but locking the active C13=C14 bond does not affect this torsional mode.[138] It indicates that these modes are not sensitive to the localized change rather depends on the overall spatial charge distribution surrounding the chromophore. It fits to our observation of unaltered nature of these modes after point mutations, which usually bring only localized changes in the charge distribution. Furthermore, several experiments indicated that these low frequency skeletal torsions may guide the reaction by twisting the chromophore towards conical intersection (see reference[173] and the references therein). In view on the insensitivity of the low frequency modes to the mutation, even when the isomerization dynamics is drastically altered, it is very less likely for these modes to represent the reactive coordinate of the reaction.

In contrast to the modes below 200 cm^{-1}, a relative increase of the FFT amplitude of 300 cm^{-1} modes was observed for the L83Q ASR compared to the WT and V112N (Figure 6.5). This is explained here due to relatively stronger ESA amplitude with respect to the GSB for L83Q in comparison to WT and V112N ASR (Figure 6.3). This increases the amplitude of the modes belonging to the excited state (300 cm^{-1}) compared to those belonging to the ground state (60-90 cm^{-1}).

6.6.4 Excited state evolution

In contrast to the coherently excited low frequency modes, the high frequency modes, especially the C=C stretching modes show a transient frequency shift for both WT and mutants (Figure 6.8) as the reaction proceeds. Each one undergoes a rapid blue shift, which is followed by a slower red shift. On the one hand, a comparison of the reference time, at which maximum blue shift occurs for the AT isomers of all three ASR samples, shows that it becomes substantially shorter for the mutants in comparison to WT ASR (Table 6.1). On the other hand, for the 13C isomers the blue shift is found to be almost instantaneous for both WT and mutants. This correlates to the isomerization reaction times of respective ASR sample. Furthermore, a similar correlation between the isomerization reaction time and the amplitude of the frequency shift exits can also be observed.

In last chapter, the observed blue frequency shift of the C=C stretching modes, in general, has been interpreted as a change in effective conjugation length of the pi-conjugated retinal system due to the rotation around the active C=C bond during the isomerizing reaction (see section 5.4.2). Therefore, the time-scale, at which the maximum frequency shift occurs, has been considered as a qualitative reference time for the retinal system to reach a twisted state. Faster the RPSB reaches that twisted state faster the isomerization completes and shorter the excited lifetime. This explains the linear correlation between this reference time and the isomerization reaction time. It also indicates that the frequency of the C=C stretching mode of the RPSB provides an alternative

Table 6.1: Correlation between the center frequency shift of the C=C stretching mode and isomerization reaction times of different ASR samples under the dark and light adapted conditions.

Sample		Time to reach maximum frequency shift	Maximum amplitude of the blue shift	Isomerization reaction time
AT isomers (~dark adapted)	**WT**	200 ±10 fs	~21 cm^{-1}	770 ±20 fs
	V112N	80 ±10 fs	~4 cm^{-1}	230 ±20 fs
	L83Q	30 ±10 fs	~3 cm^{-1}	120 ±30 fs
13C isomers (~light adapted)	**WT**	40 ±10 fs	~3 cm^{-1}	170 ±40 fs
	V112N	40 ±10 fs	~6 cm^{-1}	290 ±50 fs
	L83Q	60 ±10 fs	~5 cm^{-1}	200 ±40 fs

parameter to monitor the isomerization reaction other than following its transient electronic spectra. In order to explain the second correlation between isomerization reaction times and the amplitude of blue frequency shifts of the C=C stretching mode in pump-DFWM spectra, one need to remember the pump-DFWM transients contains a mixture of ground state and excited vibrational coherences. Now, longer the excited state life time, larger the contribution of the excited state coherence in the pump-DFWM transient and consequently, larger the frequency shift in the pump-DFWM FFT spectra.

6.7 Conclusion

In summary, we investigated the effect of mutation on high (>1000 cm^{-1}) and low (<400 cm^{-1}) frequency ground as well as excited state modes of the AT and 13C isomers of ASR. On the one hand, the results illustrate a strong correlation between the shortening of the excited state lifetime and increase in ground state HOOP activity, which is interpreted as the evidence of pre-distortion. A number of experimental and theoretical evidences indicated that pre-distortion inside the retinal pocket to be a potential reason behind the accelerated kinetics, which fits to our findings. On the other hand, low frequency torsional mode remain practically unaffected after the point mutation. Therefore, we conclude that localized change in electrostatic interaction by a point mutation can cause subtle distortion of retinal geometry which may lead to an accelerated isomerization kinetics but does not affect the delocalized torsional modes.

Chapter 7

Effect of Truncation of Cytoplasmic Domain on the Ultrafast Photocycle of Anabaena Sensory Rhodopsin[3]

In the last chapter, the importance of the amino acid residues (inside the retinal protein pocket) in the context of the retinal photochemical dynamics has been elucidated. This chapter focuses to study the role of C-terminal extended part (final 32 amino acid residues of the helix) of the protein chain, which is far away (~19 Å) from the retinal pocket and embedded into cytoplasmic region of the bacterial cell.[50, 174] The truncation of the cytoplasmic domain has been experimentally observed to improve the expression level and also to favor the crystallization.[175] Therefore, it would be helpful for the biological researchers to use the truncated retinal protein instead of the full-length wildtype form if its biological function remains intact after the truncation. In this regard, early studies showed that the truncation or modification of the C-terminal extension does not affect the functions in haloarchaeal proton pumping bacteriorhodopsin or sensory rhodopsin I and II.[176-177] In contrast, recent experiments illustrated that this cytoplasmic 'tail' plays a significant role in controlling its biological activities happened in longer (~ms) timescale.[174, 178] In particular, for Anabaena Sensory Rhodopsin (ASR), the vectoriality of proton movement during Schiff base deprotonation had been found to be controlled by the cytoplasmic tail.[174, 178] For all retinal proteins the deprotonation of retinal protonated Schiff base (RPSB) is triggered by its sub-ps photochemical dynamics, which converts the RPSB to a blue shifted M intermediate and the ejected proton is transferred from inside of the cell towards the cytoplasmic region.[54] The truncation of this tail

---

[3] This chapter includes a part of the contents (e.g. data, figures, text) used in the manuscript: *"Influence of cytoplasmic domain on the ultrafast photocycle of Anabaena Sensory Rhodopsin."* P. P. Roy, Y. Kato, D. Agathangelou, H. Kandori, J. Léonard, S. Haacke and T. Buckup, *in preparation.*

dramatically reverses the normal outward movement of the proton making ASR as an inward proton transporter.[174, 178-179] This raises the issue, whether the absence of this cytoplasmic tail of the protein chain also affects the ultrafast photocycle of the RPSB by altering the arrangements of the surrounded amino acid residues.

In this chapter, we compare the photochemical dynamics of ASR with (full-length wildtype) and without (truncated) the cytoplasmic tail of its opsin moiety by exploiting UV-Visible femtosecond transient absorption (TA) spectroscopy. Although this truncation does not affect the energetics of the electronic states like the mutation in Chapter 6, the formation of the primary photoproduct gets affected. Our results depict three major differences between the full-length wildtype and truncated forms of ASR: (i) The rise of the photo-product, particularly for all-*trans* isomer, is slightly faster (τ=710 fs) in the truncated form than that in the full length form (τ=800 fs); (ii) The K-photo-product spectra of the full length and truncated ASR are distinguishable; (iii) Dark adaptation kinetics is found to be slower (T= 152 vs 83 min) for the truncated ASR. All these differences has been speculated by a change in potential energy surface of the RPSB as consequence of an alteration of H-bonding network linked to Lys210, which is covalently bonded to the amino group of the RPSB.

7.1 Ground state isomeric ratio and absorption spectra

Isomeric ratio: As described in section 3.1, ASR binds two structurally distinguishable isomers (all-*trans*: AT and 13-*cis*: 13C) in its retinal cavity and the ratio of these two isomers can be tuned by changing the external light adaptation conditions. Under dark adapted (DA) condition, the ASR contain almost exclusively AT isomer, whereas a continuous irradiation with a light source of wavelength above 560 nm causes it to reach a light adapted (LA) photo-stationary equilibrium mixture between the two isomers (Figure 7.1). The isomeric content obtained by the HPLC analysis shows the same isomeric contents for the full-length and the truncated ASR under the DA as well as LA conditions (Figure 7.1).

Ground state spectra: The ground state spectrum of the 13C isomer is blue shifted compared to the AT isomer in the full-length ASR as depicted in section 4.1. Since the light adaptation causes an increase in the content of 13C isomers (Figure 7.1), the UV-Visible absorption spectrum under the LA condition gets shifted compared to that under the DA condition. The ground state absorption

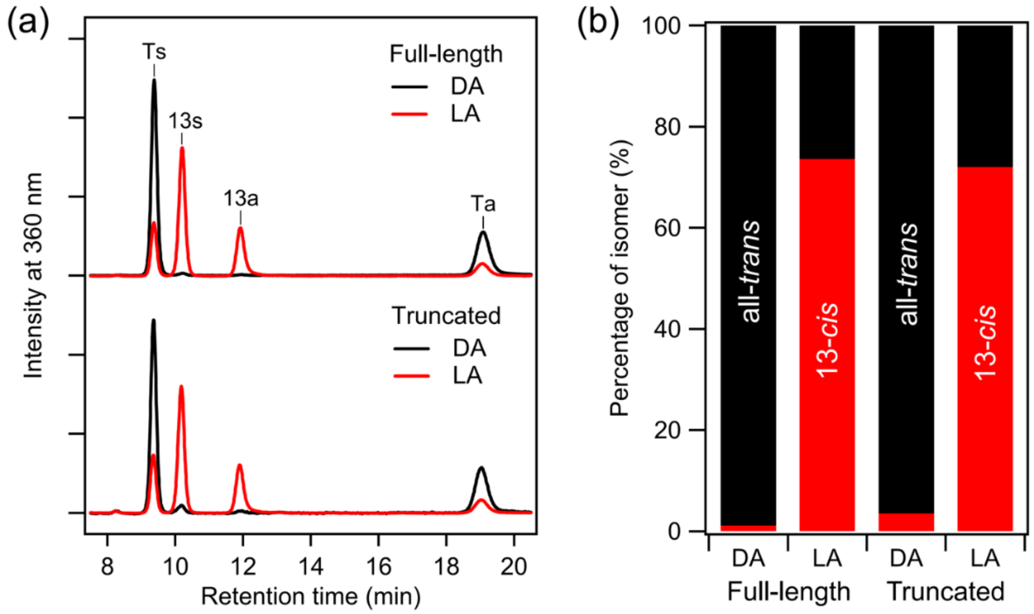

Figure 7.1: Retinal configuration of full-length and truncated ASR constructs. (a) HPLC pattern of retinal oxime extracted from ASR. (b) Percentage of all-*trans* and 13-*cis* retinal oxime. The composition of light adaptation sample were examined at 2 min after light illumination (>560 nm, 4 min).

spectra for the full-length and the truncated ASR, however, are found to be the same under the DA (Figure 7.2 (b)) as well as the LA (Figure 7.3 (c)) condition. The same isomeric content as well as

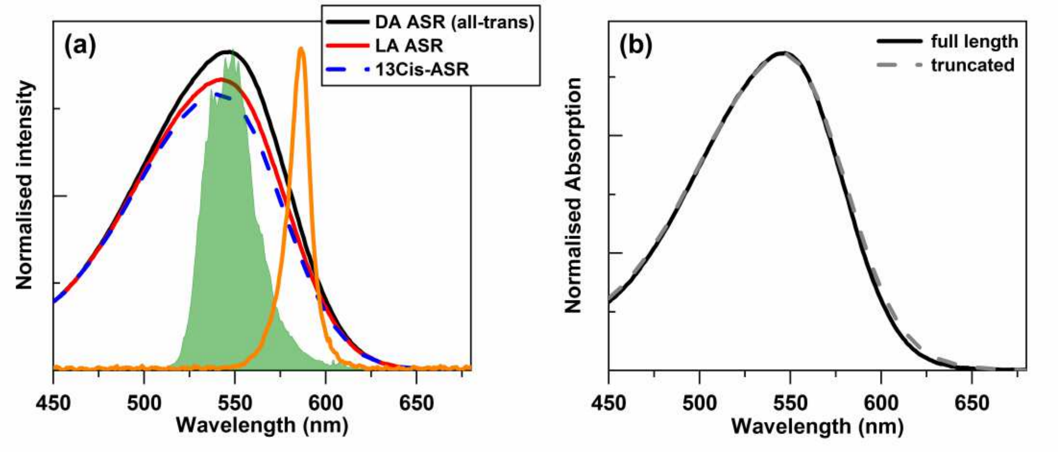

Figure 7.2: (a) Absorption spectra of full-length wildtype ASR under the DA (black line) and LA (red line) conditions. Spectrum of 13C-isomer (blue dotted line) calculated by taking linear combination of DA and LA spectrum using the known isomeric ratio. The orange curve represents the illumination spectrum used for light adaptation and filled green curve represents the excitation spectrum used for TA measurements. (b) Comparison of ground state absorption spectra of the full-length and truncated ASR under the DA condition.

similar ground state spectra of the full-length and truncated ASR under each condition infers that the truncation does not affect the $S_0 \rightarrow S_1$ energy gap in any of the isomer of the RPSB.

7.2 Comparison of dark adaptation kinetics

Keeping the LA ASR in dark allows the 13C isomer to return back to the AT conformation by a thermal relaxation. As a consequence, the ground state spectrum starts to get red shifted and increases in intensity, which is named as dark adaptation process. The difference absorption spectrum was measured up to 4 hours after the complete light adaptation to follow the dark adaptation kinetics. In spite of having similar changes in the spectral profile (Figure 7.3 (a) and (b)), the dark adaptation kinetics (Figure 7.3 (d)) are clearly different for the full-length and the truncated ASR. The full-length form (τ = 83 min) shows a 2-fold faster recovery than the truncated one (τ = 152 min). This means that the thermal relaxation from the 13C to the AT isomer gets slowed down in absence of the cytoplasmic domain.

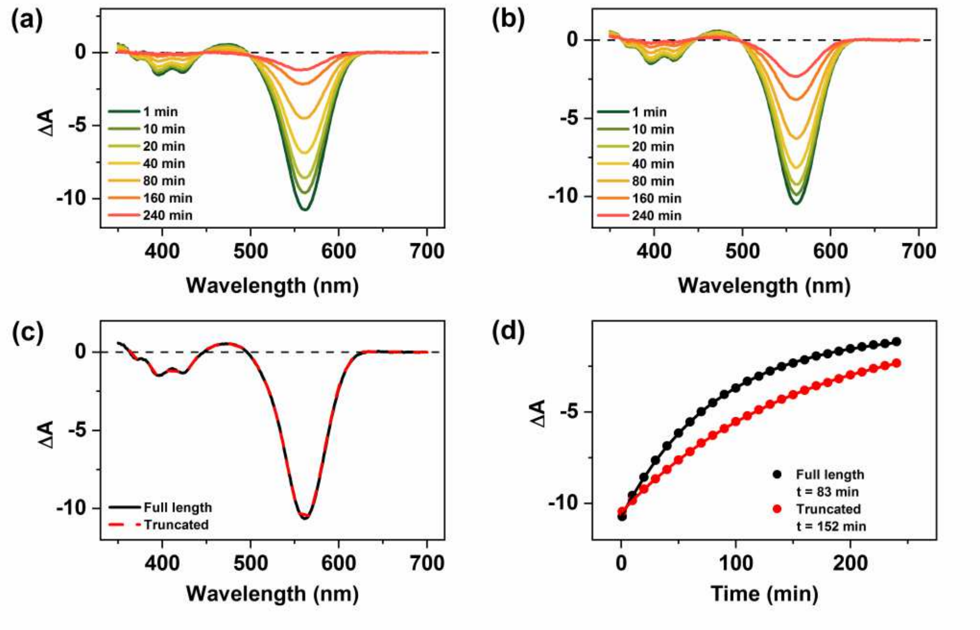

Figure 7.3: Dark adaptation at 25°C: Light minus dark difference absorption spectra of (a) full-length and (b) truncated ASR. The spectra were monitored continuously after light illumination (λ_{exc}>560 nm, 4 min). (c) Comparison of difference absorption spectrum of the full-length and the truncated ASR. (d) Dark adaptation kinetics: The difference absorption at 560 nm were plotted against time after the light illumination. The traces were fitted by a single exponential curve.

7.3 Transient absorption measurement

A set of TA measurements with an excitation spectrum centered at the maximum of the ground state absorption spectrum of ASR (Figure 7.2 (a)) was carried out to compare sub-10 ps dynamics of the full-length and truncated ASR under both DA and LA conditions (Figure 7.4). For each sample, three characteristic spectral bands of ASR such as, a ground state bleach (GSB) around 550 nm, a fast decaying blue shifted excited state absorption (ESA) around 450 nm and a long lived photo-induced absorption (PIA) around 620 nm, were observed (see section 4.2 for details). The truncation does not affect the overall spectral appearance (Figure 7.4), but makes the decay of each band slightly faster compared to the full-length form under both DA and LA conditions. In order to compare the isomer specific transients, a linear combination of the TA signal under the DA and LA conditions is taken (see section 3.3.3). Figure 7.5 shows a comparison of the transients for the full-length and truncated ASR at selected probing wavelengths 450 nm (ESA), 550 nm (GSB) and 620 nm (PIA): At each of these detection wavelengths, the pump-probe signal of the truncated

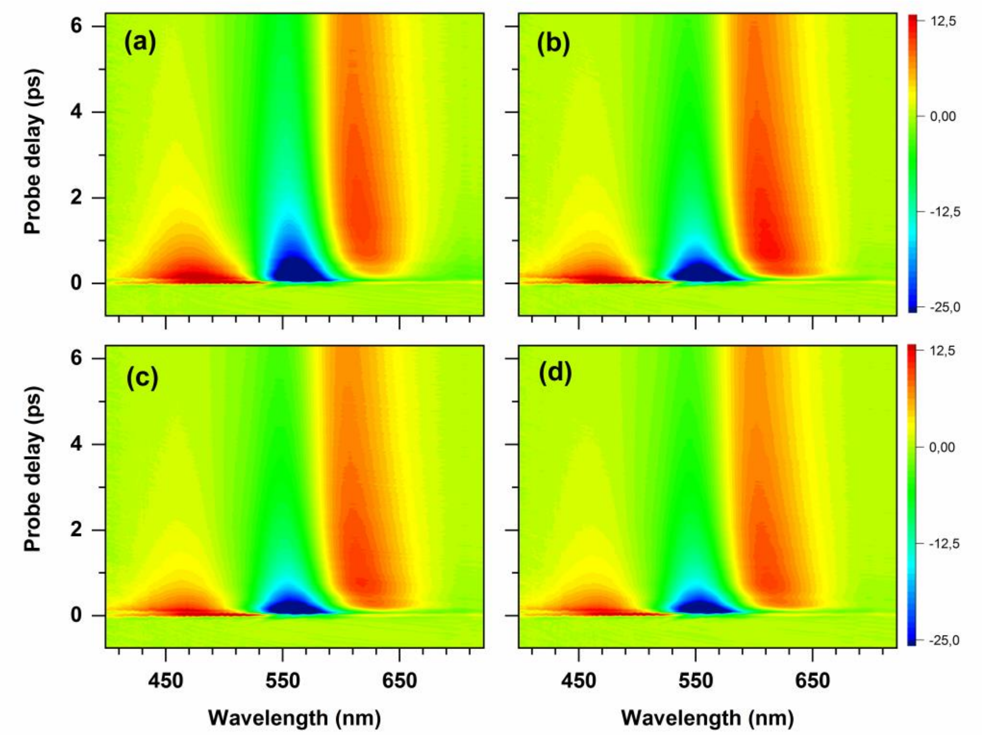

Figure 7.4: Transient absorption difference spectra of the full-length (a and c) and the truncated ASR (b and d) measured under the DA (a and b) and LA (c and d) conditions. The 2D map shows the spectro-temporal evolution of difference optical density (ΔOD).

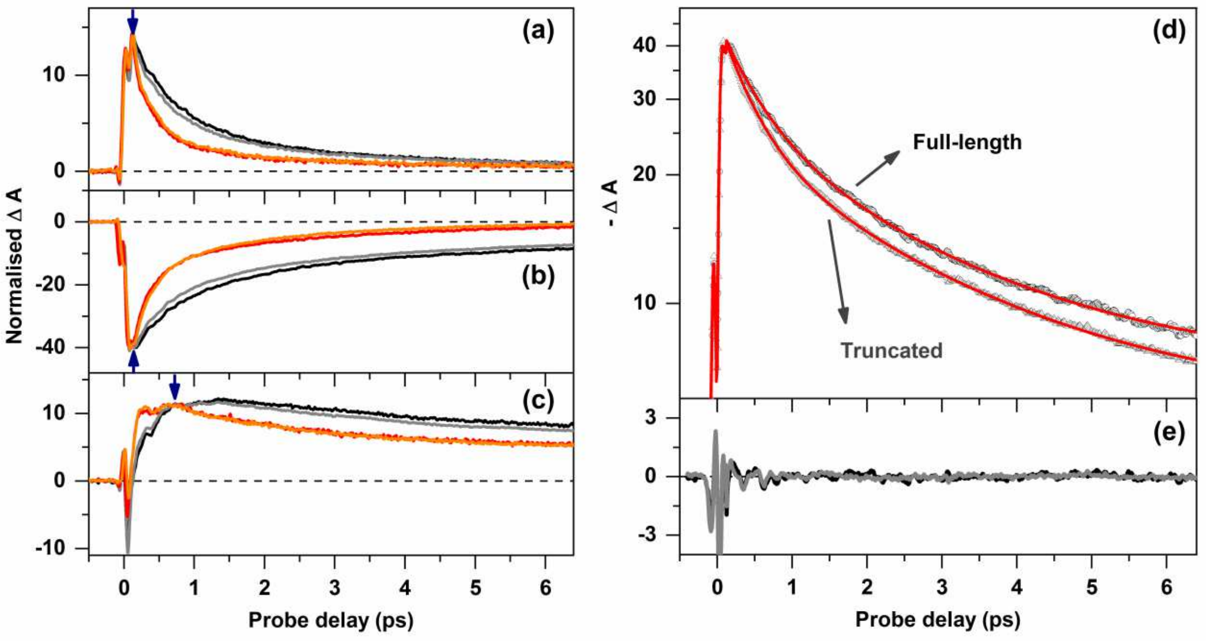

Figure 7.5: Comparison of transients of the AT (black and grey) and the 13C-isomer (red and orange) of the full-length (black and red) and truncated (grey and orange) ASR at different probing wavelengths (a) 450 nm, (b) 550 nm and (c) 620 nm averaged over 10 nm spectral window. Each set of the transients were normalized with respect to transient of full-length ASR under DA condition at the delay specified by vertical arrow in each graph. (d) Exemplary fitting of transients of the full-length and truncated forms of the AT ASR at 550 nm in logarithm scale. The open circles represent experimental data and red solid curves represent fitting with a bi-exponential double decay kinetic model along with the coherent artefact. Corresponding residuals obtained by fitting are shown in (e).

form, especially for the AT isomer, shows relatively faster decay compared to the full-length ASR. This is clearly illustrated by a careful fitting of the transient with a bi-exponential model and the results these fitting for the transients at different probing wavelengths for each sample are summarized and compared in Table 7.1. For example, at a probing wavelength of 550 nm, the signal for the AT isomer of the full-length ASR decays with a time constant (τ_1) of 540 ±8 fs, whereas for the truncated form it decays with 440 ±5 fs (Figure 7.5 (d)). The decay for the 13C isomer is also affected by the truncation but in a smaller extent: While the FL 13C decays at e.g. 550 nm with 270 ±8 fs, the truncated one decays faster with a time constant of 240 ±10 fs. The observed effect of the truncation on the kinetics is, however, much smaller compared to the effect of the mutation shown in the last chapter. Nevertheless, this small difference in the isomerization kinetics between the full-length and truncated ASR was consistent for all independent TA measurement performed on different days. In addition, a constrained bi-exponential fitting of the

Table 7.1: Time constants obtained by bi-exponential fitting of the transients. The transient were taken at different probing wavelengths for the DA, LA and extracted pure-13C isomer of the full-length (FL) and truncated (Tru) ASR. The transients at 450 and 550 nm were fitted with a bi-exponential decay model (τ_{dec1} and τ_{dec2}), whereas the transients at 620 nm were fitted with a bi-exponential one rise-one decay model (τ_{rise} and τ_{dec}).

Sample		**λ_{Pr}=450 nm**		**λ_{Pr}=550 nm**		**λ_{Pr}=620 nm**	
		τ_{dec1}	τ_{dec2}	τ_{dec1}	τ_{dec2}	τ_{rise}	τ_{dec}
DA/ AT	FL	510 ±5 fs	2.0 ±0.1 ps	540 ±8fs	2.6 ±0.1 ps	260 ±7fs	5.0 ±0.2 ps
	Tru	430 ±8 fs	1.7 ±0.1 ps	440 ±5 fs	2.5 ±0.1 ps	200 ±5fs	3.8 ±0.1 ps
LA	FL	260 ±10 fs	1.3 ±0.1 ps	280 ±5 fs	2.2 ±0.1 ps	130 ±10 fs	3.2 ±0.1 ps
	Tru	240 ±7 fs	1.3±0.1 ps	270 ±8 fs	2.0 ±0.1 ps	110 ±5 fs	3.0 ±0.1 ps
13C	FL	220 ±7 fs	1.2 ±0.1 ps	270 ±8 fs	2.1 ±0.1 ps	100 ±8 fs	2.2 ±0.1 ps
	Tru	200 ±10 fs	1.1 ±0.1 ps	240 ±10 fs	1.9 ±0.1 ps	80 ±15 fs	2.0 ±0.1 ps

transients were carried out for the truncated ASR (not shown here): the time constants, obtained by fitting the transient of the full-length ASR at corresponding probing wavelengths, were kept constant; only the amplitude were varied. It exhibits that the relative amplitude of faster decaying component compared to slower decaying component increases from the full-length to truncated ASR. This further confirms the difference in isomerization rate between the full-length and truncated ASR, especially for the AT isomer.

7.4 Coherent vibrational dynamics

In addition to the population kinetics, it was possible to extract vibrational features contributing on top of the population kinetics in the TA signal. The residuals obtained after the bi-exponential fitting of initial dynamics at blue (530 nm) and red detuned probing wavelength (640 nm) of the GSB band are depicted in Figure 7.6. It shows strongly damped oscillatory features (~1 mOD) with a period of 550 ±50 fs (~60±5 cm^{-1}) for both isomers, which is beyond the noise level (<0.1 mOD). Furthermore, there occurs a π phase shift of this periodic modulation from blue (530 nm) to red

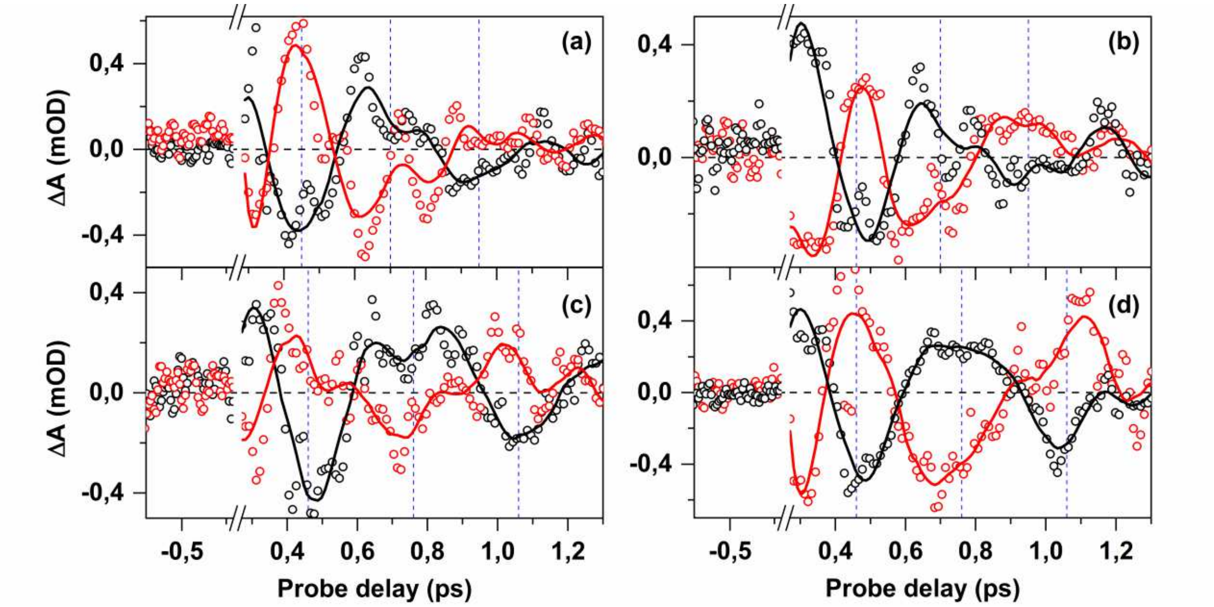

Figure 7.6: The residuals obtained after bi-exponential fitting of initial (1.5 ps) dynamics. The residuals are shown for the AT (a and b) and 13C (c and d) isomers of the full-length (a and c) and truncated (b and d) at two different probing wavelengths: 530 nm (black dot) and 640 nm (red dots). The solid lines are average of 10 points, drawn as the guide of eyes.

(640 nm) detuned probing wavelength. Similar period of oscillation was observed for each isomer of both full-length and truncated ASR, at least within our experimental error bar. Thus, the truncation of the cytoplasmic domain does not affect the low frequency (<100 cm^{-1}) oscillation.

7.5 Discussion

7.5.1 Electronic dynamics

The similar isomeric ratio and ground state absorption spectra for the full-length and truncated ASR shows that the truncation of the ‘cytoplasmic tail’ does not affect the relative energy separation between the S_0 and S_1 electronic states either of the AT or 13C isomers of the RPSB. The effect of the truncation appears on the ultrafast dynamics, especially for the AT isomer.

The first truncation effect appears in the sub-picosecond time scale (Figure 7.4) and has been clearly resolved by bi-exponential fitting (Table 7.1). This shows that overall kinetics gets

Table 7.2: The parameters obtained by global fitting of the TA data sets for the AT and 13C isomers of the full-length (FL) and truncated (Tru) ASR by a five component sequential model, as described in section 4.4: $A \xrightarrow{t_1} B \xrightarrow{t_2} I \xrightarrow{t_3} J \xrightarrow{t_4} K \xrightarrow{t_5}$

Sample		**t_1**	**t_2**	**t_3**	**t_4**	**t_5**
AT	FL	40 fs (±10)	280 fs (±30)	800 fs (±20)	3.1 ps (±0.3)	Inf
	Tru	35 fs (±10)	240 fs (±20)	710 fs (±30)	3.1 ps (±0.2)	Inf
13C	FL	30 fs (±10)	180 fs (±30)	470 fs (±30)	3.1 ps (±0.2)	Inf
	Tru	25 fs (±10)	160 fs (±20)	410 fs (±20)	3.0 ps (±0.3)	Inf

accelerated due to the truncation, majorly for the AT isomer. Further, a constrained bi-exponential fitting reveals that the truncation affects the relative amplitudes of fast and slow decaying components. In addition, a global target analysis (Table 7.2) with the same kinetic model, as used for the full-length wildtype ASR in section 4.4, shows especially the decay of the third species (t_3) is significantly accelerated in the truncated form for both the isomers. Since the decay of the third species (i.e. rise of the fourth species) has been associated with the kinetics of the primary photoproduct (J-intermediate) formation, the changes observed for t_3 hints at a modification of the dynamics close to the conical intersection because of the truncation.

The second effect of the truncation takes place in a much longer time (>100 ps) scale. The time constant for appearance of 'K'-and 'L'-product in the retinal cycle is <5 ps and ~μS, respectively. So, at 100 ps delay, the population has already relaxed into the 'K'-product and the transient absorption signal should contain only the difference spectrum of the pure ground state and the 'K'-product. Since the ground state absorption of the full-length and truncated ASR has been shown to be the same previously (Figure 7.2 (b) and Figure 7.3 (c)), the difference spectrum at 100 ps for the full length and truncated form of ASR is expected to spectrally overlap only if the absorption of the 'K'-product appears to be the same for both forms. Figure 7.7 reveals that the spectra of the full-length and truncated ASR overlap well at blue detuned wavelengths (<520nm), but a striking difference appears at detection wavelength above 550 nm, particularly around 600 nm. In DA condition (Figure 7.7 (a)), the spectrum for Tru ASR is blue shifted by about 10 nm compared to FL ASR. In LA condition (Figure 7.7 (b)), the truncation does not cause spectral shift

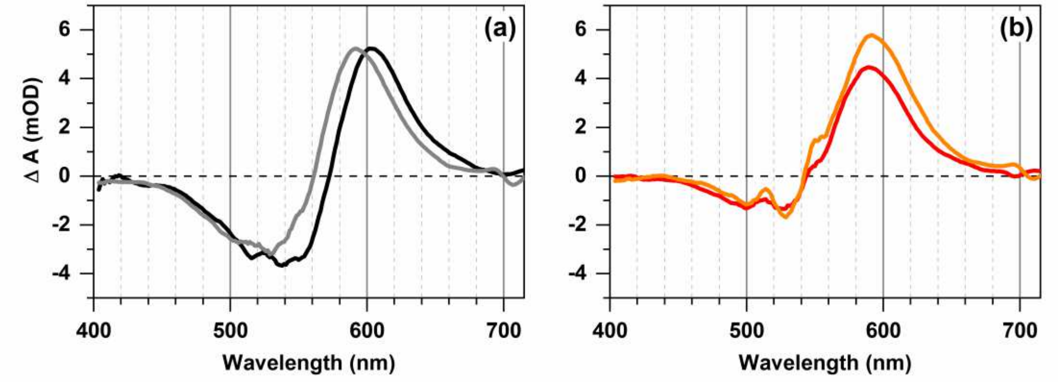

Figure 7.7: Comparison of the transient difference absorption spectra at about pump-probe delay 100 ps (averaged over ±5 ps) under (a) DA and (b) LA conditions for the full-length (black and red) and truncated (grey and orange) ASR.

but increases the amplitude of TA signal by ~1.3 times. This provides a clear experimental evidence that distinct 'K'-photoproducts are present in the truncated form compared to the wild type full-length ASR pigment.

The third effect of truncation appears in the dark adaptation kinetics. In particular, the dark adaptation gets almost two folds faster for the truncated ASR compared to the full-length form. Generally the thermal relaxation of one structural isomer of the RPSB to another during the dark adaptation of the proteins are quite well known phenomena. A few photo-calorimetry studies showed that the 13C isomer of the RPSB poses 40-50 kJ/mol higher enthalpy compared to the AT isomer.[86, 180] The thermal isomerization has been reported for the 13C isomer in bacteriorhodopsin to return back to the AT form at a rate 100 S^{-1} at 20°C.[181] In contrast, thermal relaxation of the 13C isomer in solution is extremely slow. This, indicates protein constructions plays a significant role in destabilizing the 13C isomer and catalyzing the rate limiting return to the AT isomeric form. Therefore, our experimental observation of acceleration in the thermal relaxation kinetics of the 13C isomer of the RPSB in the truncated ASR strongly suggests a change in the protein arrangements as a consequence the C-domain truncation.

7.5.2 Vibrational dynamics

In contrast to the observed differences in the electronic dynamics, a damped periodic oscillation with a frequency of 50-70 cm^{-1} were observed for both full-length and truncated ASR. Similar kind of oscillatory features with a frequency of 50-70 cm^{-1} were reported for visual Rhodopsin

(11-cis).[29] Also for ASR, an oscillation with a period of 500 fs (~65 cm-1) was observed by Cheminal *et al.*[90] Furthermore, this oscillation reverses its phase from the blue to red edge of the probing window. It gives a strong indication that the observed oscillation are the signatures for motion of a coherently excited wave packet. This is because the phase of the excited wave packet gets reversed, when it moves from one end of the potential energy surface to other end. As a consequence, the oscillatory signatures, which appear over the electronic signal, shows a π phase shift around the maximum (corresponds to potential minima) of electronic signal of that particular state. Therefore, it is also possible to assign the oscillatory mode to the particular electronic state manifold knowing the of phase change over the probing wavelength and matching it with the maxima of the electronic signal of a particular state. In case of ASR, it not trivial to assign this low frequency (~60 cm^{-1}) oscillation to a particular electronic state as the electronic signal of the ground and excited states overlap in this wavelength range (430 to 640 nm) where phase reversal has been detected. However, the oscillation seems to survive about 1 ps (Figure 7.6), which is longer than the reported excited lifetime of both AT (700 fs) and 13C (170 fs) isomer. Hence, it is less likely to be originated from the excited state; rather could be assigned as the ground state signature. This means it survives even after passing the passing the conical intersection for both AT and 13C isomer. Most importantly, it appears consistently in both full-length and truncated ASR for each isomer (Figure 7.6). This indicates that truncation does not bring any significant change in ground state vibrational dynamics (period of 550 fs).

In summary, truncation affects the thermal relaxation kinetics from 13C to AT as well as J-photoproduct formation dynamics without altering the ground state signature. This effect of truncation of the cytoplasmic part on ultrafast photo-cycle can be rationalized by the change in protein environment close to retinal pocket. Cytoplasmic opsin part of ASR are known to remain in markedly hydrophilic environment compared to other MRP's like bacteriorhodopsin and other sensory rhodopsin.[50] It has been found in the past that there is an almost continuous hydrogen bond network including two carboxylic acids, two serine residues, one threonine residue, one glutamine residue and four water molecules, which connects cytoplasmic domain to Lys^{210} residue, covalently bonded to amino group of retinal chromophore.[50, 179, 182] Truncation of cytoplasmic domain disrupts aforementioned hydrogen bond network. This brings a slight change in potential energy surface which possibly influences the retinal isomerization, leading to the formation of distinct

‘K’-photoproduct on longer time scale and also changes the pathway of thermal relaxation of 13C-isomer to AT-conformation during dark adaptation.

7.6 Conclusion

In this chapter, we studied the role of cytoplasmic ‘tail’ on the primary process of retinal photo-chemistry. Our results show truncation does not affect the ground state but alters the product formation. In summary, the full-length and truncated ASR differ in three aspects: the dark adaptation kinetics, the rate of ‘J’-intermediate formation and the K-photoproduct spectrum. All these facts point towards the conclusion that the long-lived species i.e. ‘K’-product, which is formed after the completion of the isomerization of active $C_{13}=C_{14}$ bond of retinal chromophore in the truncated ASR, is different from that formed in the wild type full-length ASR. This has been speculated by change in minimum potential energy pathway due to alteration of hydrogen bond network linked to Lys^{210} residue, which is directly bonded to the chromophore. In conclusion, it reveals not only the protein environment close to chromophore but also the amino acid residues far from retinal pocket can play a significant role on primary process of retinal photo-chemistry.

Chapter 8

Conclusion and Outlook

8.1 Conclusion

In this thesis, the photo-induced isomerization dynamics of retinal has been successfully investigated with the help of femtosecond time-resolved spectroscopic techniques. A special attention was given to monitor the transient structural changes of retinal protonated Schiff base (RPSB) inside the retinal protein. For that purpose, multidimensional coherent vibrational spectroscopic methods like pump-degenerate four wave mixing (pump-DFWM) and pump-impulsive vibrational spectroscopy (pump-IVS) were employed. Experimental results obtained by these techniques revealed the vibrational dynamics of the protein bound RPSB in the sub-ps timescale. This information on the vibrational dynamics complemented that on electronic dynamics revealed by the transient absorption (TA) methods. The following paragraphs summarize the main findings of this thesis.

In general, the ground state structure of the RPSB and the surrounding protein constructions are known to be the most crucial elements in the context of retinal photochemistry. One of the main goals of this thesis was to survey both of these factors individually. For that purpose, Anabaena Sensory Rhodopsin (ASR) was chosen as a working system as it comprises both all-*trans* (AT) and 13-*cis* (13C) isomers in its photocycle and therefore, providing a unique test ground to single out the individual effect of the ground state configuration of the RPSB on its reaction dynamics. Our experimental results showed that both electronic and vibrational dynamics are widely distinct for the AT and 13C isomers of the RPSB. In particular, a comparative TA study exhibited more than five folds acceleration of the reaction rate from the AT to the 13C isomer (Chapter 4). Furthermore, the evolution of the vibrational modes were mapped by (pump-) DFWM and (pump-) IVS techniques (Chapter 5). It depicted transient frequency shifts for the localized modes (e.g. C=C, C-C stretching, CH_3 rocking) within the excited state lifetime of each isomers. One of the major findings was a large difference in the timescales of these frequency shifts for the AT and 13C isomers. While it takes more than 200 fs after the photoexcitation for the former, it occurs instantaneously (<30 fs) for the 13C isomer. These frequency shifts were interpreted as an evidence of reduction in effective π-conjugation length as a consequence of torsion around the isomerizing C=C bond of the RPSB during the isomerization reaction. This implicated that AT isomer takes longer time to isomerize than the 13C isomer. These interpretations were in line with a quantum computational trajectory calculation reported earlier,[91] which predicted a barrier along the excited state trajectory of the AT isomer. This energy barrier between the Franck-Condon region and the conical intersection (CI) leads to deceleration of the isomerization reaction for the AT isomer. In contrast, the excited trajectory of the 13C isomer was barrierless, which explains its faster dynamics.

Another major finding of this thesis comes from the comparison of ground state Raman spectra of the AT and 13C isomers, which showed a stronger hydrogen-out-of-plane (HOOP) activity for the latter compared to the former (Chapter 5). For the retinal systems, the HOOP activity in the Raman spectra of any RPSB has been considered as an indication of its structural distortion.[84, 141, 146] Therefore, our results indicated a strong distortion of the ground state structure for the 13C isomer compared to the AT isomer of the RPSB inside the retinal pocket of ASR. The pre-distortion of the ground state retinal structure was reported to have a major influence in the acceleration of the reaction dynamics for the retinal proteins like visual-Rhodopsin.[49, 82, 84, 141-144] This is because the photo-excitation of a pre-distorted isomer causes the excited wave packet to appear relatively closer to the isomerized photoproduct potential surface along the reactive reaction coordinate than an isomer, which is completely planar in the ground state. The experimental observation of this pre-distortion in the ground state does not contradict, however, the theoretical prediction of a barrier in the excited state. Both may be connected and be the cause for the different excited state lifetimes in AT and 13C isomer. For example, if there is an energy barrier along the reactive coordinate, a pre-distortion may help to avoid that barrier, since the photoexcitation of the pre-distorted RPSB isomer might cause the wave packet to be excited after such a barrier in the excited potential and, hence, leading to shorter lifetimes.

Another important aspect of this thesis was the investigation of the influence of the protein cage surrounding the RPSB chromophore in guiding the isomerization reaction (Chapter 6-7). In that purpose, two different point mutations in the protein chain of the ASR was performed (V112N and L83Q) (Chapter 6). In each case, a single non-polar amino acid residues in vicinity of the RPSB inside the retinal pocket, was replaced by a polar one. The mutations have a strong effect on the photo-isomerization dynamics of the RPSB. In particular, they cause more than three folds acceleration of the isomerization reaction time for the AT isomer, whereas mutations have only a minor effect on the dynamics of the 13C isomer. Same trend was observed for the frequency shifts of the C=C stretching modes during the photo-isomerization reaction. This asymmetric effect of mutation on the dynamics of the AT and 13C isomers of the RPSB strongly suggests that the electrostatic interaction exerted by the same protein cage on two different isomers must be widely different.

The molecular origin of the observed difference in isomerization dynamics between the WT and the mutants were found by comparing the ground state spectra of the WT ASR and its mutants (Chapter 6). It showed a strong correlation between the amplitude of the HOOP activity and the isomerization reaction time of corresponding sample. This indicated that the observed acceleration of the reaction rate for the AT isomer in the mutants could be caused by a pre-distortion of the ground state retinal structure, similar to 13C isomer of the WT. Hence, the major conclusion drawn from all these studies is that the electrostatic interaction between the RPSB and the surrounding amino acid residues inside the retinal pocket governs the structural changes of the RPSB during its isomerization reaction. This interaction can be modified either by changing the ground state retinal structure or by perturbing the opsin constructions. In both cases, it influences the reaction dynamics.

The role of the protein chain embedded in the cytoplasmic region, which are far from the retinal pocket, were also investigated (Chapter 7). Truncation of the cytoplasmic tail showed a small acceleration for the formation of primary photoproduct, especially for the AT isomer. Major changes were observed in the longer (>100 ps) time scale. In particular, the photo-product spectra and dark adaptation kinetics were found to be widely distinct for the truncated ASR in comparison to the full length WT ASR. Observed changes were interpreted as a consequence of alternation in a long H-bond network starting from the amino group of the retinal chromophore and extended up to the cytoplasmic tail of the protein chain in ASR. These studies depicted that not only the amino acid residues in vicinity of the RPSB but also those far apart (~20A) from the RPSB can play a significant role in isomerization reaction, especially for the long time (>100 ps) relaxation kinetics of the photo-product. This is line with the recent time resolved x-ray crystallography study of bacterio-Rhodopsin, which depicted synchronized movement of the amino acid residue far apart from the retinal pocket.[31]

Another cornerstone of the present work was to explore the activation mechanism of individual vibrational mode of the RPSB. First, a complete characterization each vibrational mode to specific electronic state was done on the basis of its dephasing rate and excitation wavelength dependence. The ground state Raman spectrum was found to cover mostly the high frequency (>1000 cm^{-1}) modes, whereas the excited Raman spectra contained both high (>1000 cm^{-1}) and low frequency (<400 cm^{-1}) modes. In order to explore the activation mechanism of these excited state modes, the evolution of the transient Raman spectra was mapped by impulsive vibrational spectroscopic methods. It exhibited a distinct activation mechanism for the high frequency (>1000 cm^{-1}) localized and the low frequency (<400 cm^{-1}) torsional modes. The former modes were found to be Franck Condon active, while the latter modes were mostly activated indirectly by an energy flow from the localized modes via an internal vibrational energy re-distribution (IVR). It was evident from the time dependent Raman transition amplitude of the low frequency modes.

The observation of activation of one class of mode with other supports “two-states-two-modes” model[27, 104] (see Figure 1.3 (b)). In particular, this model states that there are two classes of coupled vibrational motions, named as tuning and coupling modes, which controls the isomerization reaction. Among these two classes, only the latter represents the reactive coordinate of the isomerization reaction. In all our experimental results, the high frequency (>1000 cm^{-1}) modes were found to be the tuning modes, which change their frequencies from the ground to excited state but don’t actively participate in the reaction (Chapter 5). In contrast, all low frequency (<400 cm^{-1}) torsional modes were found to be activated indirectly, which characterizes them as the coupling modes. However, it remain unaffected, even when a significant acceleration of the isomerization kinetics is reported (Chapter 6). This may initially puzzle since as a reactive coordinate, one would expect changes in its frequency and/or amplitude due to mutation keeping in mind the drastic effect of the mutation on the excited state lifetime of the RPSB. However, these low frequency modes are very delocalized modes, which may not be so strongly influenced by the point mutation as the localized HOOP and other high frequency modes.

Overall, the reported experimental results in this thesis shed new light on the retinal photochemistry. It revealed that the protein construction plays the predominant role for the retinal photo-isomerization mechanism. Specifically, the residues in vicinity of the bound RPSB controls the initial (<ps) events of the retinal isomerization, while those residue far apart from the RPSB play a predominant role in the long time (>100 ps) relaxation kinetics of the photo-product. Moreover, the present work elucidates the intricate relationship between the electronic and vibrational dynamics of the RPSB. In particular, it illustrates that small perturbations of the electrostatic environment lead to strong changes in the vibrational dynamics as well as in the reaction dynamics. This finding will inspire technological advancement to develop bio-mimic light harvesting compounds with faster responsive properties.[42, 48, 172, 183]

8.2 Outlook

The presented results raised several new challenges in the photochemistry of retinal. Firstly, in all coherent vibrational spectroscopic measurements presented in this thesis, the dynamics of the RPSB has been probed in the visible spectral region, where both the excited spectra overlap with the ground state spectral. It was shown that in some conditions this may lead to an optical signal contain a mixing of substantial fraction of non-resonant ground state contribution along with a major contribution from the excited state. This restricts the quantitative evaluation of the excited state vibrational spectra. The only spectral range devoid of any ground state dynamics is the near infrared (NIR) region (950-1400 nm), where a pure stimulated emission band appears without any overlap with the ground state bleach band for most of the retinal proteins.[98, 184] Thus, a pump-DFWM measurement with a visible actinic pulse and NIR DFWM pulses, would help to evaluate the pure excited state vibrational spectra as well as to track its evolution. In this regard, a non-collinear optical parametric amplifier (nc-OPA), which can derive an ultrashort pulse in the NIR region, has been recently developed in our lab. This opens up a possibility in the future to evaluate the pure excited vibration spectra of ASR as well as other retinal proteins.

Secondly, the comparative studies of the WT and two different point mutants, presented in this thesis, has depicted the role of two individual amino acid residues on the isomerization reaction. It lacks, however, the broader picture about the role of whole protein environment. In order to address this open question, one needs to follow the dynamics of the protein residues and the bound RPSB inside the WT protein all together. One possibility is the tracking of this sub-ps movement of the moieties by femtosecond transient IR spectroscopy.[137, 185] Infrared spectroscopies allow to follow the transient changes in the IR spectra of the structure changes of all molecules present in the protein. Alternatively, a direct recording of the atomic motion is also possible by emerging transient x-ray crystallography methods. A recent time-resolved x-ray crystallographic study on bacteriorhodopsin captured the movement of the RPSB as well as the surrounding amino acid residues from 100 fs to 2 ms after the photo-excitation.[31, 186] Similar studies on ASR can depict the role played by each surrounding amino acid residue and water molecule to channelize the reaction for both the AT and 13C isomers of the RPSB. It would point out the amino acid residue responsible for the differential interaction with two isomers.

Thirdly, although our studies showed an evidence for the internal energy flow from the high to low frequency modes, it could not quantitatively estimate the time scale at which this transfer of energy take place. In addition, it was not clear what are the factors determining this coupling strength. One possibility to address this question is to employ 2D Raman spectroscopic measurements.[187-189] This follows the same experimental setup as presented for the pump-DFWM technique, which widens the prospect to study the 2D Raman with the same experimental setup in our lab. In resultant 2D Raman spectrum, the appearance of cross peaks would be considered an evidence of coupling and the asymmetry of these cross peaks would provide an estimation of the time required for the IVR process.

Bibliography

1. Fork, R. L.; Greene, B. I.; Shank, C. V., Genertion of optical pulses shorter than 0.1 psec by colliding pulse mode locking. *Appl. Phys. Lett.* **1981,** *38*, 671-672.

2. Rose, T. S.; Rosker, M. J.; Zwail, A. H., Femtosecond real time observation of wave packet oscilltions (resonance) in dissociation reactions. *J. Chem. Phys.* **1988,** *88*, 6672-6673.

3. Pedersen, S.; Herek, J. L.; Zewail, A. H., The Validity of the Diradical Hypothesis - Direct Femtosecond Studies of the Transition-State Structures. *Science* **1994,** *266*, 1359-1364.

4. Zwail, A. H., Femtochemistry. Past, present, and future. *Pure. Appl. Chem.* **2000,** *72*, 2219-2231.

5. Zwail, A. H., Femtochemistry: Atomic-scale dynamics of the chemical bond. *J. Phys. Chem. A* **2000,** *104*, 5660-5694.

6. Motzkus, M.; Pedersen, S.; Zewail, A. H., Femtosecond Real-Time Probing of Reactions. 19. Nonlinear (DFWM) Techniques for Probing Transition States of Uni- and Bimolecular Reactions. *J. Phys. Chem. A* **1996,** *100*, 5620-5633.

7. Kiefer, W.; Materny, A.; Schmitt, M., Femtosecond time-resolved spectroscopy of elementary molecular dynamics. *Naturwissenschaften* **2002,** *89*, 250-258.

8. Fujiyoshi, S.; Takeuchi, S.; Tahara, T., Time-Resolved Impulsive Stimulated Raman Scattering from Excited-State Polyatomic Molecules in Solution. *J. Phys. Chem. A* **2003,** *107*, 494-500.

9. Volkmer, A., Vibrational imaging and microspectroscopies based on coherent anti-Stokes Raman scattering microscopy. *J. Phys. D: Appl. Phys.* **2005,** *38*, R59-R81.

10. Kukura, P.; Yoon, S.; Mathies, R. A., Femtosecond stimulated Raman spectroscopy. *Analytical Chemistry* **2006,** *1*, 5953-5959.

11. Hauer, J.; Buckup, T.; Motzkus, M., Pump-Degenerate Four Wave Mixing as a Technique for Analyzing Structural and Electronic Evolution: Multidimensional Time-Resolved Dynamics near a Conical Intersection. *J. Phys. Chem. A* **2007,** *111*, 10517-10529.

12. Kukura, P.; McCamant, D.; Mathies, R. A., Femtosecond Stimulated Raman Spectroscopy. *Annu. Rev. Phys. Chem.* **2007,** *58*, 461-488.

13. Berera, R.; Grondelle, R. v.; Kennis, J. T. M., Ultrafast transient absorption spectroscopy: principles and application to photosynthetic systems. *Photosynth. Res.* **2009,** *101*, 105-118.

14. Ruckebusch, C.; Sliwaa, M.; Pernotb, P.; Juan, A. d.; Taulerd, R., Comprehensive data analysis of femtosecond transient absorption spectra: A review. *J. Photo. Chem. Photo. Biol. C* **2012,** *13*, 1-27.

15. Murchie, E. H.; Lawson, T., Chlorophyll fluorescence analysis: a guide to good practice and understanding some new applications. *J. Exp. Bot.* **2013,** *64*, 3983-3998.

16. Namboodiri, M.; Khan, T.; Karki, K.; Kazemi, M. M.; Bom, S.; Flachenecker, G.; Namboodiri, V.; Materny, A., Nonlinear spectroscopy in the near-field: time resolved spectroscopy and subwavelength resolution non-invasive imaging. *Nanophotonics* **2014,** *3*, 61-73.

17. Wende, T.; Liebel, M.; Schnedermann, C.; Pethick, R. J.; Kukura, P., Population-controlled Impulsive Vibrational Spectroscopy: background- and baseline-Free Raman spectroscopy of excited electronic states. *J. Phys. Chem. A* **2014,** *118*, 9976−9984.

18. Buckup, T.; Motzkus, M., Multidimensional time-resolved spectroscopy of vibrational coherence in biopolyenes. *Annu. Rev. Phys. Chem.* **2015,** *65*, 39–57.

19. Chosrowjan, H.; Taniguchi, S.; Tanaka, F., Ultrafast fluorescence upconversion technique and its applications to proteins. *FEBS Journal* **2015,** *282*, 3003-3015.

20. Liebel, M.; Schnedermann, C.; Wende, T.; Kukura, P., Principles and Applications of Broadband Impulsive Vibrational Spectroscopy. *J. Phys. Chem. A* **2015,** *119*, 9506-9517.

21. Kuramochi, H.; Takeuchi, S.; Tahara, T., Femtosecond time-resolved impulsive stimulated Raman spectroscopy using sub-7-fs pulses: Apparatus and applications. *Rev. Sci. Instrum.* **2016,** *87*, 1-9.

22. Chen, H.-Y.; Lee, I.-R.; Cheng, P.-Y., Gas-phase femtosecond transient absorption spectroscopy. *Rev. Sci. Instrum.* **2006,** *77*, 1-4.

23. Schriever, C.; Lochbrunner, S.; Riedle, E.; Nesbitt, D. J., Ultrasensitive ultraviolet-visible 20 fs absorption spectroscopy of low vapor pressure molecules in the gas phase. *Rev. Sci. Instrum.* **2008,** *79*, 013107(1-9).

24. Stavros, V. G.; Verlet, J. R. R., Gas-Phase Femtosecond Particle Spectroscopy: A Bottom-Up Approach to Nucleotide Dynamics. *Annu. Rev. Phys. Chem.* **2016,** *67*, 211-232.

25. Freedman, K. A.; Becker, R. S., Comparative Investigation of the Photoisomerization of the Protonated and Unprotonated n-Butylamine Schiff Bases of 9-cis-, 11 -cis-, 13-cis-, and all-trans-Retináis. *J. Am. Chem. Soc.* **1986,** *108*, 1245-1251.

26. Logunov, S. L.; Song, L.; El-Sayed, M. A., Excited-State Dynamics of a Protonated Retinal Schiff Base in Solution. *J. Phys. Chem.* **1996,** *100*, 18586-18591.

27. Kraack, J. P.; Buckup, T.; Motzkus, M., Evidence for the two-state-two-mode model in retinal protonated schiff-bases from pump degenerate four-wave-mixing experiments. *Phys. Chem. Chem. Phys.* **2012,** *14*, 13979–13988.

28. Nuss, M. C.; Zinth, W.; Kaiser, W.; Kölling, E.; Oesterhelt, D., Femtosecond spectroscopy of the first events of the photochemical cycle in bacteriorhodopsin. *Chem. Phys. Lett.* **1985,** *117*, 1-7.

29. Wang, Q.; Schoenlein, R. W.; Peteanu, L. A.; Mathies, R. A.; Shank, C. V., Vibrationally coherent photochemistry in the femtosecond primary event of vision. *Science* **1994,** *266*, 422-424.

30. Polli, D.; Altoe, P.; Weingart, O.; Spillane, K. M.; Manzoni, C.; Brida, D.; Tomasello, G.; Orlandi, G.; Kukura, P.; Mathies, R. A.; Garavelli, M.; Cerullo, G., Conical intersection dynamics of the primary photoisomerization event in vision. *Nature* **2010,** *467*, 440-443.

31. Nogly, P.; Weinert, T.; James, D.; Carbajo, S.; Ozerov, D.; Furrer, A.; Gashi, D.; Borin, V.; Skopintsev, P.; Jaeger, K.; Nass, K.; Bath, P.; Bossman, R.; Koglin, J.; Seaberg, M.; Lane, T.; Kekilli, D.; Brünle, S.; Tanaka, T.; Wu, W.; Milne, C.; White, T.; Barty, A.; Weirstall, U.; Panneels, V.; Nango, E.; Iwata, S.; Hunter, M.; Schapiro, I.; Schertler, G.; Neutze, R.; Sandfuss, J., Retinal isomerization in bacteriorhodopsin captured by a femtosecond x-ray laser. *Science* **2018**.

32. Wilhelm, T.; Piel, J.; Riedle, E., Sub-20-fs pulses tunable across the visible from a blue-pumped single-pass noncollinear parametric converter. *Opt. Lett.* **1997,** *22*, 1494-1496.

33. Cerullo, G.; Nisoli, M.; Stagira, S.; Silvestri, S. D., Sub-8-fs pulses from an ultrabroadband optical parametric amplifier in the visible. *Opt. Lett.* **1998,** *23*, 1283-1285.

34. Piel, J.; Beutter, M.; Riedle, E., 20–50 fs pulses tunable across the near infrared from a blue-pumped noncollinear parametric amplifier. *Opt. Lett.* **2000,** *25*, 180-182.

35. Riedle, E.; Beutter, M.; Lochbrunner, S.; J. Piel, S. S.; Spörlein, S.; Zinth, W., Generation of 10 to 50 fs pulses tunable through all of the visible and the NIR. *Appl. Phys. B* **2000,** *71*, 457–465.

36. Cerullo, G.; Silvestri, S. D., Ultrafast optical parametric amplifiers. *Rev. Sci. Instrum.* **2003,** *74*, 1-17.

37. Manzoni, C.; Polli, D.; Cerullo, G., Two-color pump-probe system broadly tunable over the visible and the near infrared

with sub-30 fs temporal resolution. *Rev. Sci. Instrum.* **2006,** *77*, 023103(1-8).

38. Chan, W. L.; Berkelbech, T. C.; Provose, M. R.; Monahan, N. R.; Tritsch, J. R.; Hybersteyn, M. S.; Reichman, D. R.; Gao, J.; Zhu, X. Y., The Quantum Coherent Mechanism for Singlet Fission: Experiment and Theory. *Acc. Chem. Res.* **2012,** *46*, 1321-1329.

39. Rao, A.; Friend, R. H., Harnessing singlet exciton fission to break the Shockley–Queisser limit. *Nat. Rev. Mat.* **2017,** *2*, 17063.

40. Buback, J.; Kullmann, M.; Langhojer, F.; Nuernberger, P.; Schmidt, R.; Würthner, F.; Brixner, T., Ultrafast Bidirectional Photoswitching of a Spiropyran. *J. Am. Chem. Soc.* **2010,** *132*, 16510–16519.

41. Kaszub, W.; Marino, A.; Lorenc, M.; Collet, E.; Bagryanskaya, E. G.; Tretyakov, E. V.; Ovcharenko, V. I.; Fedin, M. V., Ultrafast Photoswitching in a Copper-Nitroxide-Based Molecular Magnet. *Angew. Chem. Int. Ed.* **2014,** *53*, 10636-10640.

42. Briand, J.; Bräm, O.; Re´hault, J.; Le´onard, J. r. m.; Cannizzo, A.; Chergui, M.; Zanirato, V.; Olivucci, M.; Helbing, J.; Haacke, S., Coherent ultrafast torsional motion and isomerization of a biomimetic dipolar photoswitch. *Phys. Chem. Chem. Phys.* **2010,** *12*, 3178-3187.

43. Gueye, M.; Manathunga, M.; Agathangelou, D.; Orozco, Y.; Paolino, M.; Fusi, S.; Haacke, S.; Olivucci, M.; Léonard, J., Engineering the vibrational coherence of vision into a synthetic molecular device. *Nat. Comm.* **2018,** *9*, 1-8.

44. Gai, F.; Hasson, K. C.; McDonald, J. C.; Anfinrud, P. A., Chemical Dynamics in Proteins: The Photoisomerization of Retinal in Bacteriorhodopsin. *Science* **1998,** *279*, 1886-1891.

45. Wand, A.; Rozin, R.; Eliash, T.; Jung, K.-H.; Sheves, M.; Ruhman, S., Asymmetric toggling of a natural photoswitch: Ultrafast spectroscopy of Anabaena Sensory Rhodopsin. *J. Am. Chem. Soc.* **2011,** *133*, 20922-20932.

46. Mathies, R., A coherent picture of vision. *Nat. Chem.* **2015,** *7*, 945-947.

47. Congreve, D. N.; Lee, J.; Thompson, N. J.; Hontz, E.; Yost, S. R.; Reusswig, P. D.; Bahlke, M. E.; Reineke, S.; Voorhis, T. V.; Baldo, M. A., External Quantum Efficiency Above 100% in a Singlet-Exciton-Fission–Based Organic Photovoltaic Cell. *Science* **2013,** *340*, 334-337.

48. Leonard, J.; Schapiro, I.; Briand, J.; Fusi, S.; Paccani, R. R.; Olivucci, M.; Haacke, S., Mechanistic Origin of the Vibrational Coherence Accompanying the Photoreaction of Biomimetic Molecular Switches. *Chem. Euro. J.* **2012,** *18*, 15296-15304.

49. Okada, T.; Sugihara, M.; Bondar, A.-N.; Elstner, M.; Entel, P.; Buss, V., The Retinal Conformation and its Environment in Rhodopsin in Light of a New 2.2 A° Crystal Structure. *J. Mol. Biol.* **2004,** *342*, 571-583.

50. Vogeley, L.; Sineshchekov, O. A.; Trivedi, V. D.; Sasaki, J.; Spudich, J. L.; Luecke, H., Anabaena sensory rhodopsin: a photochromic color sensor at 2.0 Å. *Science* **2004,** *306*, 1390-1393.

51. Nishikawa, T.; Murakami, M.; Kouyama, T., Crystal Structure of the 13-cis Isomer of Bacteriorhodopsin in the Dark-adapted State. *J. Mol. Biol.* **2005,** *352*, 319-328.

52. Spudich, J. L.; Yang, C.-S.; Jung, K.-H.; Spudich, E. N., RETINYLIDENE PROTEINS: Structures and Functions from Archaea to Humans. *Annu. Rev. Cell Dev. Biol.* **2000,** *16*, 365-392.

53. Kawanabe, A.; Kandori, H., Photoreactions and structural changes of anabaena sensory rhodopsin. *Sensors* **2009,** *9*, 9741-9804.

54. Ernst, O. P.; Lodowski, D. T.; Elstner, M.; Hegemann, P.; Brown, L. S.; Kandori, H., Microbial and Animal Rhodopsins: Structures, Functions, and Molecular Mechanisms. *Chem. Rev.* **2014,** *114*, 126-163.

55. Lanyi, J. K., Understanding structure and function in the light-driven proton pump bacteriorhodopsin. *J. Struct. Biol.* **1998,** *124*, 164-178.

56. Sasaki, J.; Spudlich, J. L., Proton transport by sensory rhodopsins and its modulation by transducer-binding. *Biochim. Biophys. Acta.* **2000,** *1460*, 230-239.

57. Kamo, N.; Shimono, K.; Iwamoto, M.; Sudo, Y., Photochemistry and photoinduced proton-transfer by pharaonis phoborhodopsin. *Biochemistry* **2001,** *66*, 1277-1282.

58. Essen, L. O., Halorhodopsin: light-driven ion pumping made simple? *Curr. Opsin. Struct. Biol.* **2002,** *12*, 516-522.

59. Negel, G.; Ollig, D.; Fuhrmann, M.; Kateriya, S.; Musti, A. M.; Bamberg, E.; Hegemann, P., Channelrhodopsin-1: a light-gated proton channel in green algae. *Science* **2002,** *296*, 2395-2398.

60. Wand, A.; Gdor, I.; Zhu, J.; Sheves, M.; Ruhman, S., Shedding new light on retinal photochemistry. *Annu. Rev. Phys. Chem.* **2013,** *64*, 437-458.

61. Kobayashi, T.; Saito, T.; Ohtani, H., Real-time spectroscopy of transition states in bacteriorhodopsin during retinal isomerization. *Nature* **2001,** *414*, 531-534.

62. Kukura, P.; McCamant, D. W.; Yoon, S.; Wandschneider, D. B.; Mathies, R. A., Structural observation of the primary Isomerization in vision with Femtosecond-Stimulated Raman. *Science* **2005,** *310*, 1006-1009.

63. McCamant, D. W.; Kukura, P.; Mathies, R. A., Femtosecond stimulated Raman Study of excited-state evolution in Bacteriorhodopsin. *J. Phys. Chem. B* **2005,** *109*, 10449-10457.

64. Zgrablic, G.; Voitchovsky, K.; Kindermann, M.; Haacke, S.; Chergui, M., Ultrafast excited state dynamics of the protonated schiff base of all-trans retinal in solvents. *Biophys. J.* **2005,** *88*, 2779–2788.

65. Kahan, A.; Nahmias, O.; Friedman, N.; Sheves, M.; Ruhman, S., Following photoinduced dynamics in bacteriorhodopsin with 7-fs Impulsive Vibrational Spectroscopy. *J. Am. Chem. Soc.* **2007,** *129*, 537-546.

66. Polli, D.; Rivalta, I.; Nenov, A.; O.Weingart; Garavelli, M.; Cerullo, G., Tracking the primary photoconversion events in rhodopsins by ultrafast optical spectroscopy. *Photochem. Photobiol. Sci.* **2015,** *14*, 213-228.

67. Schnedermann, C.; Liebel, M.; Kukura, P., Mode-Specificity of vibrationally coherent internal conversion in Rhodopsin during the primary visual event. *J. Am. Chem. Soc.* **2015,** *137*, 2886−2891.

68. Schoenlein, R. W.; Peteanu, L. A.; Mathies, R. A.; Shank, C. V., The first step in vision: femtosecond isomerization of Rhodopsin. *Science* **1991,** *254*, 412-415.

69. Smitienko, O. A.; Mozgovaya, M. N.; Shelaev, I. V.; Gostev, F. E.; Feldman, T. B.; Nadtochenko, V. A.; Sarkisov, O. M.; Ostrovsky, M. A., Femtosecond formation dynamics of primary photoproducts of visual pigment rhodopsin. *Biochemistry* **2009,** *75*, 34-45.

70. Johnson, P. J. M.; Halpin, A.; Morizumi, T.; Prokhorenko, V. I.; P.Ernst, O.; Miller, R. J. D., Local vibrational coherences drive the primary photochemistry of vision. *Nat. Chem.* **2015,** *7*, 980-986.

71. Kim, J. E.; Tauber, M. J.; Mathies, R. A., Wavelength Dependent Cis-Trans Isomerization in Vision. *Biochemistry* **2001,** *40*, 13774-13778.

72. Mathies, R. A.; Cruz, C. H. B.; Polard, W. T.; Shank, C. V., Direct Observation of the femtosecond excited-state cis-trans isomerization in Bacteriorhodopsin. *Science* **1988,** *240*, 777-779.

73. Kandori, H.; Yoshihara, K.; Tomioka, H.; Sasabe, H., Primary Photochemical Events in Halorhodopsin Studied by Subpicosecond Time-Resolved Spectroscopy. *J. Phys. Chem.* **1992,** *96*, 6066-6072.

74. Kandori, H.; Tomioka, H.; Sasabe, H., Excited-State Dynamics of pharaonis Phoborhodopsin Probed by Femtosecond Fluorescence Spectroscopy. *J. Phys. Chem. A* **2002,** *106*, 2091-2095.

75. Kandori, H.; Katsuta, Y.; Ito, M.; Sasabe, H., Femtosecond Fluorescence Study of the Rhodopsin Chromophore in Solution. *J. Am. Chem. Soc.* **1995,** *116*, 2669-2670.

76. Hamm, P.; Zurek, M.; Sschinger, T. R.; Patzelt, H.; Oesterhelt, D.; Zinth, W., Femtosecond spectroscopy of the photoisomerisation of the protonated Schiff base of all-trans retinal. *Chem. Phys. Lett.* **1996,** *263*, 613-621.

77. Schapiro, I.; Ryazantsev, M. N.; Frutos, L. M.; Ferre, N.; Olivucci, M., The ultrafast photoisomerizations of Rhodopsin and Bathorhodopsin are modulated by bond length alternation and HOOP driven electronic effects. *J. Am. Chem. Soc.* **2011,** *133*, 3354-3364.

78. Sharkov, A. V.; Pakulev, A. V.; Chekalin, S. V.; Matveetz, a. Y. A., Primary events in bacteriorhodopsin probed by subpicosecond spectroscopy. *Biochim. Biophys. Acta.* **1985,** *808*, 94-102.

79. Ruhman, S., Bixue Hou, Noga Friedman, Michael Ottolenghi, Mordechai Sheves, Following evolution of Bacteriorhodopsin in its reactive excited state via stimulated emission pumping. *J. Am. Chem. Soc.* **2002,** *124*, 8854-8858.

80. Brown, M. F.; Heyn, M. P.; Job, C.; Kim, S.; Moltke, S.; Nakanishi, K.; Nevzorov, A. A.; Struts, A. V.; Salgado, G. F. J.; Wallat, I., Solid-State 2H NMR spectroscopy of retinal proteins in aligned membranes. *Biochim. Biophys. Acta.* **2007,** *1768*, 2979–3000.

81. Kochendoerfer, G. G.; Verdegem, P. J. E.; Hoef, I. v. d.; Lugtenburg, J.; Mathies, R. A., Retinal Analog Study of the Role of Steric Interactions in the Excited State Isomerization Dynamics of Rhodopsin. *Biochemistry* **1996,** *35*, 16230-16240.

82. Cembran, A.; González-Luque, R.; Serrano-Andrés, L.; ManuelaMerchán; Garavelli, M., About the intrinsic photochemical properties of the 11-cis retinal chromophore: computational clues for a trap state and a lever effect in Rhodopsin catalysis. *Theor. Chem. Acc.* **2007,** *118*, 173-183.

83. Moltke, S.; Nevzorov, A. A.; Sakai, N.; Wallat, I.; Job, C.; Nakanishi, K.; Heyn, M. P.; Brown, M. F., Chromophore Orientation in Bacteriorhodopsin Determined from the Angular Dependence of Deuterium Nuclear Magnetic Resonance Spectra of Oriented Purple Membranes. *Biochemistry* **1998,** *37*, 11821-11835.

84. Eyring, G.; Curry, B.; Broek, A.; Lugtenburg, J.; Mathies, R., Assignment and Interpretation of Hydrogen Out-of-Plane Vibrations in the Resonance Raman Spectra of Rhodopsin and Bathorhodopsin. *Biochemistry* **1982,** *21*, 384-393.

85. Song, L.; El-Sayed, M. A.; Lanyi, J. K., Protein catalysis of the retinal subpicosecond photoisomerization in the primary process of bacteriorhodopsin photosynthesis. *Science* **1993,** *261*, 891-894.

86. Logunov, S. L.; El-Sayed, M. A., Redetermination of the Quantum Yield of Photoisomerization and Energy Content in the K-Intermediate of Bacteriorhodopsin Photocycle and Its Mutants by the Photoacoustic Technique. *J. Phys. Chem. B* **1997,** *101*, 6629-6633.

87. Agathangelou, D.; Orozco-Gonzalez, Y.; Marín, M. d. C.; Roy, P. P.; Brazard, J.; Kandori, H.; Jung, K.-H.; Léonard, J.; Buckup, T.; Ferré, N.; Olivucci, M.; Haacke, S., Effect of point mutations on the ultrafast photo-isomerization of Anabaena sensory rhodopsin. *Faraday Discuss.* **2018,** *207*, 55-75.

88. Jung, K. H.; Trivedi, V. D.; Spudich, J. L., Demonstration of a sensory rhodopsin in eubacteria. *Mol. Microbiol.* **2003,** *47*, 1513-1522.

89. Kawanabe, A.; Furutani, Y.; Jung, K.-H.; Kandori, H., Photochromism of Anabaena Sensory Rhodopsin. *J. Am. Chem. Soc.* **2007,** *129*, 8644-8649.

90. Cheminal, A.; Léonard, J.; young, K. S.; Kwang-Hwan, J.; Hideki, K.; Stefan, H., 100 fs photo-isomerization with vibrational coherences but low quantum yield in Anabaena Sensory Rhodopsin. *Phys. Chem. Chem. Phys.* **2015,** *17*, 25429-25439.

91. Strambi, A.; Durbeej, B.; Ferre, N.; Olivucci, M., Anabaena sensory rhodopsin is a light-driven unidirectional rotor. *Proc. Natl. Acad. Sci. U. S. A.* **2010,** *107*, 21322-21326.

92. Wada, Y.; Kawanabe, A.; Furutani, Y.; Kandori, H.; Ohtani, H., Quantum yields for the light adaptations in Anabaena sensory rhodopsin and bacteriorhodopsin. *Chem. Phys. Lett.* **2008,** *453*, 105-108.

93. Domcke, W.; Yarkony, D. R.; Köppel, H., *Conical Intersections: Electronic Structure, Dynamics and Spectroscopy*. 2004.

94. Schoenlein, R. W.; Peteanu, L. A.; Wang, Q.; Mathies, R. A.; Shank, C. V., Femtosecond dynamics of cis-trans isomerization in a visual pigment analog isorbodopsin. *J. Phys. Chem.* **1993,** *97*, 12087-12092.

95. Cheng, L.-Y.; Zhang, Y.; Liu, S.-G.; Hu, K.-S.; Ruan, K.-C., Studies on the Temperature Effect on Bacteriorhodopsin of Purple and Blue Membrane by Fluorescence and Absorption Spectroscopy. *Acta Biochim. Biophys. Sin* **2006,** *38*, 691-696.

96. Bismuth, O.; Komm, P.; Friedman, N.; Eliash, T.; Sheves, M.; Ruhman, S., Deciphering Excited State Evolution in Halorhodopsin with Stimulated Emission Pumping. *J. Phys. Chem. B* **2010,** *114*, 3046–3051.

97. Zgrablic´, G.; Haacke, S.; Chergui, M., Heterogeneity and Relaxation Dynamics of the Photoexcited Retinal Schiff Base Cation in Solution. *J. Phys. Chem. B* **2009,** *113*, 4384-4393.

98. Wand, A.; Loevsky, B.; Friedman, N.; Sheves, M.; Ruhman, S., Probing ultrafast photochemistry of retinal proteins in the near-IR: Bacteriorhodopsin and Anabaena sensory rhodopsin vs retinal protonated schiff base in solution. *J. Phys. Chem. B* **2013,** *117*, 4670-4679.

99. Hasson, K. C.; Gai, F.; Anfinrud, P. A., The photoisomerization of retinal in bacteriorhodopsin: Experimental evidence for a three-state model. *Proc. Natl. Acad. Sci. U. S. A.* **1996,** *93*, 15124-15129.

100. Logunov, S. L.; Volkov, V. V.; Braun, M.; El-Sayed, M. A., The relaxation dynamics of the excited electronic states of retinal in bacteriorhodopsin by two-pump-probe femtosecond studies. *Proc. Natl. Acad. Sci. U. S. A.* **2001,** *98*, 8475-8479.

101. Warshel, A.; Chu, Z. T., Nature of the Surface Crossing Process in Bacteriorhodopsin: Computer Simulations of the Quantum Dynamics of the Primary Photochemical Event. *J. Phys. Chem. B* **2001,** *105*, 9857-9871.

102. Hayashi, S.; Tajkhorshid, E.; Schulten, K., Molecular Dynamics Simulation of Bacteriorhodopsin's Photoisomerization Using Ab Initio Forces for the Excited Chromophore. *Biophys. J.* **2003,** *85*, 1440-1449.

103. Gonza´lez-Luque, R.; Garavelli, M.; Bernardi, F.; Mercha´n, M.; Robb, M. A.; Olivucci, M., Computational evidence in favor of a two-state, two-mode model of the retinal chromophore photoisomerization. *Proc. Natl. Acad. Sci. U. S. A.* **2000,** *97*, 9379-9384.

104. Cembran, A.; Bernardi, F.; Olivucci, M.; Garavelli, M., Excited-state singlet manifold and oscillatory features of a nonatetraeniminium retinal chromophore model. *J. Am. Chem. Soc.* **2003,** *125*, 12509-12519.

105. Kraack, J. P.; Buckup, T.; Hampp, N.; Motzkus, M., Ground- and excited-state vibrational coherence dynamics in bacteriorhodopsin probed with degenerate four-wave-mixing experiments. *Chem. Phys. Chem.* **2011,** *12*, 1851-1859.

106. Kraack, J. P.; Buckup, T.; Motzkus, M., Vibrational analysis of excited and ground electronic states of all-trans retinal protonated Schiff-base. *Phys. Chem. Chem. Phys.* **2011,** *13*, 21402-21410.

107. Warshel, A., Bicycle pedal model for the first step in the vision process. *Nature* **1976,** *260*, 679-683.

108. Warshel, A.; Weiss, R. M., An Empirical Valence Bond Approach for Comparing Reactions in Solutions and in Enzymes. *J. Am. Chem. Soc.* **1980,** *102*, 6218-6226.

109. Braun, M.; Sobotta, C.; Durr, R.; Pulvermacher, H.; Malkmus, S., Analysis of Wave Packet Motion in Frequency and Time Domain: Oxazine 1. *J. Phys. Chem. A* **2006,** *110*, 9793-9800.

110. Herek, J. L.; Wohlleben, W.; Cogdell, R. J.; Zeidler, D.; Motzkus, M., Quantum control of energy flow in light harvesting. *Nature* **2002,** *417*, 533-535.

111. Kraack, J. P.; Wand, A.; Buckup, T.; Motzkus, M.; Ruhman, S., Mapping multidimensional excited state dynamics using pump-impulsive-vibrational-spectroscopy and pump-degenerate-four-wave-mixing. *Phys. Chem. Chem. Phys.* **2013,** *15*, 14487--14501.

112. Miki, T.; Buckup, T.; Krause, M. S.; Southall, J.; Cogdell, R. J.; Motzkus, M., Vibronic coupling in the excited-states of carotenoids. *Phys. Chem. Chem. Phys.* **2016,** *18*, 11443-11453.

113. Cavalleri, A.; Dekorsy, T.; Chong, H. H. W.; Kieffer, J. C.; Schoenlein, R. W., Evidence for a structurally-driven insulator-to-metal transition in VO2: A view from the ultrafast timescale. *Phys. Rev. B* **2004,** *70*, 161102 (1-4).

114. Mukamel, S., *Principles of Nonlinear Optics and Spectroscopy*. Oxford university press: 1995.

115. Boyd, R., *Nonlinear Optics*. Academic Publication: 1992.

116. Tokmakoff, A., *Time dependent quantum mechanics and spectroscopy*. 2014.

117. Hamm, P.; Zanni, M., *Concepts and Methods of 2D Infrared Spectroscopy*. Chambridge university press: 2011.

118. Kraack, J. P.; Motzkus, M.; Buckup, T., Selective nonlinear response preparation using femtosecond spectrally resolved four-wave-mixing. *J. Chem. Phys.* **2011,** *135*, 224505.

119. Demtröder, W., *Spectroscopy with lasers*. Springer: 1973.

120. Feldstein, M. J.; Vöhringer, P.; Scherer, N. F., Rapid-scan pump–probe spectroscopy withhigh time and wave-number resolution:optical-Kerr-effect measurements of neat liquids. *J. Opt. Soc. Am. B* **1995,** *12*, 1500-1510.

121. Lorenc, M.; Ziolek, M.; Naskrecki, R.; Karolczak, J.; Kubicki, J.; Maciejewski, A., Artifacts in femtosecond transient absorption spectroscopy. *Appl. Phys. B* **2002,** *74*, 19-27.

122. Dadap, J. I.; Focht, G. B.; Reitze, D. H.; Downer, M. C., Two-Photon Absorption in Diamond and Its Application to Ultraviolet Femtosecond Pulse-Width Measurement. *Opt. Lett.* **1991,** *16*, 499-501.

123. Reuther, A.; Laubereau, A.; Nikogosyan, D. N., A simple method for the in situ analysis of femtosecond UV pulses in the pump-probe spectroscopy of solutions. *Opt. Commun.* **1997,** *141*, 180-184.

124. Alfano, R. R.; Baldeck, P. L.; Ho, P. P.; Agrawal, G. P., Cross-Phase Modulation and Induced Focusing Due to Optical Nonlinearities in Optical Fibers and Bulk Materials. *J. Opt. Soc. Am. B* **1989,** *6*, 824-829.

125. Dobler, J.; Zinth, W.; Kaizer, W.; Oesterhelt, D., Excited state reaction dynamics of bacteriorhodopsin study by femtosecond spectroscopy. *Chem. Phys. Lett.* **1988,** *144*, 215-220.

126. Arlt, T.; Schmidt, S.; Zinth, W.; Haupts, U.; Oesterhelt, D., The initial reaction dynamics of the light-driven chloride pump halorhodopsin. *Chem. Phys. Lett.* **1995,** *241*, 549-555.

127. Nakamura, T.; Takeuchi, S.; Shibata, M.; Demura, M.; Kandori, H.; Tahara, T., Ultrafast Pump-Probe Study of the Primary Photoreaction Process in pharaonis Halorhodopsin: Halide Ion Dependence and Isomerization Dynamics. *J. Phys. Chem. B* **2008,** *112*, 12795–12800.

128. Lutz, I.; Sieg, A.; Wegener, A. A.; Engelhard, M.; Boche, I.; Otsuka, M.; Oesterhelt, D.; Wachtveitl, J.; Zinth, W., Primary reactions of sensory rhodopsins. *Proc. Natl. Acad. Sci. U. S. A.* **2001,** *98*, 962-967.

129. Amsden, J. J.; Kralj, J. M.; Chieffo, L. R.; Wang, X.; Erramilli, S.; Spudich, E. N.; Spudich, J. L.; Ziegler, L. D.; Rothschild, K. J., Subpicosecond Protein Backbone Changes Detected during the Green-Absorbing Proteorhodopsin Primary Photoreaction. *J. Phys. Chem. B* **2007,** *111*, 11824-11831.

130. Wand, A.; Friedman, N.; Sheves, M.; Ruhman, S., Ultrafast Photochemistry of Light-Adapted and Dark-Adapted Bacteriorhodopsin: Effects of the Initial Retinal Configuration. *J. Phys. Chem. B* **2012,** *116*, 10444−10452.

131. Doig, S. J.; Reid, P. J.; Matties, R. A., Picosecond Time-Resolved Resonance Raman Spectroscopy of Bacterlorhodopsin's J, K, and KL Intermediates. *J. Phys. Chem.* **1991,** *95*, 6372-6379.

132. Kobayashi, T.; Kim, M.; Taiji, M.; Iwasa, T.; Nakagawa, M.; Tsuda, M., Femtosecond Spectroscopy of Halorhodopsin and Rhodopsin in a Broad Spectral Range of 400-1000 nm. *J. Phys. Chem. B* **1998,** *102*, 272-280.

133. Verhoefen, M.-K.; Bamann, C.; Blöcher, R.; Förster, U.; Bamberg, E.; Wachtveitl, J., The Photocycle of Channelrhodopsin-2: Ultrafast ReactionDynamics and Subsequent Reaction Steps. *Chem. Phys. Chem.* **2010,** *11*, 3113-3122.

134. Zhong, Q.; Ruhman, S.; Ottolenghi, M., Reexamining the Primary Light-Induced Events in Bacteriorhodopsin Using a Synthetic C13=C14-Locked Chromophore. *J. Am. Chem. Soc.* **1996,** *118*, 12828-12829.

135. Atkinson, G. H.; Brack, T. L.; Blanchard, D.; Rumbles, G., Picosecond time resolved Raman spectroscopy of the initial Trans to Cis isomerization in the Bacteriorhodopsin photocycle. *Chem. Phys.* **1989,** *131*, 1-15.

136. Berg, R. v. d.; Du-Jeon-Jang; Bitting, H. C.; El-Sayed, M. A., Subpicosecond resonance Raman spectra of the early intermediates in the photocycle of bacteriorhodopsin. *Biophys. J.* **1990,** *58*, 135-141.

137. al, R. D.; Maiti, S.; Walker, G. C.; Cowea, B. R.; Pippenger, R.; Bogomolni, R. A.; Hochstrasser, R. M., Femtosecond time-resolved infrared laser study of the J-K transition of bacteriorhodopsin. *Chem. Phys. Lett.* **1995,** *241*, 109-115.

138. Hou, B.; Friedman, N.; Ottolenghi, M.; Sheves, M.; Ruhman, S., Comparing photoinduced vibrational coherences in bacteriorhodopsin and in native and locked retinal protonated Schiff bases. *Chem. Phys. Lett.* **2003,** *381*, 549-555.

139. Olivucci, M.; Lami, A.; Santoro, F., A Tiny Excited-State Barrier Can Induce a Multiexponential Decay of the Retinal Chromophore: A Quantum Dynamics Investigation. *Angew. Chem. Int. Ed.* **2005,** *44*, 5118-5121.

140. Polli, D.; Weingart, O.; Brida, D.; Poli, E.; Maiuri, M.; Spillane, K. M.; Bottoni, A.; Kukura, P.; Mathies, R. A.; Cerullo, G.; Garavelli, M., Wavepacket Splitting and Two-Pathway Deactivation in the Photoexcited Visual Pigment Isorhodopsin. *Angew. Chem. Int. Ed.* **2014,** *53*, 2504-2507.

141. Palings, I.; Pardoen, J. A.; Berg, E. v. d.; Winkel, C.; Lugtenburg, J.; Mathies, R. A., Assignment of Fingerprint Vibrations in the Resonance Raman Spectra of Rhodopsin, Isorhodopsin, and Bathorhodopsin: Implications for Chromophore Structure and Environment*. *Biochemistry* **1987,** *26*, 2544-2556.

142. Palings, I.; Berg, E. M. v. d.; Lugtenburg, J.; Mathies, R. A., Complete assignment of the Hydrogen Out-of-Plane wagging vibrations of Bathorhodopsin: chromophore structure and energy storage in the primary photoproduct of vision. *Biochemistry* **1989,** *28*, 1498-1507.

143. Lin, S. W.; Groesbeek, M.; Hoef, I. v. d.; Verdegem, P.; Lugtenburg, J.; Mathies, R. A., Vibrational assignment of torsional normal modes of Rhodopsin: Probing excited-state isomerization dynamics along the reactive C11=C12 torsion coordinate. *J. Phys. Chem. B* **1998,** *102*, 2787-2806.

144. Sugihara, M.; Hufen, J.; Buss, V., Origin and Consequences of Steric Strain in the Rhodopsin Binding Pocket. *Biochemistry* **2006,** *45*, 801-810.

145. Kawanabe, A.; Furutani, Y.; Jung, K.-H.; Kandori, H., FTIR study of the photoisomerization processes in the 13-cis and All-trans forms of Anabaena Sensory Rhodopsin at 77 K. *Biochemistry* **2006,** *45*, 4362-4370.

146. Smith, S.; Pardoen, J. A.; Lugtenburg, J.; Mathies, R. A., Vibrational Analysis of the 13-cis-Retinal Chromophore in Dark-Adapted Bacteriorhodopsin. *J. Phys. Chem.* **1987,** *91*, 804-819.

147. Kim, J. E.; Mathies, R. A., Anti-Stokes Raman Study of Vibrational Cooling Dynamics in the Primary Photochemistry of Rhodopsin. *J. Phys. Chem. A* **2002,** *106*, 8508-8515.

148. Furutani, Y.; Kawanabe, A.; Jung, K.-H.; Kandori, H., FTIR Spectroscopy of the All-Trans Form of Anabaena Sensory Rhodopsin at 77 K: Hydrogen Bond of a Water between the Schiff Base and Asp75. *Biochemistry* **2005,** *44*, 12287-12296.

149. Schnedermann, C.; Muders, V.; Ehrenberg, D.; Schlesinger, R.; Kukura, P.; Heberle, J., Vibronic dynamics of the ultrafast all-trans to 13-cis photoisomerization of retinal in Channelrhodopsin‑1. *J. Am. Chem. Soc.* **2016,** *138*, 4757−4762.

150. Shim, S.; Dasgupta, J.; Mathies, R. A., Femtosecond Time-Resolved Stimulated Raman Reveals the Birth of Bacteriorhodopsin's J and K Intermediates. *J. Am. Chem. Soc.* **2009,** *131* (22), 7592-7597.

151. Groot, H. J. M. d.; Harbison, G. S.; Herzfeld, J.; Griffin, R. G., Nuclear Magnetic Resonance Study of the Schiff Base in Bacteriorhodopsin: Counterion Effects on the 15N Shift Anisotropy. *Biochemistry* **1989,** *28*, 3346-3353.

152. Smith, S. o.; Groot, H. J. M. d.; Gebhard, R.; Courtin, I. M. L.; Lugtenburg, J.; Herzfeld, J.; Griffin, R. G., Structure and Protein Environment of the Retinal Chromophore in Light- and Dark-Adapted Bacteriorhodopsin Studied by Solid-State NMR. *Biochemistry* **1989,** *28*, 8897-8904.

153. Swails, J. M.; York, D. M.; Roitberg, A. E., Constant pH Replica Exchange Molecular Dynamics in Explicit Solvent Using Discrete Protonation States: Implementation, Testing, and Validation. *J. Chem. Theor Comput.* **2014,** *10* (3), 1341-1352.

154. Karplus, M., Charm-GUI: Effeective simulaton input generator and more. 2006.

155. Maier, J. A.; Martinez, C.; Kasavajhala, K.; Wickstrom, L.; Hauser, K. E.; Simmerling, C., ff14SB: Improving the Accuracy of Protein Side Chain and Backbone Parameters from ff99SB. *J. Chem. Theor Comput.* **2015,** *11* (8), 3696-3713.

156. Jorgensen, W. L.; Chandrasekhar, J.; Madura, J. D.; Impey, R. W.; Klein, M. L., Comparison of simple potential functions for simulating liquid water. *J. Chem. Phys.* **1983,** *79*, 926-935.

157. Dickson, C. J.; Madej, B. D.; Skjevik, Å. A.; Betz, R. M.; Teigen, K.; Gould, I. R.; Walker, R. C., Lipid14: The Amber Lipid Force Field. *J. Chem. Theor Comput.* **2014,** *10* (2), 865-879.

158. Hayashi, S.; Tajkhorshid, E.; Schulten, K., Structural Changes during the Formation of Early Intermediates in the Bacteriorhodopsin Photocycle. *Biophys. J.* **2002,** *83*, 1281-1297.

159. Yabushita, A.; Kobayashi, T., Primary Conformation Change in Bacteriorhodopsin on Photoexcitation. *Biophys. J.* **2009,** *96*, 1447–1461.

160. Schaffer, H. E.; Chance, R. R.; R. J. Silbey, K. K.; Schrock, R. R., Conjugation length dependence of Raman scattering in a series of linear polyenes: Implications for polyacetylene. *J. Chem. Phys.* **1991,** *94*, 4161-4170.

161. Kupka, T.; Buczek, A.; Broda, M. A.; Stachów, M.; Tarnowski, P., DFTstudies on the structural and vibrational properties of polyenes. *J. Mol. Model.* **2016,** *22*, 101-111.

162. Tomasello, G.; Olaso-Gonzalez, G.; Altoe, P.; Stenta, M.; Serrano-Andres, L.; Mercha, M.; Orlandi, G.; Bottoni, A.; Garavelli, M., Electrostatic Control of the Photoisomerization Efficiency and Optical Properties in Visual Pigments: On the Role of Counterion Quenching. *J. Am. Chem. Soc.* **2009,** *131*, 5172–5186.

163. Sovdat, T.; Bassolino, G.; Liebel, M.; Schnedermann, C.; Fletcher, S. P.; Kukura, P., Backbone modification of retinal induces protein-like excited state dynamics in solution. *J. Am. Chem. Soc.* **2012,** *134*, 8318−8320.

164. Logunov, S. L.; El-Sayed, M. A.; Lanyi, J. K., Catalysis of the retinal subpicosecond photoisomerization process in acid purple bacteriorhodopsin and some bacteriorhodopsin mutants by chloride ions. *Biophys. J.* **1996,** *71*, 1545-1553.

165. Logunov, S. L.; El-Sayed, M. A.; Song, L., Photoisomerization Quantum Yield and Apparent Energy Content of the K Intermediate in the Photocycles of Bacteriorhodopsin, Its Mutants D85N, R82Q, and D212N, and Deionized Blue Bacteriorhodopsin. *J. Phys. Chem.* **1996,** *100*, 2391-2398.

166. El-Sayed, M. A.; Logunov, S., On the molecular origin of the protein catalysis of the primary process in bacteriorhodopsin photosynthesis: Retinal photoisomerization. *Pure & Appl. Chem.* **1997,** *69*, 749-754.

167. Aharoni, A.; Khatchatouriants, A.; Manevitch, A.; Lewis, A.; Sheves, M., Protein-β-Ionone Ring Interactions Enhance the Light-Induced Dipole of the Chromophore in Bacteriorhodopsin. *J. Phys. Chem. B* **2003,** *107*, 6221-6225.

168. Kennis, J. T. M.; Larsen, D. S.; Ohta, K.; Facciotti, M. T.; Glaeser, R. M.; Fleming, G. R., Ultrafast Protein Dynamics of Bacteriorhodopsin Probed by Photon Echo and Transient Absorption Spectroscopy. *J. Phys. Chem. B* **2002,** *106*, 6067-6080.

169. Xu, D.; Martin, C.; Schulten, K., Molecular Dynamics Study of Early Picosecond Events in the Bacteriorhodopsin Photocycle: Dielectric Response, Vibrational Cooling and the J, K Intermediates. *Biophys. J.* **1996,** *70*, 453-460.

170. Schobert, B.; Cupp-Vickery, J.; Hornak, V.; Smith, S. O.; Lanyi, J. K., Crystallographic Structure of the K Intermediate of Bacteriorhodopsin: Conservation of Free Energy after Photoisomerization of the Retinal. *J. Mol. Biol.* **2002,** *321*, 715-726.

171. Zgrablic, G.; Haacke, S.; Chergui, M., Vibrational coherences of the protonated Schiff base of all-trans retinal in solution. *Chem. Phys.* **2007,** *338*, 168-174.

172. Melaccio, F.; Ferre´, N.; Olivucci, M., Quantum chemical modeling of rhodopsin mutants displaying switchable colors. *Phys. Chem. Chem. Phys.* **2012,** *14*, 12485–12495.

173. Mataga, N.; Chosrowjan, H.; Taniguchi, S., Investigations into the dynamics and mechanisms of ultrafast photoinduced reactions taking place in photoresponsive protein nanospaces (PNS). *J. Photochem. Photobiol. C* **2004,** *4*, 155-168.

174. Sineshchekov, O. A.; Spudich, E. N.; Trivedi, V. D.; Spudich, J. L., Role of the cytoplasmic domain in Anabaena Sensory Rhodopsin photocycling: Vectoriality of schiff base deprotonation. *Biophys. J.* **2006,** *91*, 4519-4527.

175. Elisa, F.-M.; Brustmann, B.; Oesterhett, D., A C-terminal truncation results in high-level expression of the functional photoreceptor sensory rhodopsin I in the archaeon Halobacterium salinarium. *Mol. Microbiol.* **1993,** *9*, 943-953.

176. Ovchinnikov, Y. A.; Abdulaev, N. G.; Kiselev, A. V.; Drachev, L. A.; Kaulen, A. D.; Skulachev, V. P., The water-exposed C-terminal sequence of bacteriorhodopsin does not affect H^+ pumping. *FEBS Lett.* **1986,** *194*, 16-20.

177. Yang, C.-S.; Spudich, J. L., Light-induced structural changes occur in the transmembrane helices of the Natronobacterium pharaonis HtrII transducer. *Biochemistry* **2001,** *40*, 14207-14214.

178. Shi, L.; Yoon, S. R.; Bezerra, A. G.; Jung, K.-H.; Brown, L. S., Cytoplasmic shuttling of protons in Anabaena Sensory Rhodopsin: implications for signaling mechanism. *J. Mol. Biol.* **2006,** *358*, 686-700.

179. Kawanabe, A.; Furutani, Y.; Jung, K.-H.; Kandori, H., Engineering an Inward Proton Transport from a Bacterial Sensor Rhodopsin. *J. Am. Chem. Soc.* **2009,** *131*, 16439–16444.

180. Birge, R. R.; Cooper, T. M.; Lawrence, A. F.; Masthay, M. B.; Zhang, C.-F.; Zidovetzki, R., Revised Assignment of Energy Storage in the Primary Photochemical Event in Bacteriorhodopsin. *J. Am. Chem. Soc.* **1991,** *113*, 4327-4328.

181. Váró, G.; Lanyi, J. K., Effects of the Crystalline Structure of Purple Membrane on the Kinetics and Energetics of the Bacteriorhodopsin Photocycle. *Biochemistry* **1991,** *30*, 7165-7171.

182. Dong, B.; Sannchez-Magraner, L.; Luecke, H., Structure of an Inward Proton-Transporting Anabaena Sensory Rhodopsin Mutant: Mechanistic Insights. *Biophys. J.* **2016,** *111*, 963-972.

183. Huntress, M. M.; Gozem, S.; Malley, K. R.; Jailaubekov, A. E.; Vasileiou, C.; Vengris, M.; Geiger, J. H.; Borhan, B.; Schapiro, I.; Larsen, D. S.; Olivucci, M., Toward an Understanding of the Retinal Chromophore in Rhodopsin Mimics. *J. Phys. Chem. B* **2013,** *117*, 10053−10070.

184. Loevsky, B.; Wand, A.; Bismuth, O.; Friedman, N.; Sheves, M.; Ruhman, S., A New Spectral Window on Retinal Protein Photochemistry. *J. Am. Chem. Soc.* **2011,** *133*, 1626-1629.

185. Herbst, J.; Heyne, K.; Diller, R., Femtosecond Infrared Spectroscopy of Bacteriorhodopsin Chromophoren Isomerization. *Science* **2002,** *297*, 822-825.

186. Nango, E.; Royant, A.; Kubo, M.; Nakane, T.; CeciliaWickstrand; Kimura, T.; Tanaka, T.; Tono, K.; Song, C.; Tanaka, R.; Arima, T.; Yamashita, A.; Kobayashi, J.; Hosaka, T.; EiichiMizohata; Nogly, P.; Sugahara, M.; Nam, D.; Nomura, T.; Shimamura, T.; Im, D.; Fujiwara, T.; Yamanaka, Y.; Jeon, B.; Nishizawa, T.; Oda, K.; Fukuda, M.; Andersson, R.; Båth, P.; Dods, R.; Davidsson, J.; ShigeruMatsuoka; Kawatake, S.; MichioMurata; Nureki, O.; Owada, S.; Kameshima, T.; Hatsui, T.; Joti, Y.; Schertler, G.; Yabashi, M.; Bondar, A.-N.; Standfuss, J.; Neutze, R.; Iwata, S., A three-dimensionalmovie of structural changes in bacteriorhodopsin. *Science* **2016,** *354*, 1552-1557.

187. Berg, M.; Bout, D. A. V., Ultrafast Raman Echo Measurements of Vibrational Dephasing and the Nature of Solvent-Solute Interactions. *Acc. Chem. Res.* **1997,** *30*, 65-71.

188. Tokmakoff, A.; Fleming, G. R., Two-dimensional Raman spectroscopy of the intermolecular modes of liquid CS2. *J. Chem. Phys.* **1997,** *106*, 2569-2582.

189. Guo, Z.; Molesky, B. P.; Cheshire, T. P.; Moran, A. M., Elucidation of reactive wavepackets by two-dimensional resonance Raman spectroscopy. *J. Chem. Phys.* **2015,** *143*, 124202 (1-15).

Acknowledgement

First of all, I would like to thank Deutsche Forschungsgemeinschaft (DFG) and Agence Nationale de la Recherche (ANR) for the financial support during the course of my doctoral study.

I would like to express my deepest gratitude to my supervisor Dr. Tiago Buckup for giving me the opportunity to pursue my PhD research career on such a cutting edge topic in the field of ultrafast spectroscopy. His immense patience and guidance have channelized all research plans and ideas into a fruitful pathway. I thank him for giving me enough freedom to implement my ideas, which has helped me to grow up as a scientist. In addition, I thank him for teaching me how to present the research findings in the most interesting way for the audiences in a seminar or for the readers of any scientific article.

I would like to thank Prof. Andreas Dreuw and Prof. Hans-Robert Volppp who kindly agreed to be the referees for my doctoral oral exam. I also thank both of them for investing their time to review my thesis. I thank Prof. Volppp also for the laser safety instruction before entering the lab and especially for his interesting questions and comments during the group seminars.

I am thankful to Prof. Markus Motzkus for giving me the opportunity to work in his lab with an extremely nice laser system, which has helped to acquire high quality of experimental data. I would also like to thank him for providing his inspiring ideas during our discussions.

Here, I would like to acknowledge my cooperative partners who were involved in the same research project on Anabaena Sensory Rhodopsin. I am grateful to Dr. Yoshitaka Kato, Dr. Rei Yoshizumi and Prof. Hideki Kandori from Nagoya Institute of Technology in Japan for their tireless effort to extract and purify the protein samples. I would like to thank Damianos Agathangelou, Dr. Jeremie Léonard and Prof. Stephan Haacke from University of Strassbourg in France for the experimental collaborations as well as for the critical appreciations and brainstorming discussions in our meetings. I thank Dr. Elisa Pieri and Prof. Nicola Ferré from Aix-Marseille University in France and Prof. Masimo Olivucci and co-workers from Bowling Green State University in USA to carry out the theoretical studies, which gave an invaluable insights to understand our experimental results.

I appreciate the support of Mr. Klaus Schmitt and his team from the mechanics workshop for making a metallic flow cell holder. I am also thankful to Mr. Gerhard Schodt and Mr. Uwe Branczyk for helping me to build an illuminating setup with LED, which was essential for the light adaptation of the protein sample.

I thank secretaries Ms. Sylvia Boganski and Ms. Angelika Neuner for their supports to prepare the official documents for research stay in Germany. A special thanks to Ms. Boganski for her help to find accommodation in Heidelberg and to complete the administrative procedures in the university at the beginning of my PhD career.

My cordial thanks to all my current and former colleagues who made the journey of my PhD career very smooth. I am fortunate enough to have officemates like Dr. Jiang Man (JJ), Nicoló Alagna and Nikolaus Wollscheid, who always bring the fresh air of happiness. I thank Nicoló for his help in the lab and especially for keeping the window of fun always open in our office. I am thankful to JJ for being so supportive, kind and caring friend. I would also like to thank Klaus for helping me for the correction of my manuscript and also for ‘decoding’ the German official letters.

I am thankful to Dr. Takeshi Miki, Zhibin Zhang and Andreas Ludwig, who spent time with me in the lab. Takeshi explained me every details of the experimental setups and also taught me about the adjustment of the NOPA. Zhibin helped me for optical adjustments during the experimental measurements. I learnt a lot about the lab from Andreas.

I would like to thank Dr. José Luis Pérez Lustres, Dr. Nick Paul and Dr. Yang Li for expressing their views on my research works, which guided me to innovate new research ideas. It was great fun to attend the conference of Ultrafast Phenomena with Luis and the conference of Photochemistry with Nick.

I am also thankful to Christian Busch for the support to perform the steady state Raman measurements, Florian Nicolai for helping me to translate my abstract into German and Niklas Müller for correcting a part of my thesis. Further, I would like express my gratitude to my former colleagues Dr. Elisabeth Brühl, Dr. Lukas Brückner, Dr. Mariana Ishikawa, Dr. Julia Herz, Daniel Garz, Esther Kimmle and Cinthia Emanuello. I feel myself to be extremely lucky as a member of

such a dynamic research group. Spending these three years of my PhD career with great fun of the scientific discoveries was truly a unique experience and will be stored in my memory forever.

Finally, my deepest appreciation goes to my parent, brother, relatives and friends for their encouragement, patience and undemanding supports.

Eidesstattliche Versicherung gemäß § 8 der Promotionsordnung der Naturwissenschaftlich-Mathematischen Gesamtfakultät der Universität Heidelberg

1. Bei der eingereichten Dissertation zu dem Thema

Femtosecond Vibrational Dynamics of Anabaena Sensory Rhodopsin

handelt es sich um meine eigenständig erbrachte Leistung.

2. Ich habe nur die angegebenen Quellen und Hilfsmittel benutzt und mich keiner unzulässigen Hilfe Dritter bedient. Insbesondere habe ich wörtlich oder sinngemäß aus anderen Werken übernommene Inhalte als solche kenntlich gemacht.

3. Die Arbeit oder Teile davon habe ich wie folgt/bislang nicht1) an einer Hochschule des In- oder Auslands als Bestandteil einer Prüfungs- oder Qualifikationsleistung vorgelegt.

Titel der Arbeit: ______________________________

Hochschule und Jahr: ______________________________

Art der Prüfungs- oder Qualifikationsleistung: ______________________________

4. Die Richtigkeit der vorstehenden Erklärungen bestätige ich.

5. Die Bedeutung der eidesstattlichen Versicherung und die strafrechtlichen Folgen einer unrichtigen oder unvollständigen eidesstattlichen Versicherung sind mir bekannt.

Ich versichere an Eides statt, dass ich nach bestem Wissen die reine Wahrheit erklärt und nichts verschwiegen habe.

Heidelberg, 06/11/18
Ort und Datum

Partha Pratim Roy
Unterschrift

---

1) Nicht Zutreffendes streichen. Bei Bejahung sind anzugeben: der Titel der andernorts vorgelegten Arbeit, die Hochschule, das Jahr der Vorlage und die Art der Prüfungs- oder Qualifikationsleistung.

12/2012